LAWRENCE
LIVERMORE
NATIONAL
LABORATORY

UCRL-TH-224123

High-Contrast Imaging using Adaptive Optics for Extrasolar Planet Detection

J. W. Evans

August 31, 2006

This work was performed under the auspices of the U.S. Department of Energy by University of California, Lawrence Livermore National Laboratory under Contract W-7405-Eng-48.

High-Contrast Imaging using Adaptive Optics for Extrasolar Planet Detection

by

JULIA WILHELMSEN EVANS

B.S. (Stevens Institute of Technology) 2001
M.S. (University of California, Davis) 2003

DISSERTATION
Submitted in partial satisfaction of the requirements for the degree of
DOCTOR OF PHILOSOPHY

in

Engineering - Applied Science

in the

OFFICE OF GRADUATE STUDIES
of the
UNIVERSITY OF CALIFORNIA
DAVIS

Approved:

_____

_____

_____

Committee in Charge

2006

High-Contrast Imaging using Adaptive Optics for Extrasolar Planet Detection

by

Julia Wilhelmsen Evans

Julia Wilhelmsen Evans

September 2006

Engineering - Applied Science

High-Contrast Imaging using Adaptive Optics for Extrasolar Planet Detection

Abstract

Direct imaging of extrasolar planets is an important, but challenging, next step in planetary science. Most planets identified to date have been detected indirectly — not by emitted or reflected light but through the effect of the planet on the parent star. For example, radial velocity techniques measure the doppler shift in the spectrum of the star produced by the presence of a planet. Indirect techniques only probe about 15% of the orbital parameter space of our solar system. Direct methods would probe new parameter space, and the detected light can be analyzed spectroscopically, providing new information about detected planets. High contrast adaptive optics systems, also known as Extreme Adaptive Optics (ExAO), will require contrasts of between 10^{-6} and 10^{-7} at angles of $4 - 24\ \lambda/D$ on an 8-m class telescope to image young Jupiter-like planets still warm with the heat of formation. Contrast is defined as the intensity ratio of the dark wings of the image, where a planet might be, to the bright core of the star. Such instruments will be technically challenging, requiring high order adaptive optics with > 2000 actuators and improved diffraction suppression. Contrast is ultimately limited by residual static wavefront errors, so an extrasolar planet imager will require wavefront control with an accuracy of better than 1 nm rms within the low- to mid-spatial frequency range.

Laboratory demonstrations are critical to instrument development. The ExAO

testbed at the Laboratory for Adaptive Optics was designed with low wavefront error and precision optical metrology, which is used to explore contrast limits and develop the technology needed for an extrasolar planet imager. A state-of-the-art, 1024-actuator micro-electrical-mechanical-systems (MEMS) deformable mirror was installed and characterized to provide active wavefront control and test this novel technology. I present 6.5×10^{-8} contrast measurements with a prolate shaped pupil and flat mirror demonstrating that the testbed can operate in the necessary contrast regime. Wavefront measurements and simulations indicate that contrast is limited by wavefront error, not diffraction. I demonstrate feasibility of the MEMS deformable mirror for meeting the stringent residual wavefront error requirements of an extrasolar planet imager with closed-loop results of 0.54 nm rms within controllable spatial frequencies. Individual contributors to final wavefront quality have been identified and characterized. I also present contrast measurements of 2×10^{-7} made with the MEMS device and identify amplitude errors as the limiting error source. Closed-loop performance and simulated far-field measurements using a Kolmogorov phase plate to introduce atmosphere-like optical errors are also presented.

To Gary Sommargren,

For personal and intellectual inspiration.

Contents

List of Figures

List of Tables

Acknowledgements

This work has been supported by the Gordon and Betty Moore Foundation through its grant to the UCO/Lick Observatory Laboratory for Adaptive Optics and the NSF Science and Technology Center for Adaptive Optics, managed by the University of California at Santa Cruz under cooperative agreement No. AST-9876783. This work was performed under the auspices of the U.S. Department of Energy by the University of California, Lawrence Livermore National Laboratory under contract No. W-7405-Eng-48.

Many people have contributed to my success as a graduate student. I would like to thank my advisers Scot Oliver, and Hector Baldis for their guidance and my colleagues at LLNL who have answered numerous questions and helped me to become a better scientist including Bruce Macintosh, Lisa Poyneer, Dave Palmer, Brian Bauman, Don Phillion, Butch Bradsher and Nhan Nguyen. My experiments at the LAO would not have been as successful (or as much fun) without the help of Daren Dillon, Scott Severson, Don Gavel, and Katie Morzinski.

Finally I would like to thank my family for their love and support. Without their spare bedrooms my travels through northern California on the quest for my degree would have been much more difficult. Special thanks to Sandra Evans for proof reading my thesis and my mother and my grandmother for all of those dinners I didn't have to cook. And to my husband Dave, thank you for being there through the good times when I passed, the bad times when I had to try again, and everything in between.

Chapter 1

High-Contrast Imaging using Adaptive Optics for Extrasolar Planet Detection

1.1 Introduction

Looking up into the starry night sky it is hard not to wonder if out there among the countless stars there is another world like our own—or maybe many, many worlds. Beyond the sentimental questions of our place in the universe, other planets could help us learn about the formation of planets, including our own. We could look for signs of life and maybe learn about our own origins. The idea of an image of a planet like our own around another sun is scientifically and emotionally captivating. It is also technically challenging. The discovery of over 150 extrasolar planets [1] has opened a new era in planetary science, one in which our theories of planetary formation must be based on more than just our solar system. Detected planets have already lead to major revisions

in planetary formation theories, and the desire to test new theories fuels the search for more planets and more complete statistics [2]. To date, most planets have been detected indirectly— not by emitted or reflected light but through the effect of the planet on the parent star. For the most part, these planets do not look like Earth or even Jupiter. It is clear, however, that the tools are rapidly developing and that the search is on.

The progression of planetary science relies on technical advances in astronomical instrumentation. Indirect techniques have made great progress. This progress is discussed in the next section. Although indirect techniques are complimentary to direct detection, the information about a planet detected indirectly is limited. With direct detection, light from the planet could be used spectroscopically to determine material make up. For direct detection systems, the figure of merit is contrast. Contrast is defined as the intensity ratio of the dark wings of the image, where a planet might be, to the bright core of the star. How much contrast do we need? In our solar system the Earth is over a billion times dimmer than the sun requiring contrasts of about 10^{-10} in visible light [3]. In general, contrast is limited by wavefront error and diffraction (see Chapter 2). Wavefront error can be introduced by optical errors in the telescope or instrument and by the atmosphere (in ground-based systems). Adaptive optics systems can correct this wavefront error. Diffraction is a fundamental limit of any imaging system, but can be manipulated. High-contrast imaging with current systems is limited to about 10^{-4} in the mid-IR. These six orders of magnitude represent a long way to go to imaging Earth-like planets, but there will be a lot of interesting planetary science on the way. Next-generation, ground-based, planet-imaging systems (first light in approximately 2010) will look for young Jupiter-like planets that are still glowing with the heat of formation. This will require contrasts of between 10^{-6} and 10^{-7} [4] at IR wavelengths.

Ground-based planet imagers represent a new type of adaptive optics instrumentation. An Extreme Adaptive Optics (ExAO) system is designed specifically for high-contrast applications instead of balancing the needs of many observation types like a more general science instrument. That specialization makes the remaining two orders of magnitude improvement in contrast feasible, although technology development is still required and is the focus of the work presented here. Earth-like planets will most likely be imaged by space-based systems, which can avoid atmospheric effects. It is important to note for all of these techniques that the imaging or detection of a single planet, while exciting, is not scientifically interesting. A survey of extrasolar planets is needed to really gain insight.

1.2 Indirect detection

As of June, 2006 173 planets were detected using indirect techniques [1]. By far the most common technique is radial velocity, but other methods are starting to yield results as well. I have briefly reviewed the indirect detection techniques and their limitations in this section. An interesting discussion on the first 8 planets discovered using indirect techniques and their impact on planetary formation theories can be found in a paper by Marcy and Butler [5].

The most common indirect method is radial velocity or doppler detection [5]. This method relies on small perturbations in the velocity of the parent star caused by the planet and favors large planets at close separations. This technique determines separation from the star and the approximate mass of the planet depending on its unknown inclination. Most exciting about radial velocity is the large number of planets detected, providing valuable statistics about the number of stars that might have planets. One limitation is the time it takes to confirm a planet. In general the planet must make one

full orbit around the parent star to confirm its existence. Planets, like Jupiter and Saturn, with wider orbits (12 and 30 years respectively [6]) will take a long time to observe with this method.

Astrometry is the oldest technique for indirect detection of extrasolar planets but has not yielded any results [2]. It requires looking for small perturbations in the position of a parent star [3]. It is difficult to know if the star has moved when there is no obvious reference. Other astrophysical and instrumental noise sources can limit measurements. One advantage of this method is that the mass determined is not related to orbital inclination as in radial velocity methods. Ground-based astrometry is usually done with an interferometer and could potentially find small (Earth-size) planets. An excellent review of work in this area can be found in Sozzetti [2].

Photometric techniques break into two categories [3]: transit methods and mircolensing. In the first case the light of the star is slightly reduced by the transit of the planet across the star. For this to work the planet must be aligned such that it can be observed from Earth and the timing must be right as the transit will happen rarely, and for only a short period of time. The signals for detection are quite small leading to frequent false positives. Typically this method can detect planets that have already been located with another technique, but may have more success in a space-based observatory [7]. Once the planet is detected, it is possible to extract some spectroscopic information about the planet from the data.

Gravitational lensing that is caused by a small point source, like a star, is known as mircolensing. As another photometric technique, it can be employed on the same instrumentation as transit searches. Microlensing occurs when the light from a source star is deflected by a mass (usually another star) between the source and the observer.

Lensing occurs in a predictable way, and perturbations from models can indicate the presence of a planet [8]. The likelihood of an event is quite small, and millions of stars must be constantly monitored to yield results. Four planets have been detected with this method including the lowest-mass planet found to date [8]. Microlensing is particularly sensitive in the 3-6 AU range for very small Earth-like planets. This technique can probe an interesting parameter space for planets but is not conducive to follow up observations because most of the planets detected will be difficult to image.

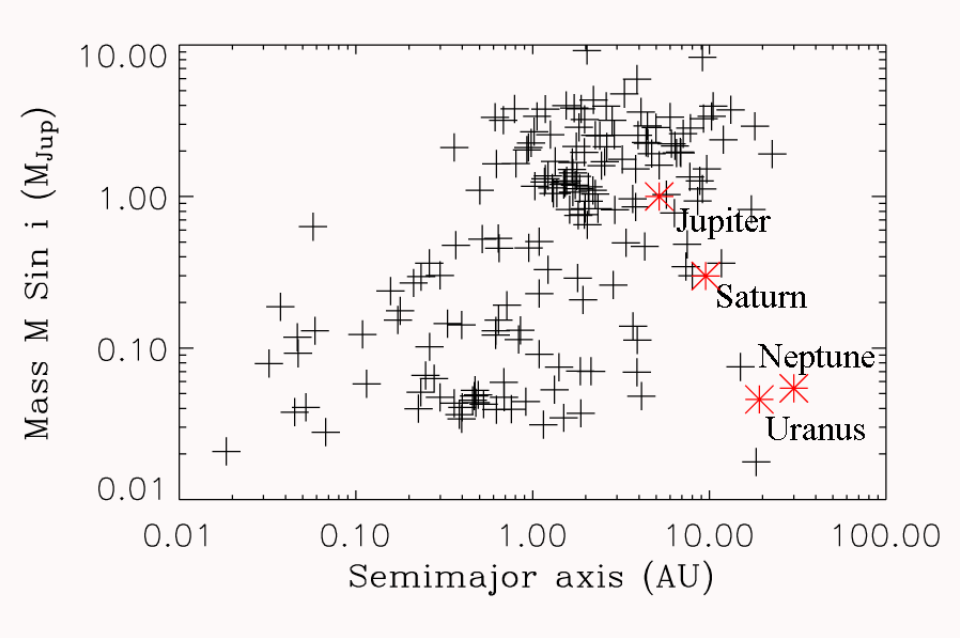

Figure 1.1: A plot of mass versus position of known planets from the California & Carnegie Planet Search website [1]. The plus signs indicate planet detected indirectly and are mostly larger planets with small radii. A few planets from our solar system are shown for comparison [6].

With the planets that have already been detected, statistics about the number and location of extrasolar planets are being compiled, but most of these planets are not like Earth or Jupiter. The parameter space covered by the detected planets corresponds to just 15% of our own solar system. The position and mass of the known planets are shown in Fig. 1.1. The plus signs represent planets detected indirectly [1]. A few

planets from our solar system are also plotted [6] to demonstrate that indirect detection does not probe the parameter space of most of our solar system. It is clear that a combination of many searching techniques will be needed to generate more complete statistics about the number and location of extrasolar planets. Different techniques can also yield different information about planets. Direct detection will be very valuable tool, but indirect methods should not be abandoned. Working in tandem, indirect detections will inform the design and use of future direct detection systems. Information about the planets detected indirectly is limited and for many interesting types of planets these techniques will take too long. Direct detection is the obvious next step in planetary science instrumentation.

1.3 Current high-contrast astronomy

While new high-contrast imaging systems are being built, current high-contrast astronomy is on-going at many observatories. For ground-based observation, adaptive optics systems are critical and generally are coupled with instrumentation to attenuate starlight. At the Keck telescope a coronagraph can be used with the adaptive optics system [9]. Several systems, including one at the Very Large Telescope (VLT), also use differential imagers, which take multiple simultaneous images at different wavelengths and combine them to remove starlight while not attenuating light from the planet [10, 11]. Contrast is limited in current systems to approximately 10^{-4} at separations of about 0.5" [11]. While this level, as mentioned in Section 1.1, is not sufficient for imaging Earth-like planets there are several observational strategies that can make use of it. Astronomers can look for young, massive planets which are much brighter [9] or look at much wider angles where contrast improves [12]. Null results, while not as exciting as

imaging a planet, can still provide valuable information about upper limits to planet mass and location, which informs future planet searches [13, 12]. Planets around much dimmer brown dwarfs also do not require as much contrast. Space telescopes can also be used for high-contrast astronomy. Starlight can be better attenuated through point spread function (PSF) subtraction in these systems because of greater stability over ground-based systems. Current space-based systems were not optimized for planet searches and often suffer from residual scattered light. Space-based telescopes are also limited by aperture size [14]. One major limitation of all current high-contrast work is the inability to conduct a survey of many potential exoplanets. Imaging a single exoplanet, under unusual circumstances, while exciting, is not as scientifically valuable as a larger survey, such as is performed by indirect radial velocity searches.

1.4 Future extrasolar planet imaging

The performance limits of a ground-based exoplanet imager were first discussed by Angel [15], but were optimized for only a handful of very bright stars and required unproven wavefront sensor technology. A more practical approach, which eventually led to a design study for a Keck instrument [16] and later to the Gemini Planet Imager (GPI), was outlined by Macintosh et. al. [17]. This approach focused on improving existing wavefront sensor (WFS) technology coupled with novel deformable mirror technology to conduct a survey of many potential planets. High-contrast systems will have more actuators, faster update rates and less residual wavefront error than conventional systems. The exact requirements for these areas depend on the science criteria of the particular instrument.

GPI is an extrasolar planet imager for the 8-m Gemini South Telescope in

Chile. It will undertake a survey of nearby stars (10-50 parsecs) looking for young, Jupiter-like planets. This system will have contrasts of 10^{-6} to 10^{-8} over a region from 4 to 24 λ/D. At 1 μm this region corresponds to an angular separation of between 0.1" and 0.6". GPI will operate at wavelengths of 1 to 2.5 μm. For comparison a planet with an orbit of 5 AU (the orbit of Jupiter) at 50 parsecs would have an angular separation of 0.1". Nominally GPI will have over 2000 actuators (48 actuator across the diameter) using a novel, deformable, micro-electrical-mechanical-systems (MEMS) mirror. The spatially filtered Shack-Hartmann WFS will run at 2500 Hz. An apodized-pupil Lyot coronagraph will be used for diffraction suppression. A secondary calibration system will enable precision wavefront control, reducing residual wavefront errors to 1 nm rms. The science instrument will be an integral field unit (IFU), similar to the OH-Suppressing Infra-Red Imaging Spectrograph (OSIRIS) [18]. An IFU allows imaging at multiple wavelengths simultaneously, which is useful for identifying planets because speckles produced by wavefront errors will scale differently with wavelength then images of a planet. The spectral information can also be used to characterize planets. GPI is scheduled for first light in 2010.

The Spectro-Polarimetric High-contrast Exoplanet Research (SPHERE) project is building a ground-based giant exoplanet imager for the VLT located in Chile funded by the European Southern Observatory [19]. It has similar goals [20] and technical requirements [21, 22] to GPI and is also scheduled for first light in 2010.

Future, space-based missions for extrasolar planet detection will focus on Earth-like planets in the habitable zone. This is the region around a star where the temperature is right for liquid water [3]. (It depends on the temperature of the star as well as separation distance.) Space missions are planned to spend part of their lifetimes looking for

planets and the other part characterizing what they find. Compared to ground-based missions, space-based missions will have much better contrast and much shorter operating lifetimes. Shorter lifetimes means a smaller list of potential planets. There are three main missions under study with two distinct architectures. The Darwin project [23], under study by the European Space Agency, and the Terrestrial Planet Finder Interferometer (TPF-I) [24], under study by the Jet Propulsion Laboratory (JPL) with funding from NASA, are formation flying interferometers. These spacecraft will be multiple telescope spacecraft flying in formation with a combiner spacecraft that will interfere the collected beams. Based on the principles of nulling interferometry, the beams will be shifted and combined such that the starlight is destructively interfered while the planet light is not. The two projects are collaborating on formation studies to minimize the effect of thermal and scattered light. The Terrestrial Planet Finder Coronagraph (TPF-C) has an architecture more similar to ground-based missions. It uses a telescope with adaptive optics (for correcting optical errors—there are no atmospheric errors in space) and a coronagraph for suppressing diffraction. Unlike a ground-based instrument, it operates in the visible, has an elliptical primary mirror (due to launch constraints) and will achieve contrasts of 10^{-10}. All of these missions are planned for launch after first light on the ground-based instruments mentioned above. More information can be found about TPF at their website [25].

1.5 Summary of graduate work

Designing a next-generation high-contrast planet imager requires many technical advances. Laboratory testbed experiments are critical in understanding fundamental limits and demonstrating feasibility. At the Laboratory for Adaptive Optics, I have

worked on technology development for a giant planet imager. This work contributed to the awarding of a contract with Gemini Observatory to build an instrument. On this type of instrument there are many contributors, even over the more narrow area of technology development. In this section I try to clarify what work on this project is specifically my own.

I identified laboratory contrast limitations through experiments with a flat mirror and shaped pupils on the testbed [26]. Using wavefront data from the phase shifting diffraction interferometer, I simulated performance and compared to experimental results. I compared the performance of prolate shaped pupils manufactured with lithographic etching and machining.

I completed characterization of the micro-electrical-mechanical-systems (MEMS) deformable mirror including unpowered flatness, number and type of irregular actuators and stroke.

I ran closed-loop tests identifying and reducing error sources leading to flattening of < 1 nm rms wavefront error within controllable spatial frequencies, meeting the precision flattening requirements of a giant extrasolar planet imager and demonstrating the best MEMS deformable mirror performance to date.

I also completed contrast measurements with the MEMS, without additional aberrations, again meeting the requirements for a planet imager. This involved characterization of amplitude errors that limited contrast and reducing scattered light in the focal plane.

I have completed preliminary demonstrations of flattening the wavefront with additional Kolmogorov-like wavefront aberrations and simulations of far-field performance with those abberations, demonstrating feasibility of the MEMS deformable mirror

for more realistic tests leading to an instrument prototype.

Chapter 2

Basic Principles

2.1 Introduction

High-contrast imaging, like that needed for imaging extrasolar planets from the ground, is technically challenging. A common comparison is that looking for planets around other stars is like looking for a firefly near a search light from 3000 miles away. The planet is very close to the star, and the planet is much dimmer than the star.

In a perfect system, with no atmospheric distortion, starlight will still be scattered into the region of interest (ROI) by the fundamental process of diffraction. For example, a perfect telescope with a circular aperture (and no central obscuration) will produce an image in the form of an Airy pattern (See Fig. 2.1). At 10 λ/D, the Airy pattern will limit contrast to 10^{-4}, and at more desirable angles of less than this, contrast is even worse. Diffraction is a fundamental limit to contrast. Any real system will also have wavefront error, either introduced by the atmosphere or from the optics of the system itself. These errors will also limit contrast.

When designing an astronomical instrument, it is important to quantify the effect of error sources in order to make an error budget indicating the technical require-

ments for achieving a desired scientific performance. An extrasolar planet imager can be described as an imaging system, and the analytical tools of Fourier optics yield insight into the fundamental limitations of high-contrast imaging.

2.2 Point spread function expansion

The point spread function (PSF) of an imaging system is the output of the system (the image) for a point source input. It is also known as the impulse response. In general for an image with small wavefront error (WFE), most of the light will be concentrated in the core of the image. Off-axis values of the PSF will indicate limits to contrast. The PSF can be calculated from the generalized pupil function: $P(x, y) = a(x, y)\mathrm{e}^{\mathrm{i}\phi(x,y)}$, where $a(x, y)$ represents the real illuminated aperture function (a circle for example) and $\phi(x, y)$ represents a real phase function (a combination of residual atmospheric and systematic optical errors, for example). The electric field, $E(X, Y)$, in the image plane is the Fourier transform of the pupil, where X and Y are the image plane coordinates. The PSF is $|E(X, Y)|^2$. Mathematically explicit expansions of the PSF using the Taylor series can be found in several references [27–29]. Here I briefly summarize the second order expansion of Sivaramakrishnan et. al. [27]. The function $\mathrm{e}^{\mathrm{i}\phi(x,y)}$ can be expanded using a Taylor series:

$$\mathrm{e}^{\mathrm{i}\phi(x,y)} = 1 + \mathrm{i}\phi - \phi^2/2 + \cdots \tag{2.1}$$

Calculating the PSF using the above expansion, truncating second order terms:

$$\begin{aligned} PSF = & AA^* \\ & - \mathrm{i}\left[A\left(A \star \Phi\right)^* - A^*\left(A \star \Phi\right)\right] \\ & + \left(A \star \Phi\right)\left(A \star \Phi\right)^* \\ & - \frac{1}{2}\left[A\left(A \star \Phi \star \Phi\right)^* + A^*\left(A \star \Phi \star \Phi\right)\right] \end{aligned} \tag{2.2}$$

where A,Φ are the Fourier transforms of $a(x, y)$ and $\phi(x, y)$ respectively, $\star$ represents a convolution and $*$ the complex conjugate [27]. Each of the terms in the PSF expansion has physical significance.

The first term AA^* represents the perfect PSF with no WFE. For example, a circular aperture without WFE would return an Airy pattern in the image (See Fig. 2.1). For high-contrast imaging, a PSF with a sharp drop off, as from an apodized aperture, is more desirable. For example, a broad Gaussian aperture would produce a sharp Gaussian image. A Gaussian, however, is not physical because its wings extend to infinity. An aperture apodized with a Blackman function can suppress diffraction (See Fig. 2.1).

At first glance, the second term appears unphysical because it is imaginary. This term, however, can be expressed as:

$$-\mathrm{i}\left[A\left(A \star \Phi\right)^* - A^*\left(A \star \Phi\right)\right] = 2\mathcal{I}\left[A\left(A \star \Phi\right)^*\right] \tag{2.3}$$

where $\mathcal{I}$ indicates the imaginary part of the expression, making it a real antisymmetric perturbation of the perfect PSF [27]. This term produces speckles 'pinned' to the perfect aperture diffraction pattern. When $a(x, y)$ is an apodized function, this term is suppressed with the first term.

The third term in the PSF expansion is arguably the most important for a ground-based planet imager. This term can be expressed as the power spectrum of $A\Phi$

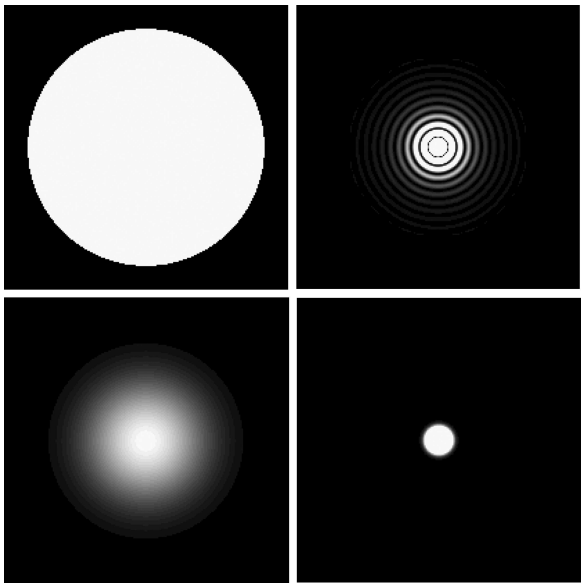

Figure 2.1: Top: A circular aperture and no wavefront error produces an Airy pattern in the image plane. Bottom: An apodized aperture such as a Blackman window has diffraction suppressed in the image plane.

and indicates that WFE will introduce speckles into the PSF regardless of apodization. In regions where diffraction is suppressed, WFE will ultimately limit contrast [27].

The final term is also dependent on the aperture function and will be suppressed by an apodized pupil. At the origin (the center of the image) this term reduces to the Maréchal approximation which relates Strehl ratio, S, to phase variance, σ_ϕ^2 [27]. At high Strehl ratios, $S \simeq 1 - \sigma_\phi^2$. Strehl ratio is the amount of light in the core of an image, and the light in the halo is roughly $1 - S$, or σ_ϕ^2. Assuming $\sigma_\phi^2 = 1$ nm rms and is evenly distributed over a region of interest 48 λ/D wide, contrast will be approximately 10^{-8} at a wavelength of 1.5 μm.

The second and third terms of the PSF expansion can best be understood with an example. Starting with a circular or apodized pupil and introducing a sinusoidal phase error of a single frequency, two images are simulated (See Fig. 2.2). In the top image with the circular aperture an Airy pattern is produced, but the rings are obviously distorted by the effect of the second 'pinned' speckle term. In the bottom image,

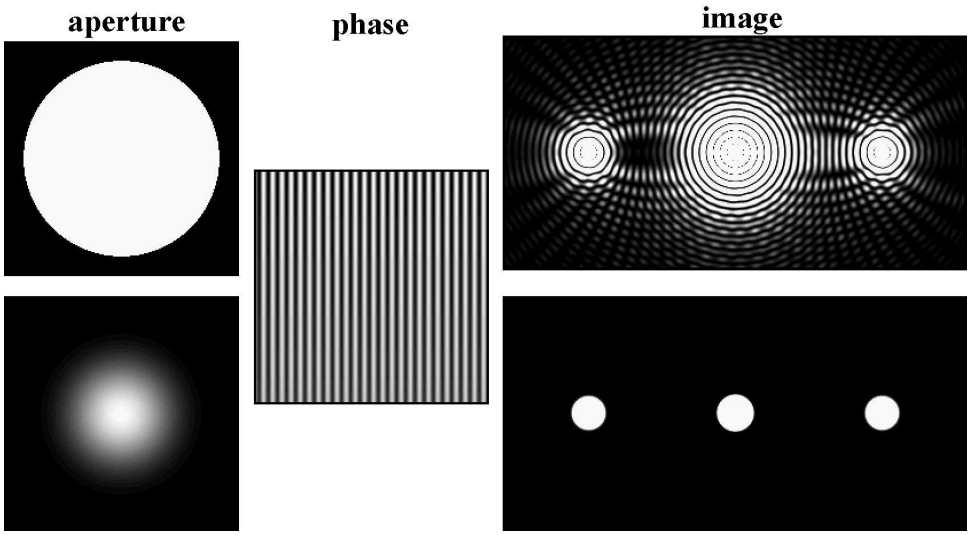

Figure 2.2: Images produced with the circular aperture (top) and the apodized Blackman aperture (bottom) and a sinusoidal phase error. The image without apodization shows diffraction (the Airy pattern) and the pinned speckle term (the wavy distortion of the Airy rings). In the bottom image diffraction is suppressed, but wavefront error still introduces speckles in a position correlated to the spatial frequency of the input phase error.

diffraction is suppressed by a Blackman apodized aperture, but the phase error still introduces speckles in the image plane caused by the third term. These speckles are in a position directly related to the spatial frequency of the sinusoidal phase error. This example illustrates the importance of suppressing diffraction and controlling wavefront error in high-contrast imaging. It also demonstrates the correspondence between spatial frequency in the wavefront and speckle position in the image plane. High-frequency errors will scatter to large angles making mid-frequency errors the most critical for a ROI near the star.

2.3 Suppressing Diffraction

In astronomical instrumentation, diffraction is controlled with a coronagraph. The original coronagraphs were designed to image the corona of the sun. As seen in Fig. 2.1, a coronagraph can be as simple as an apodized pupil, but in practice, a number

of factors must be considered in coronagraph selection. Manufacturability is critical—many coronagraphs are designed before the technology to manufacture them is available. Apodizations are limited both by the ability to replicate the design and the substrate upon which the apodization is produced. Any errors in manufacturing could introduce WFE, which may limit performance. A serious consideration in coronagraph design is diffraction suppression versus throughput. The inner working distance (IWD), or how close to the target star the ROI begins, is also a critical design feature as the IWD has direct consequences on the science limits of an instrument. Certain coronagraphs produce small, non-circularly symmetric ROIs which can limit performance. Telescope geometry must be considered in coronagraph design. The terrestrial planet finder - coronagraph (TPF-C) project, for example, will have an elliptical primary mirror, requiring an elliptical coronagraph. In ground-based systems, the coronagraph must account for the central obscuration and support structure.

2.3.1 Shaped pupils

In a laboratory setting, the requirements for a coronagraph are slightly different. The size of the ROI, the throughput, and the IWD are not serious considerations. A design which is simple to implement and simulate and does not introduce additional WFE into the system is highly desirable. Shaped pupils are nearly ideal for laboratory experiments. These binary masks can be machined or etched from a metal sheet and inserted as the system aperture. Shaped pupils do not require a glass substrate so additional WFE is not introduced, and they are inherently broadband. Edge quality can be a problem and more complicated designs with small feature sizes can be difficult to manufacture. Shaped pupils only suppress diffraction over a particular region, and in the presence of large WFEs that region can be contaminated. Image formation convolves

the aperture with WFE, causing a large speckle to take on the shape of the primary PSF, effectively increasing its size and introducing diffraction into the ROI.

Shaped pupils are not new; Jacquinot and Dossier [30] provide a through description of early efforts with shaped pupils. Experimental tests with these early designs produced limited results, probably as a result of WFE in the testing systems. Advances in computing and manufacturing have allowed new designs and realizations of shaped pupils. Kasdin et. al. [31, 32] have developed many new and sophisticated pupil designs, including some elliptical ones for the elliptical geometry of TPF-C.

Basic, single-opening shaped pupils are based on typical apodization functions. For example, a lineout through the Blackman aperture of Fig. 2.1 would trace the top half of a Blackman shaped pupil. The Blackman function is composed of sines and cosines making it easy to simulate. However, it is not the ideal apodization function. The ideal function is a prolate spheroid function, developed by Slepian and Pollak in 1961 [33]. This function is calculated from an eigenvalue problem and provides the

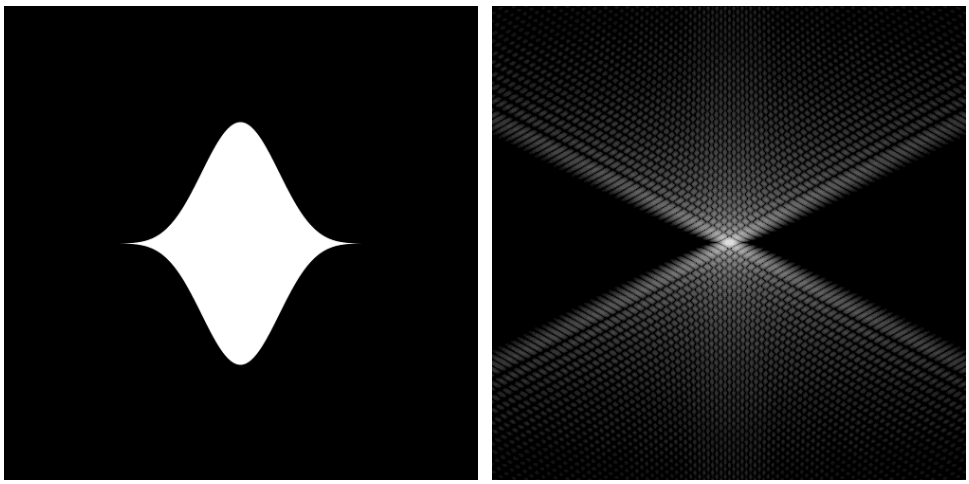

Figure 2.3: The prolate shaped pupil and the resulting far-field image without wavefront error. The x-shaped pattern is characteristic of the prolate shaped pupil.

points for the single opening prolate spheroid shaped pupil used on the ExAO testbed for diffraction suppression (see Fig. 2.3). Pupils were manufactured using both machining

and lithographic etching. I estimate the machined pupil to have an edge quality three times worse than the lithographic pupil (see Fig. 2.4).

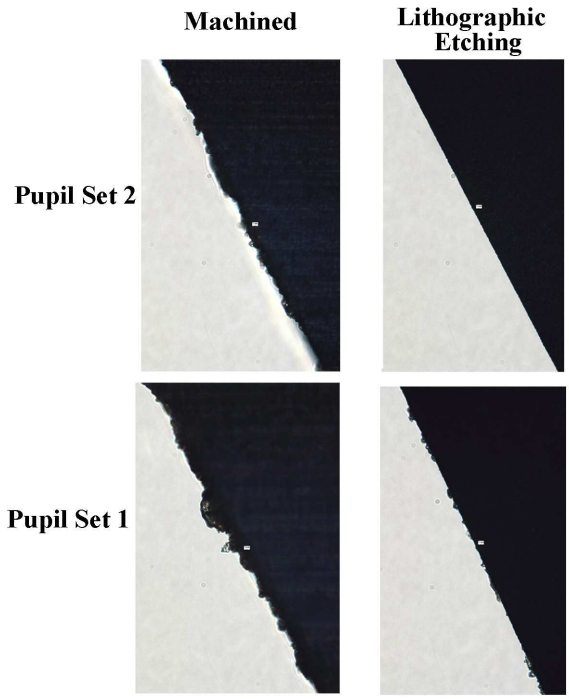

Figure 2.4: Microscope images of four shaped pupils used on the ExAO testbed. The small white box in each represents 1 μm. The pupils made with lithographic etching have better edge quality than the machined pupils. The original pupils were imaged after being in use for several months and may have been damaged during that time, indicating that shaped pupils should be stored with care.

One of the advantages of simple shaped pupils is the ease of simulating performance. A simulated pupil can be generated and applied to a measured or simulated wavefront measurement and Fourier transformed to simulate an image. For a single-opening pupil, a simple, one dimensional Fourier transform can be used to simulate on-axis performance in the absence of WFE [32]. Comparing the analytic model to the two-dimensional simulation ensures that the simulated pupil is generated correctly. For my simulations a 1024 by 1024 array was used, and to avoid pixelation errors, the edge of the simulated mask uses the gray pixel approximation (GPA).

2.3.2 Lyot Coronagraph

Shaped pupils work well in the laboratory, but the small ROI and problems with the central obscuration make them unsuitable for ground-based instrumentation. A more traditional approach, which produces a circularly symmetric ROI, is a Lyot coronagraph. First developed by Lyot in 1939 [34], the coronagraph's original use was to image the corona of the sun, which is roughly a million times dimmer than the core. Lyot recognized that blocking the light from the sun was not sufficient. A second 'Lyot' stop was required to suppress diffraction. He also noted the necessity of high-quality optics to avoid scattered light caused by optical imperfections.

A modern Lyot coronagraph is basically the same as the original design. An occulting spot blocks the on-axis light from the star while a secondary stop at the second pupil plane blocks the halo caused by diffraction, enabling faint structure (or planets) to be imaged. The size of each of the stops has to be optimized for the ROI and the geometry of the imaging system. The use of adaptive optics greatly improves the performance of a coronagraph by concentrating the starlight in a smaller core allowing a smaller occulting spot and thus a smaller IWD.

An excellent description of a modern Lyot coronagraph working with adaptive optics is given by Sivaramakrishnan et. al. [35]. A one dimensional description of coronagraphs details how the instrument works (See Fig. 2.5 from Sivaramakrishnan et. al. [35]). Part a) in the diagram represents the aperture of the system, which is Fourier transformed to produce part b), the image. The image is multiplied by c), the occulting stop, producing d), the masked image. In this case, the occulting stop is Gaussian, but a square function is more common because of manufacturing concerns. Fourier transforming the masked image produces the second pupil image, e). The second pupil is

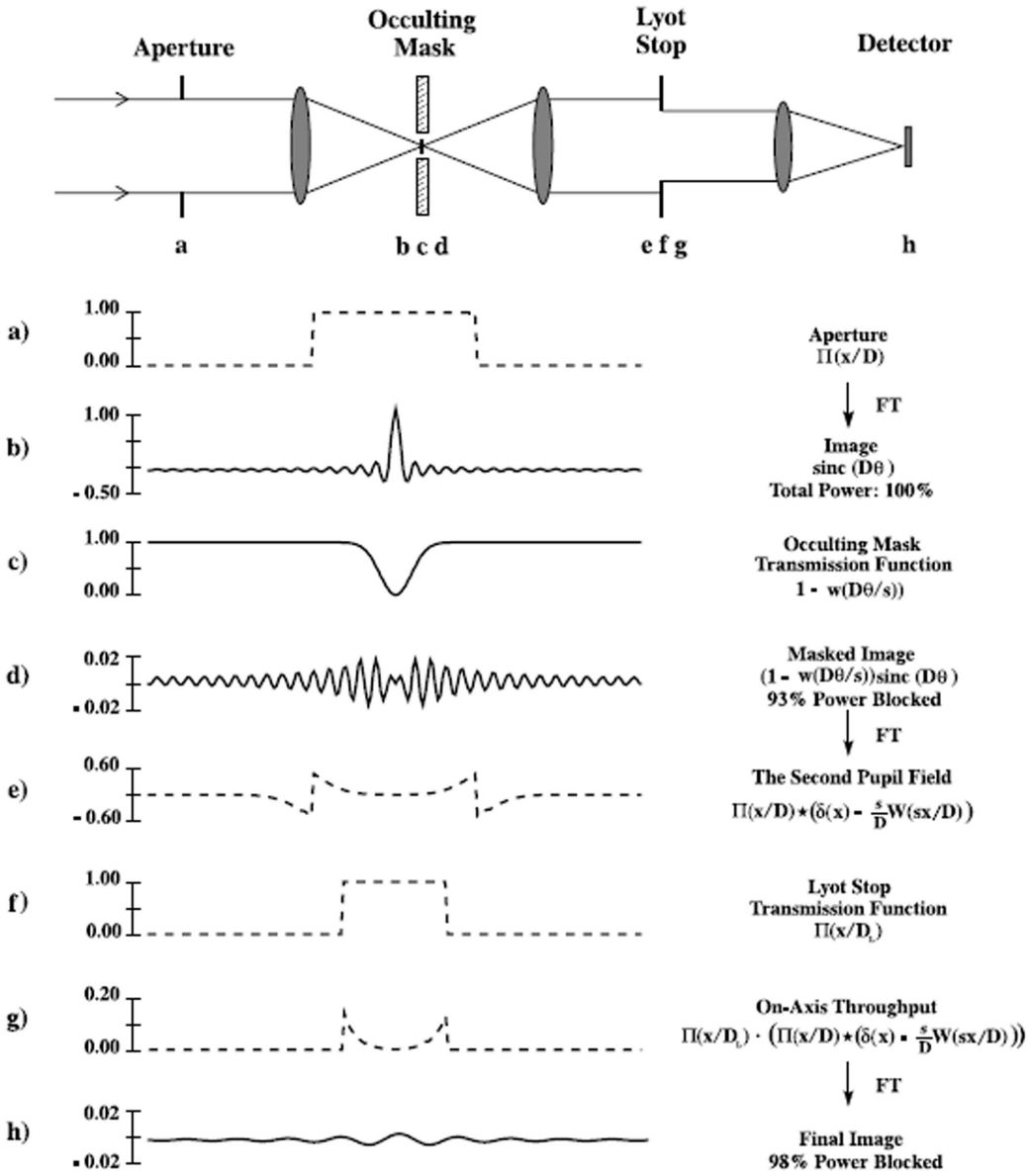

Figure 2.5: One-dimensional coronagraph summary from Sivaramakrishnan et. al. [35], with locations and electric field or stop profiles of (a) primary pupil for on-axis source, (b) image before image plane stop, (c) image plane stop, (d) image after image plane stop, (e) pupil before Lyot stop, (f) Lyot stop, (g) pupil after Lyot stop, and (h) final on-axis image. In this example, 98% of the incident power is blocked by the coronagraph.

multiplied by the Lyot stop, f), producing g). The Fourier transform of the masked pupil is the final image, h), where most of the on-axis signal has been blocked.

Classical Lyot coronagraphs, as described above, will not perform well enough for GPI. Instead, an Apodized Pupil Lyot Coronagraph (APLC) will be used [36]. In this case, the pupil before the focal plane mask is apodized to improve throughput and diffraction suppression by the coronagraph. The level of apodization required for this application is not as difficult to achieve as it is for other types of apodized coronagraphs, thus making it manufacturable with current technology for the desired wavelengths.

Space-based, high-contrast instruments are pursuing band-limited coronagraphs, another type of Lyot coronagraph [37]. In a band-limited coronagraph, the Fourier transform of the occulting spot has limited spatial frequency extent. The easiest example is a square function, which is one over a small region and zero everywhere else. The occulting spot that has this Fourier transform is a Sinc function [38]. A Sinc function along each axis is two-dimensional band-limited mask because two band-limited functions multiplied together produce another band-limited function. These masks work well in visible light [37] and are minimally sensitive to low-order WFE [38]. They are, however, difficult to manufacture for IR wavelengths which limits their usefulness for ground-based applications.

2.4 Adaptive Optics for Wavefront Correction

Adaptive Optics (AO) provides dynamic, real-time correction of optical errors for a wide variety of applications, including astronomical and biomedical imaging, high-power laser systems, and laser communication systems. In all of these applications, a dynamic optical error is introduced and must be compensated to achieve good per-

formance. In ground-based astronomical imaging, most of the WFE is introduced by the atmosphere. Uncorrected images are blurry with low resolution while corrected images have most of the light concentrated in a diffraction limited core. Many excellent references exist on AO [39, 40]. A brief summary is provided here of important characteristics of AO systems as related to extreme adaptive optics (ExAO) systems, which are discussed in the next section.

Figure 2.6 is a typical schematic of an AO system provided by Claire Max [41]. There are three main components to an adaptive optics system. A wavefront sensor

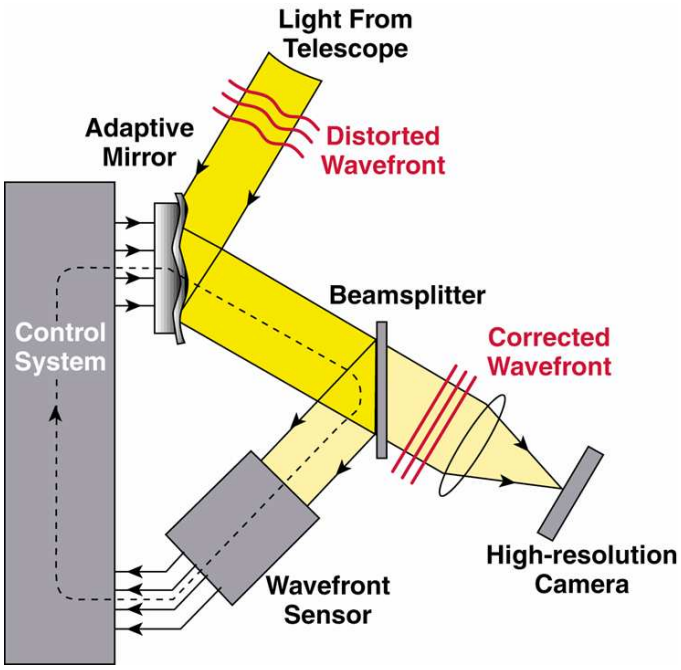

Figure 2.6: Schematic of a basic AO system from the lecture notes of an AO course at UCSC by Claire Max [41]. The distorted wavefront is corrected by the DM and the resulting wavefront is split between the science instrument and the WFS. The WFS provides feedback to the DM.

(WFS) is used to measure the optical aberration, then a wavefront reconstructor or control system is used to send commands to a deformable mirror (DM). The DM produces an opposite wavefront that cancels the aberration of the incoming beam. The most common WFS technology is the Shack-Hartmann WFS. In this system, an array of lenslets

in the pupil plane subdivides the aperture into subapertures. The position of the focal spot of each lenslet is dependent on the local wavefront gradient over each subaperture. A CCD array is used to measure the position of each spot, and that information can be used to reconstruct the wavefront [39]. There are many other types of WFS, including curvature systems [39], pyramid WFS [42] and interferometers of various types [39, 43]. Conventional DMs are made of a glass substrate with piezoelectric (PZT) or piezomagnetic (PMN) actuators attached to the back, which deform the substrate when a voltage is applied. The front surface of the substrate has a reflective coating. These systems have actuator spacings on the order of millimeters and cost about $1000/acutator [41]. More recently, many new types of DMs have become available, including micro-electrical-mechanical-systems (MEMS) (see Section 3.4), membrane deformable mirrors [44], and liquid crystals [45]. These technologies promise more actuators with a smaller actuator spacing for less money per channel and could revolutionize AO. Reconstruction is usually performed with a vector-matrix multiplication, but new techniques using Fourier transforms are critical for next generation systems [46]. The ExAO testbed can use the phase shifting diffraction interferometer or a Shack-Hartmann as the WFS for controlling the MEMS DM.

A common metric for AO system performance is Strehl ratio, defined as the ratio of actual peak intensity in an image to peak intensity without WFE. There are a number of system characteristics which determine AO performance, including number of subapertures, update rate and calibration errors. An AO system with more subapertures (i.e., more DM actuators) will have higher Strehl ratios and require brighter reference stars. Atmospheric errors change rapidly, and quality of wavefront correction is dependent on how well the AO system keeps up with those changes, or the bandwidth of the

system. Internal calibration errors are critical for high-contrast AO systems. These errors are caused by systematic optical errors, particularly non-common path errors between the WFS and the science camera, and will limit AO performance.

2.5 Extreme Adaptive Optics

Extreme Adaptive Optics systems are optimized for high-contrast imaging. These systems incorporate a coronagraph for diffraction suppression with high-actuator-count, high-bandwidth AO systems for exceptional AO performance. ExAO systems will achieve Strehl ratios of $> 90\%$, but Strehl ratio, S, is not the critical metric for high-contrast systems. The Strehl ratio represents how much light is concentrated into the core of the image, which will be blocked by the coronagraph of an ExAO system. The light that is not in the core, roughly $1 - S$, will be in the halo around the star and will ultimately limit contrast [17]. A high Strehl ratio is critical for achieving high contrast but not sufficient. In theory, an AO system can correct WFE out to a spatial frequency directly related to the number of actuators across the aperture, producing a dark hole region in the image where the halo is virtually nonexistant [47, 17]. In conventional AO systems, the dark hole is not visible because intensity in the halo is limited by aliasing. These are errors introduced by the AO system itself in an attempt to correct high-order errors that the WFS incorrectly measures as low-order errors. ExAO systems will use spatially filtered WFSs to avoid aliasing [29]. Another error source in conventional AO imaging that must be reduced for high contrast are internal calibration errors. These errors are problematic for high-contrast imaging because they will introduce speckles to the dark hole region which will not average out over long exposures [27]. As mentioned in Section 2.2, residual wavefront errors for an ExAO system operating in the near-IR

must be less than 1 nm rms to achieve 10^{-8} contrast.

Figure 2.7 is a simulated PSF for an ExAO system designed for the Gemini 8-meter telescope named the Gemini Planet Imager (GPI) [48]. In this image, different

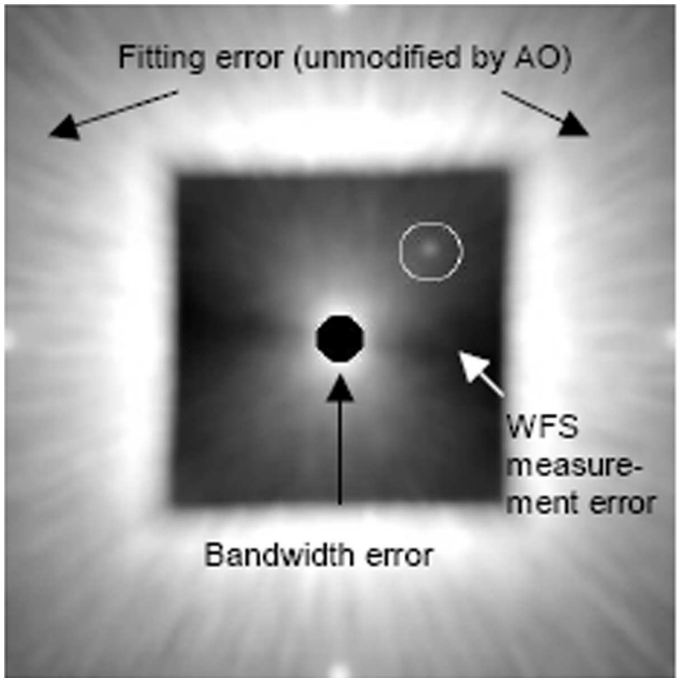

Figure 2.7: A simulated ExAO system PSF from Macintosh et. al. [48]. The dark circle in the center is the starlight blocked by the coronagraph. The dark hole is the region of the PSF that can be corrected by the DM without aliasing. Imperfect atmospheric correction due to bandwidth error produces some scattered light in the dark region and internal calibration and WFS errors will also produce speckles in that region. Outside of the dark hole, errors are dominated by high-order atmospheric errors that cannot be corrected by the ExAO system. A faint planet is visible in the upper right corner.

regions of the PSF are dominated by speckles produced by different types of wavefront errors. The dark circle in the center is where the starlight is blocked by the occulting stop of the coronagraph. Directly around this dark circle is scattered light caused by bandwidth errors. Even though GPI will have an update rate about twice the rate of current systems, bandwidth errors will still be a dominant error source. The square dark hole region produced by the deformable mirror has a width $n/2$ in λ/D units, where n is the number of actuators. Residual wavefront errors (such as calibration errors) will

also introduce speckles to the dark hole region. Outside of the dark hole, the image is dominated by high-order atmospheric errors that cannot be corrected by the ExAO system. In this simulation a faint planet is visible in the right upper corner of the image.

Chapter 3

The Extreme Adaptive Optics Testbed

3.1 Introduction

The Laboratory for Adaptive Optics, located at the University of California, Santa Cruz, is generously funded by the Gordon and Betty Moore foundation for the development and testing of advanced adaptive optics technology for future astronomical instrumentation [49]. Currently there are two main projects: extreme adaptive optics (ExAO) for extrasolar planet imaging, and multi-conjugate adaptive optics for large next generation telescopes. The ExAO testbed has focused on exploring the limitations of the high-contrast regime and the development and testing of micro-electrical-mechanical-systems (MEMS) deformable mirror (DM) technology. Future work (not included here) will include component testing and assembly of the Gemini Planet Imager (GPI).

3.2 Description

The ExAO testbed has two modes of operation: far-field imaging, and wavefront measurement interferometry (phase shifting diffraction interferometer mode). The far-field measurements directly measure the contrast of the system. Wavefront measurements simulate far fields as a consistency check and provide optical metrology of the system. Wavefront measurements are also used for closed-loop control of the MEMS deformable mirror. The testbed was designed with high-quality optics to ensure that end-to-end wavefront error (WFE) would be small (< 1.5 nm RMS). Initial high-contrast measurements focused on measurement techniques and instrumentation without active correction, in particular, suppressing diffraction, understanding the high-contrast regime and developing experimental methods for high-contrast imaging (i.e., controlling scattered light) [26]. After initial tests, a 1024-actuator MEMS deformable mirror, developed by Boston Micromachines Corporation (BMC) [50], was installed for active wavefront control.

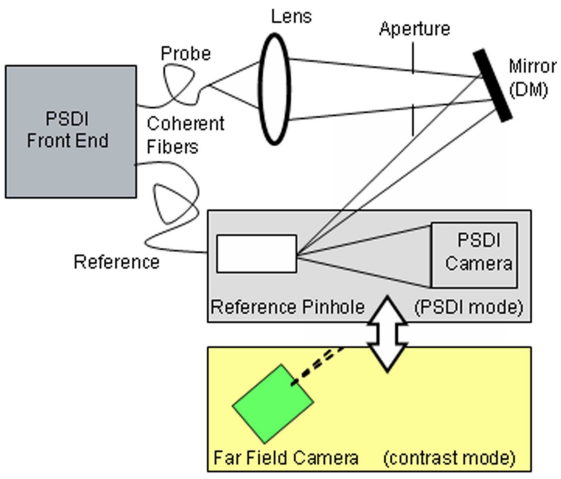

Figure 3.1: Simplified schematic of the ExAO testbed [26]. The testbed has two modes of operation: imaging and phase shifting diffraction interferometry (PSDI). In PSDI mode, the interferometer is used for metrology and wavefront control. Far-field images can be captured in imaging mode. The deformable mirror can be replaced with a fold mirror for more basic tests (See Chap. 4).

In interferometry mode, the testbed becomes an extremely accurate optical metrology system. The phase shifting diffraction interferometer (PSDI) was developed at Lawrence Livermore National Laboratory for metrology of aspheric optics for use at ultra-violet wavelengths [51]. In its original configuration the PSDI has an absolute wavefront accuracy of 100 pm. In the experiment described here, I estimate WFE to be 200 pm. A probe (or measurement) wavefront is injected from the upper single-mode fiber in Figure 3.1. This passes through the system and is focused onto a pinhole embedded in a super-polished flat mirror (the reference pinhole). Meanwhile, a coherent reference beam passes through the pinhole and interferes with the outgoing probe wavefront. The interference pattern is recorded by a CCD located in an arbitrary location along the optical axis. Using standard phase-shifting interferometer techniques, this produces a measurement of the fringe pattern at this location, which can then be converted to a measurement of phase and amplitude. This wavefront is then numerically propagated in two steps to the plane of interest. More information on the PSDI is located in Section 3.3.

Wavefront measurements are used to control the MEMS during closed-loop operations. The spatial resolution at the MEMS plane is limited by truncation effects due to an aperture at the reference pinhole. The effective resolution in the MEMS plane is $\sim 141\mu$m or 41% of an actuator. For closed-loop operation, programs in the interactive data language (IDL) are used to direct data acquisition (wavefront sensing with the PSDI), to direct back propagation calculations and to command the MEMS device through the MEMS driver. Before closed-loop operation, the alignment and voltage response of the system must be calibrated. Alignment is done by activating four known actuators on the MEMS and noting their position in a wavefront measurement. During voltage

calibration, the response of each actuator is measured and fit with a quadratic. The device is typically operated at a bias of 110 volts, and the calibration must be done with the same bias level. The MEMS model assumes linear superposition. The MEMS is controlled with 13-bit D/A conversion and amplification using a system developed by Red Nun Electronics Company. The smallest voltage step allowed with these electronics is 0.025 volts.

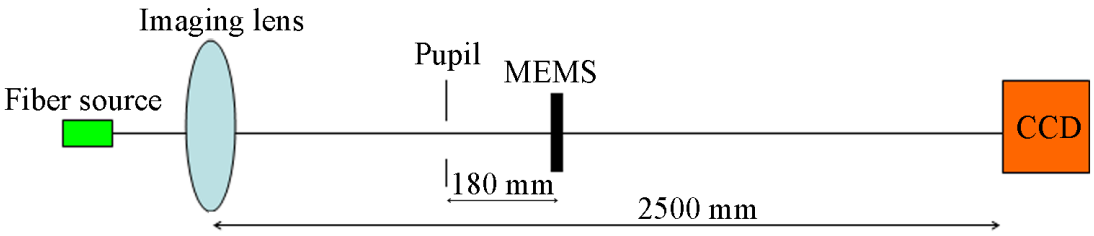

Figure 3.2: Unfolded layout of imaging mode. The system has a 10 mm aperture and an $f/\#$ of $\sim f/250$. The pupil is not conjugate to the MEMS, but the slowness of the imaging beam mitigates the effects introduced by the separation.

During imaging mode the probe beam from the PSDI is used as the source. An unfolded layout with distances is shown in Fig. 3.2. The laser source (532 nm) passes through an optical fiber and a high quality lens. The beam then passes through a pupil stop and reflects off the flat or a DM. The focal plane of the probe beam is located at the reference pinhole, which is replaced with the far-field camera for imaging mode. The far-field image is sampled at ~ 5 times the Nyquist limit. High-contrast measurements can be made directly in imaging mode when diffraction is suppressed. For diffraction suppression, current work uses a prolate spheroid shaped pupil [31] (see Section 2.3.1), which does not introduce phase errors into the system. A shaped pupil does not require an additional pupil or focal plane, thus keeping the optical system components to a minimum.

3.3 Phase Shifting Diffraction Interferometer

The Phase Shifting Diffraction Interferometer (PSDI) was designed for real time metrology for the manufacturing of aspheric mirrors needed for Extreme Ultraviolet Lithography (EUVL) applications. This challenging application required metrology with 100 pm accuracy [51]. The PSDI is a proven optical metrology technology that can provide the absolute wavefront accuracy needed for high-contrast imaging. Although the PSDI is not a feasible solution for the final instrument because of its size and complexity, it does provide a stable and accurate platform for component testing.

In this section, I provide a detailed description of the PSDI methodology as it relates to the current set up. This review relies heavily on work done by Gary Sommargren and Don Phillion.

3.3.1 Description

The layout of the ExAO testbed is shown in Fig. 3.1. As shown, the PSDI front end feeds the measurement and reference legs of the system. The front end itself is shown in Fig. 3.3 [52]. A doubled YAG 532-nm laser is the light source for the PSDI. It has 2 watts of power, but before entering the ExAO testbed, a 90-10 split reduces the power to approximately 200 mW. The laser was chosen for its short coherence length. A coherence length of about 5 mm causes most secondary reflections in the system (particularly from the beam cube and compound focusing lens) to be incoherent with the main beam. These incoherent images can reduce contrast in the fringe measurement but do not introduce errors into the phase. After entering the enclosure, the beamline is polarized with a $\lambda/2$ wave plate. A polarizing beam cube divides the beam into reference and measurement beams. The relative power of these is controlled with the wave plate.

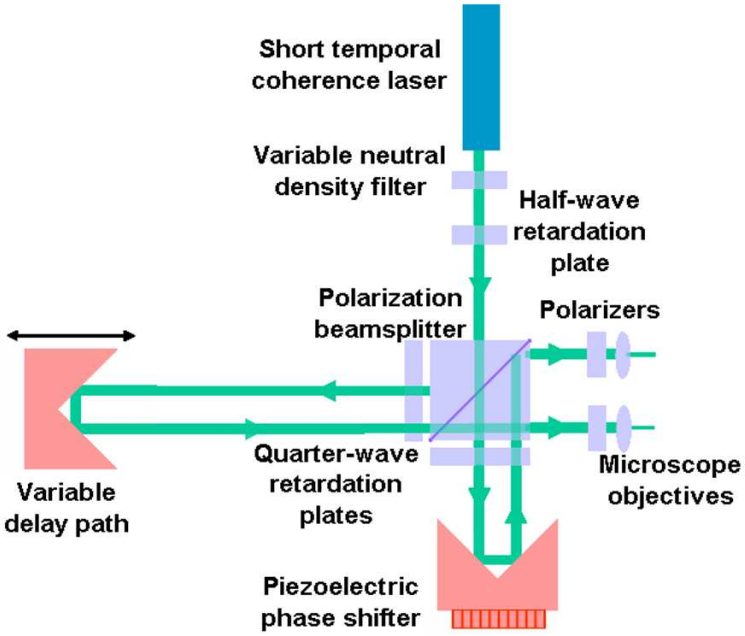

Figure 3.3: The front end of the phase shifting diffraction interferometer produces two phase shifted coherent beams. The measurement (probe) beam is phase shifted and the reference beam travels the delay path.

The PSDI is a zero-path difference interferometer so that while the measurement beam traverses the testbed section of the system, the reference beam travels the delay leg to account for the path difference. In practice, the delay leg is longer than the physical distance covered by the measurement leg to account for the glass in the focusing lens. Some PSDI configurations have a fiber delay leg which can significantly reduce the size of the system. The measurement leg includes a PZT phase shifter. Both beams are launched into single mode fiber optic cable. The wavefront quality before the fibers is unimportant because the fibers act as spatial filters [53]. After the light is launched into the fibers, polarization is changed with fiber polarizers. These polarizers compress and twist the fiber to induce an index of refraction change along a particular axis, thus changing polarization. When the beams are recombined later in the system they need to have the same polarization in order to interfere. The measurement beam is launched

from a bare fiber into the testbed system, effectively a 4 μm pinhole. It is brought to a focus on the ultra-flat reflective surface of the pinhole aligner. The reference beam is emitted from a 3 μm hole in the aligner. The focal spot of the measurement leg is 150 μm so the small amount of light not reflected by the reference pinhole is not significant. Both beams then propagate to the PSDI CCD where the phase and amplitude are calculated.

The phase at the CCD is calculated using a 12 bucket, $\pi/4$ phase step, least-squares, phase-shifting interferometry algorithm. The redundancy of the 12 bucket process makes the calculation more robust against errors like laser variability [52]. Unfortunately, the phase in the CCD plane is not of interest. Most interferometers re-image the pupil plane onto the CCD and those re-imaging optics introduce additional WFE. To avoid these errors, the PSDI uses lensless imaging. Numerical back propagation is performed using the ABCD matrix and a Huygens Integral Transformation. It is implemented using fast fourier transforms in two steps: from the CCD to the focal plane, and from the focal plane to the pupil plane [52]. In early tests, the paraxial approximation was used, but it was not accurate enough [51].

Most interferometers produce a relative measurement of phase that is dependent on the quality of the reference used. The reference beam of the PSDI is generated using the fundamental process of diffraction and is so nearly perfect that the PSDI provides an absolute measurement of wavefront error in the measurement beam. A λ-size aperture produces a perfect spherical wave over a specific numerical aperture (NA). For example, an aperture with diameter 2λ will produce a wavefront with $\lambda/10,000$ wavefront quality over a numerical aperture of 0.3 in the far-field [53], much larger than the NA required for these experiments. In its original form, the PSDI was used to test aspheric focusing optics, eliminating the need for the focusing lens and allowing the PSDI to measure

only WFEs introduced by the test optic. In the current system the PSDI measures the combined error of the flat or DM and the focusing lens. The focusing lens is a high-quality optic with approximately 10-nm rms WFE over a 150-mm aperture. We are only using a small portion in the center of the lens, and the flat or MEMS mirror will be a much more significant source of WFE. With a flat mirror in place of the DM, the system has a total rms WFE of less than 2 nm. Unlike a traditional adaptive optics system, the absolute measurement of the PSDI also ensures that non-common path error is not a problem.

3.3.2 Error in the PSDI

A rigorous compilation of the total WFE of the PSDI was presented in Sommargren et. al. [51]. The largest source of error is the surface roughness of the reference pinhole. In EUVL applications, 4 rotational averages were used to reduce this error to 50 pm. The next largest error source is caused by nonuniformities in the CCD pixel size and position (30 and 60 pm respectively). The PSDI is sensitive to these errors because of the numerical back propagation. Small misalignments in the system contribute a small amount of WFE. Adding in quadrature (assuming that the error sources are uncorrelated) the total WFE of the PSDI is 89 pm. This level of wavefront measurement is not required for current work, and the rotational averages are not used. Accounting for that, but keeping other error sources the same, I estimate wavefront error to be ~ 200 pm.

Measurement error can be dynamic if system components deform with time or temperature. In particular, if the input measurement fiber is misaligned, there is phase print through of the tilt fringes, and the error is much larger. At the end of each closed-loop run, an additional measurement is taken without any change in the system and used to calculate measurement error for that run. This measurement error is typically

between 0.15-0.20 nm rms phase. System stability also affects measurement error and is found to be 0.08 nm rms phase over a 38 minute period (See section 3.4.3). These numbers correspond well with estimates based on Sommargren et. al.'s calculations.

3.3.3 Resolution of the PSDI

The error of the PSDI is not sufficient to characterize performance. PSDI measurements are used to control the MEMS device making resolution of better than half of one of the MEMS actuators (340 μm per actuator) highly desirable. Far-field simulations are also generated from wavefront data and break down when not enough spatial frequency information is available. Resolution was calculated analytically based on the geometry of the system. Those calculations were confirmed by an experiment using a resolution target and a numerical simulation [54]. The analytical calculations for an earlier layout were presented by Sommargren in an internal memo [55]. Those calculations are elaborated and applied to the final layout in this section.

For simplicity, these calculations are done with the MEMS plane as the pupil plane, but the technique is the same if another plane is chosen. In part (a) of Fig. 3.4, the unfolded layout is shown, and the necessary geometrical parameters are labeled. The pupil has a radius of $a = 5$ mm, and is a distance $s = 2180$ mm from the focal plane where the reference pinhole is located. The PSDI CCD is located a distance $d = 815$ mm from the focal plane. The total number of pixels in the CCD is n^2, with $n = 1024$, and the pixel size is $p = 13$ μm.

The most basic limitation to resolution is sampling. An aperture of radius h in the focal plane can be treated as two point sources in a double slit experiment. One of the sources is the reference beam emitted from the pinhole at the center of the focal plane. The other is the light from the measurement beam being reflected by the super-polished

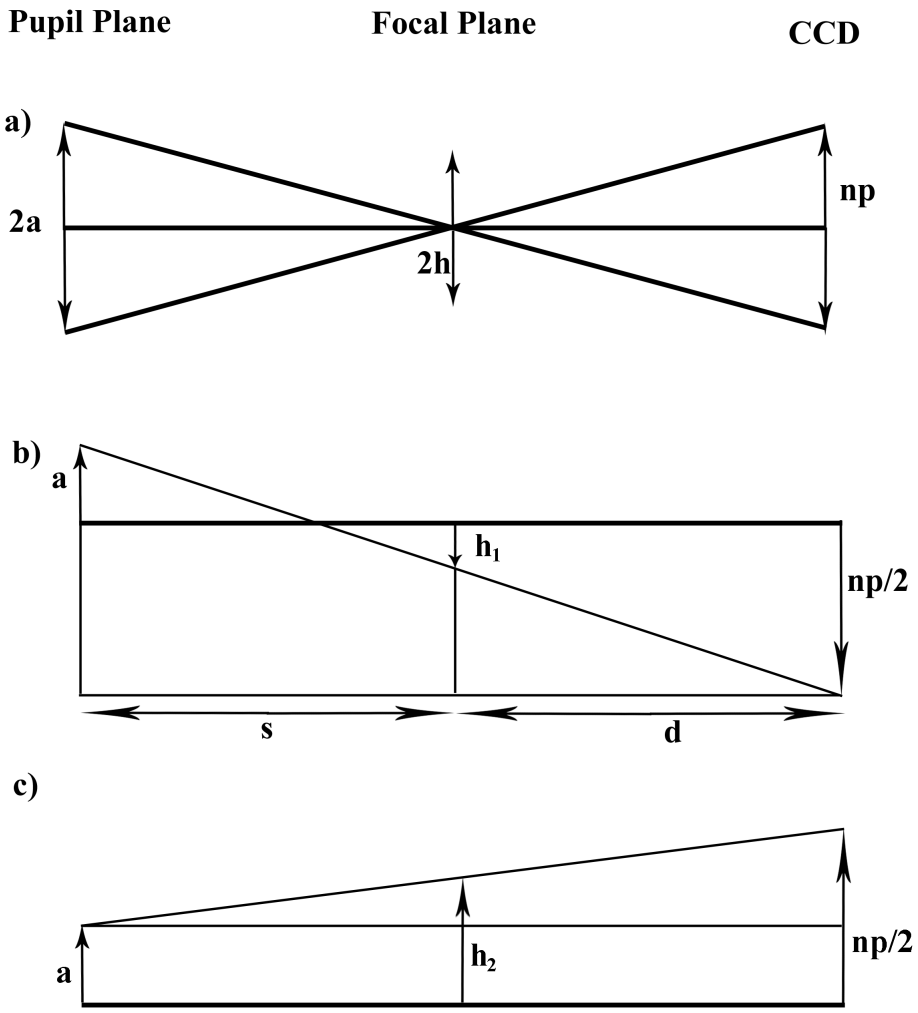

Figure 3.4: Top: An unfolded diagram of the PSDI system with appropriate geometric variables labeled. Middle: Diagram for calculating resolution without truncation of spatial information at CCD. Bottom: Diagram for calculating resolution with some truncation of spatial information.

pinhole substrate. These two point sources will interfere, thus producing a fringe pattern at the CCD. The separation of two maxima will be $\triangle x = d\lambda/h$, where λ is the wavelength of light. In order to meet the Nyquist condition, $\triangle x = 2p$. Resolution is defined, using the Rayleigh criterion, as $R = 0.61\lambda/NA$, where NA is the numerical aperture. We are interested in the resolution at the aperture plane, and using the paraxial approximation, $NA = h/s$, thus the resolution limited by sampling is $R = 1.22ps/d$. Based on the geometrical values of the current set up, $R = 42.4$ μm. However, if we calculate the corresponding size of the aperture at the focal plane, it has a radius $h = d\lambda/2p = 16$ mm. There is a physical aperture located at the reference pinhole of radius 5 mm. Using this value, $R = 0.61\lambda s/h = 141.5$ μm, indicating that resolution is not limited by sampling. This new limit caused by truncation at the reference pinhole is still better than half an actuator and sufficient for our needs.

It is also possible for truncation at the CCD to limit resolution. There are two methods for calculating a limiting h value due to CCD truncation. In method one, all of the spatial information is collected. Light diffracting from either edge of the aperture will still make it onto the CCD. That case is illustrated in part (b) of Fig. 3.4. Two similar triangles, one with base $s + d$ and one with base d, identify a relationship, which can be solved for h,

$$h_1 = np/2 - \frac{d(a + np/2)}{s + d}.$$

Using this formula, we calculate a $R = 203$ μm with a corresponding h_1 of 3.48 mm. This smaller value of h indicates that resolution could be limited by truncation at the CCD. However, in this case, requiring all spatial information to be collected is overly stringent [55]. The calculated h_1 value does provide insight into far-field simulations made with the measured wavefronts of the PSDI. In the focal plane, 3.48 mm corresponds

to a frequency of 3.0 mm^{-1}. Far-field simulations with the MEMS plane as the pupil plane will start to break down at $\sim 30\lambda/D$.

In the second method for calculating h, only the diffracted light from one side of the aperture is required to make it on to the CCD. Using similar triangles again,

$$h_2 = np/2 - \frac{d(a - np/2)}{s + d}.$$

In the current set up, $h = a$, making this type of truncation a mathematical impossibility. Resolution is not limited by truncation at the CCD; it is limited by the physical aperture in the focal plane. The most obvious effect of this truncation is ringing in the wavefront measurements.

3.4 MEMS deformable mirrors

Traditional, macroscopic DMs will not meet the technical requirements of many new adaptive optic (AO) systems. For example, in high-contrast or high-resolution AO, DMs with $>$ 2000 actuators will be required [48], but currently, the largest commercially available traditional DM has $<$1000 actuators. Traditional DM technology is scalable but at a cost of approximately \$1000/channel. These DMs are made by attaching macroscopic actuators to a thick glass facesheet with an actuator spacing on the order of millimeters. A high-actuator-count device would be quite large, significantly increasing the cost of the optical system. New applications for adaptive optics, such as ophthalmic instrumentation, do not require a large number of actuators but are more feasible with a smaller, less expensive deformable mirror than traditional technology can provide [56]. Future AO systems may also operate in open-loop control systems, and the hysteresis of traditional mirrors will make this difficult.

MEMS DMs are a promising technology to meet the technical requirements

of advanced AO systems. Batch processing techniques, such as those pioneered in the integrated circuit industry, are used to produce many DMs at once, greatly reducing the cost. Typically these devices are made with lithographic techniques, which layer polysilicon with sacrificial phosphosilicate [50] glass layers to produce individually addressable actuators made of polysilicon using the mulit-user MEMS process (MUMPS) or the Sandia Ultra-planar, Multi-level MEMS Technology (SUMMIT) process [57]. The inter-actuator spacing is on the order of 100s of microns greatly reducing the size of a typical DM, even one with a high actuator count. Each actuator is composed of two parallel plate electrodes separated by a dielectric (usually air). When a voltage is applied, the two electrodes are compressed closer together. The upper electrode is supported by springs, which provide the restoring force for the actuator [57]. Figure 3.5 is a diagram of actuator components [58].

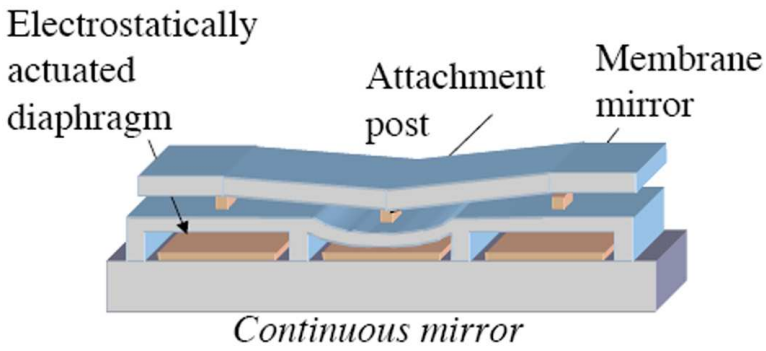

Figure 3.5: A diagram showing the components of a MEMS actuator [58]. Each actuator is composed of two parallel plate electrodes separated by a dielectric (usually air). When a voltage is applied, the two electrodes are compressed closer together. The upper electrode is supported by springs, which provide the restoring force for the actuator. The top surface of the MEMS is a continuous facesheet.

Traditional DMs are a more mature technology, but MEMS DMs are becoming a more viable option as increased testing provides feedback to device development. While MEMS DMs do not have hysteresis like traditional DM technologies, yield and actuator

uniformity can be a problem. Driver technology for MEMS devices is also being tested and contributes significantly to the cost of a MEMS system. In the future, MEMS will use integrated circuit technology to solve the driver problem and reducing the cost from \$10/channel to \$1/channel [56]. MEMS DMs are critical to GPI, and the testing I have done indicates that using a MEMS DM for high-contrast imaging applications is feasible.

We have tested a total of ten 1024-actuator deformable MEMS mirrors fabricated by BMC [50] from several different fabricating runs. While a future exoplanet imager will require more actuators, the 1024 device is the largest commercially available MEMS device. Characterization and performance testing of these devices have provided feedback to the design and specification of the larger device. We have characterized voltage response, actuator uniformity and device stability, as these characteristics will affect closed loop performance. MEMS DM technology for ExAO applications are still under development, but over these ten devices, we have seen a dramatic improvement in unpowered flatness and yield, which will be crucial for the 4000 actuator device. The 1024 mirrors have 4 inactive actuators by design (they are wired to ground). The actuators are spaced 340 μm apart with a continuous face sheet as the top surface. Due to residual manufacturing stress, the top surfaces of these devices have curvature. Early devices had $>$ 200 nm rms unpowered WFE, but more recent devices have had as little as 50 nm rms unpowered WFE.

In general, defective actuators occur during the manufacturing process rather than failing during operation. A combination of high humidity and high voltage can produce oxidation in individual actuators which will eventually limit the performance of those actuators [59]. To avoid humidity damage, the device can be sealed under a glass window, or only operated in a controlled laboratory environment. An unpowered

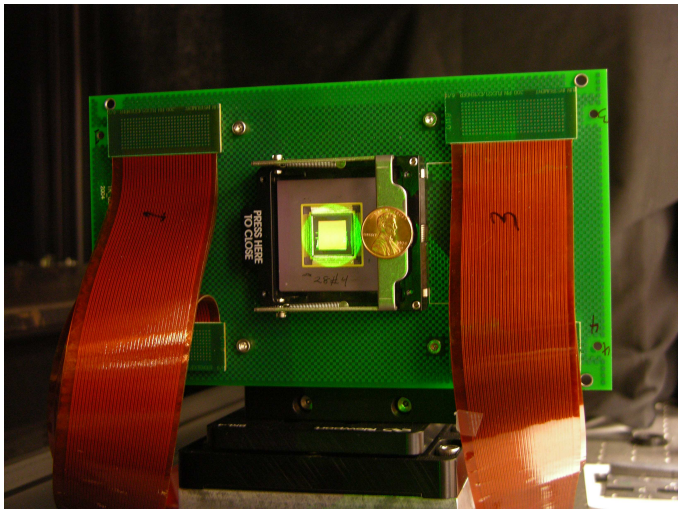

Figure 3.6: The 1024 actuator MEMS device made by Boston Micromachines Corporation, shown on the testbed with a penny for scale.

device is not damaged by high humidity, but if condensation occurs, the mirror must be dry before it is activated. A windowed device does not have reduced closed-loop performance. Two of the devices tested, including the device with the best closed-loop performance, have windows. Contrast measurements with a windowed MEMS can be limited by ghost images. 'Snap-down' can also damage actuators. This occurs when an actuator has too much displacement and the electrical attraction compressing the actuator overcomes the mechanical force that allows the actuator to rebound. These actuators will be stuck in the maximum displacement position. Actuators damaged by humidity and high-voltage will be stuck in the no displacement position. Two early devices were damaged by humidity at the LAO but no damage due to snap-down has occurred.

The MEMS is controlled with 13-bit D/A conversion and amplification using a system developed by Red Nun Electronics Company. The smallest voltage step allowed with these electronics is 0.025 volts for the current configuration. This corresponds to a phase step of 0.18 nm. The driver boards for many-channel systems like this are also

under development. It is critical and tedious to ensure that the mapping through the driver electronics is accurate. Minor damage to the boards can be difficult to detect and will negatively affect closed-loop performance.

3.4.1 Voltage Response

One limitation of MEMS DM technology is the device's limited stroke, especially compared with macro-DM technology. Currently most applications will have to operate a MEMS DM in tandem with a low-order standard DM. The low-order DM will provide most of the correction while the MEMS DM provides higher spatial resolution correction (woofer/tweeter configuration) [48]. The MEMS devices tested with the voltage limits used have particularly limited stroke (about 1 μm). However, the more limited stroke of these particular devices is not a concern because other device geometries with larger actuator spacing have demonstrated 4 μm of stroke [50]. Those geometries will be used for the future 4000-actuator device needed for GPI.

In practice, we find that MEMS stroke depends on the position of neighboring actuators, as expected for their relatively broad influence functions, which have approximately 26% crosstalk [60]. For example, a 3 by 3 array of actuators will have more displacement at a given voltage than a single actuator at the same voltage. In Fig. 3.7, this difference is indicated by the 3 dotted versus solid lines. In a typical AO system, the DM is operated at a bias to correct both positive and negative WFEs. The entire device is set at an intermediate voltage and actuators are moved by varying their voltage about the bias. We typically operate at a bias of 110 volts, that voltage being midway in our operational displacement. We set a maximum voltage limit to 160 volts, to prevent snap-down both in software and on the voltage power supply. An imbalance between the electrostatic force of activating an actuator and the mechanical restoring force causes

stroke at a bias to be reduced. Figure 3.7 summarizes the results of testing the stroke of a particular MEMS device for these situations [61]. For this test, 4 actuators were acti-

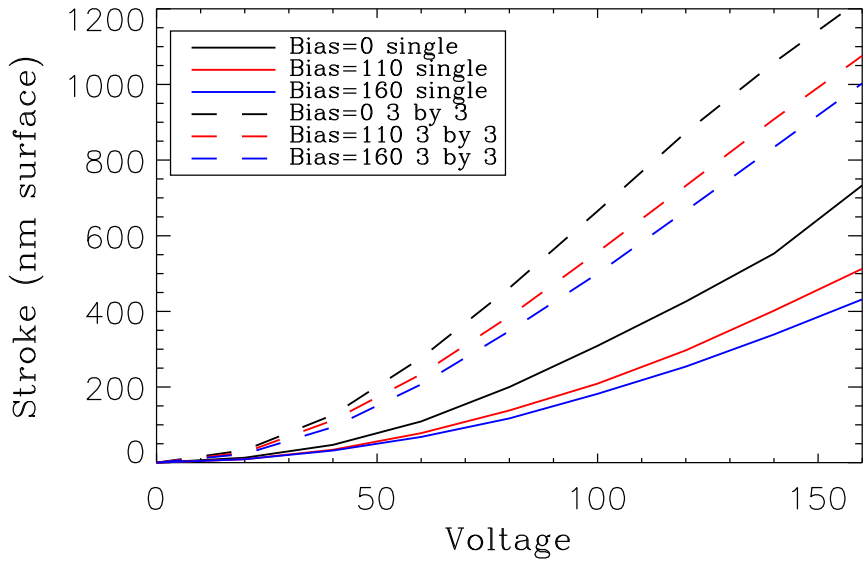

Figure 3.7: Stroke of a device measured with 0, 110, and 160 volt bias for an individual or group of actuators [61]. More stroke is achieved when actuators move together without a bias voltage.

vated at several incremental voltages, and their displacement relative to the flat surface of the MEMS was measured with a Zygo interferometer. The test was also done with a set of adjacent actuators moved in a 3 by 3 box. Both tests were done with a bias voltage of 0, 110 and 160 volts. In Figure 3.7, the resultant curves have been re-centered so that 0 displacement is at 0 volts rather than at the bias voltage. In typical operations, these devices achieve about 1 μm of stroke with our operational parameters, similar to the measured response of the 3 by 3 array because actuators are not significantly displaced from their neighbors during closed-loop. The 'snap-down' effect is caused by too much displacement, not too much voltage. There is potential to increase the stroke of the device by increasing operational voltage above the current 160 volt maximum, while staying within the range of acceptable displacement. Because additional stroke was not

required for our tests, increasing maximum voltage was not investigated.

MEMS actuators have a non-linear response to voltage that varies on an individual device and between devices. We calibrate the voltage response of every actuator on a device. In this test, one actuator in each 4 by 4 array of actuators on the device is tested at varying voltages cyclically until all of the actuators are tested. There are 16 frames for each voltage level, with 64 actuators tested in each frame. A few actuators have a particularly irregular response and this could be an issue for closed-loop high-contrast operation. These irregular actuators are discussed in greater detail in the next section. In early tests the average voltage response of four actuators was used to calibrate the entire device. Performance was improved, particularly for irregular actuators, by calibrating individual responses.

3.4.2 Actuator uniformity

Operating in closed-loop mitigates the effect of small variations in voltage response between actuators. On the most recent device, the variation in maximum displacement at 160 volts is less than 5% (excluding the outer two rows and columns of actuators), which is well within our ability to flatten. Irregular actuators, however, are unable to achieve the desired position, regardless of number of iterations, producing an in-band fitting error that limits closed-loop performance. I have identified three categories of such actuators: no-response (or dead), low-response and coupled. We typically refer to the yield of a MEMS device as percentage of working actuators. This number is particularly important in high-contrast applications as no-response actuators scatter light into the dark hole region. Actuator uniformity refers to the variability of all 'working' actuators including low-response and coupled actuators.

Figure 3.8 is a representation of actuator yield and uniformity in three tested

devices [60]. No-response actuators are marked in red, other irregular actuators in yellow and normal actuators are white. The three figures exclude the outer 2 rows and columns, which are outside the aperture and difficult to characterize. The left device was received in November 2004. It had limited performance due to the number of irregular actuators and was operated over a smaller aperture because of the number and placement of no-response actuators. The middle and right devices were received in February and October of 2005. The two no-response actuators in the top middle of all three devices are wired to ground and are excluded from the following statistics. The oldest device has 96.9% normal actuators (33 irregular) while the most recent device has 99.5% normal actuators (5 irregular). Only 94.1% of actuators were normal (60 irregular) in tests of the segmented device published by Baker et. al. in 2004 [43, 62]. This dramatic improvement in actuator yield and uniformity has allowed improved performance and made MEMS deformable mirrors a feasible technology for high-contrast applications.

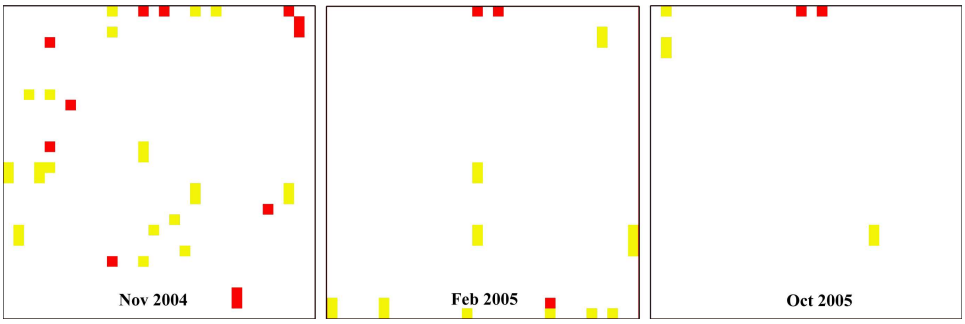

Figure 3.8: Irregular actuators are identified for the working region of three MEMS devices [60]. Red indicates a no-response actuator, yellow a 'working' irregular actuator, and white is a normal actuator. The Nov 2004 device had limited performance due to the number of irregular actuators and was operated over a smaller aperture because of the number and placement of no-response actuators. There has been a dramatic improvement in both yield and uniformity in the Feb and Oct 2005 devices. The two no-response actuators in the top middle of all three devices are wired to ground.

With fewer no-response actuators the effects of other irregular actuators have become more apparent. Careful characterization of irregular actuators has led to im-

proved control and provided engineering feedback to the manufacturer. As mentioned above, I have categorized irregular actuators as low-response or coupled. Low-response actuators can be actuators that only move with their neighbors or actuators with reduced voltage response. The February 2005 device in Figure 3.8 has a low-response actuator that only moves with its neighbors, right in the center. After flattening, this actuator is offset from its neighbors by about 20 nm. In previous tests with this device [63], more irregular actuators were apparent due to errors in the driver electronics, but this electronics problem has since been corrected. Coupled actuators affect voltage calibration. For example, the October 2005 device has two coupled actuators. When a coupled actuator's voltage response is tested individually there is no displacement after the bias voltage because the other actuator in the pair is set to the bias during the test. If coupled actuators are tested simultaneously, the voltage response is normal. (See Fig. 3.9.) A coupled actuator will move to the lesser of the voltage applied to the pair.

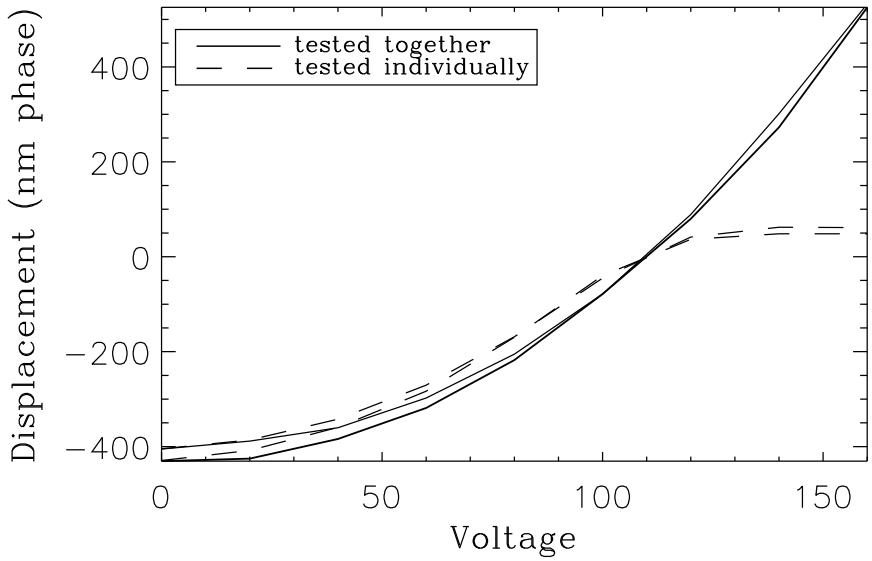

Figure 3.9: Voltage response of two coupled actuators tested individually and together, with a bias voltage of 110 volts [61].

3.4.3 Stability

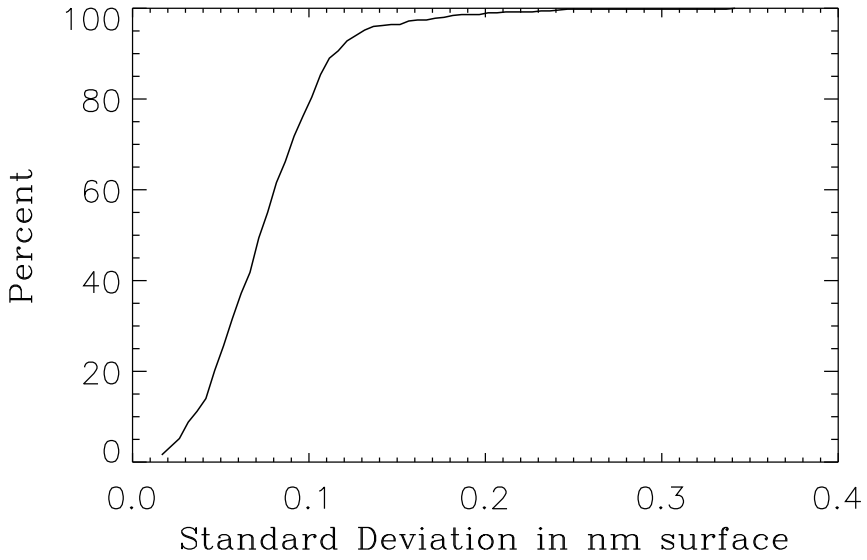

Figure 3.10: Curve of growth for stability data. Of the 500 actuators tested 97% have stability of better than 0.16 nm (standard deviation of surface over 60 measurements taken in 38 minutes).) Figure courtesy of Katie Morzinski [60].

Current closed-loop tests use the PSDI as the wavefront sensor, which limits frame rate. As a result, excellent stability for both the system and the MEMS is required. To test MEMS stability, a flattened shape is applied to the MEMS device and successive wavefront measurements are taken every 38 seconds (the minimum time to complete a PSDI measurement) for 60 iterations. Short term stability is measured over 9 minute intervals within the long term stability test. The shorter time scale is comparable to typical closed-loop operation times. The variation of each actuator in phase from its initial position is calculated with piston and tip/tilt removed. This analysis was done over approximately half of the device. The PSDI stability was measured to be 0.08 nm rms phase by replacing the MEMS with a flat mirror. The average long term stability of the MEMS was measured as 0.16 nm rms phase. On the shorter time scale the system is more stable with an average rms deviation of 0.13 nm rms phase for the

MEMS and 0.07 nm rms phase for the flat mirror [60]. Previous tests had indicated less stability [63] because of errors produced by the MEMS drive electronics, which have since been corrected. Figure 3.10 is a curve of growth showing that most of the actuators are quite stable. Of the 500 tested, 97% are stable to better than 0.16 nm rms surface over 38 minutes.

3.5 Summary

In summary, the ExAO testbed is nearly ideal for conducting basic, far-field measurements because of the built-in, accurate metrology of the PSDI and its low WFE. The metrology of the PSDI also allows characterization and performance testing of MEMS deformable mirrors. This testbed has also been used to test the spatially filtered Shack-Hartmann wavefront sensor. The lack of additional pupil or focal planes does limit diffraction suppression to shaped pupils and a future iteration will need to include additional optics for testing more advanced coronagraph concepts.

Chapter 4

High-Contrast Measurements without Active Wavefront Control

4.1 Introduction

Contrast in an image is fundamentally a question of measurement. In theory, the nulls of any diffraction pattern get infinitely close to zero or perfectly dark. In practice, wavefront error (WFE), CCD dynamic range and sampling effects prevent a perfect dark region from being achieved. Entering the high-contrast regime requires suppressing diffraction so a large null region is created and limiting or controlling wavefront errors [27] so that speckles do not fill in that region. (More information on how diffraction and WFE affect contrast is given in Section 2.2).

Planetary science has become a hot topic for astronomers with the discovery of more than 150 extrasolar planets [1]. Imaging planets is the next important scientific achievement but is technically challenging because of the high-contrast measurements required. A ground-based imaging system would look for young Jupiter-like planets that

are still warm with the heat of formation and would require contrasts of 10^{-6} to 10^{-7} in the near-IR [4]. There are space-based efforts to image earth-like planets which require the more challenging contrast of 10^{-10}.

Laboratory tests investigating the experimental limits to contrast are ongoing at several institutions including the Laboratory for Adaptive Optics (LAO). These early tests are without active control of WFE. Kasdin et. al. [64] have focused on pupil design and manufacturing limitations identifying numerous shaped pupil designs and demonstrating between 10^{-6} and 10^{-7} contrast at radii greater than 6 λ/D. Other experimental results have been obtained by Charborty et. al. [65] where they used a multi-opening Gaussian pupil and obtained contrast of 4×10^{-7} at 4.5 λ/D. Contrast in a diffraction-suppressed regime scales with wavelength squared [27] and this work was at a slightly longer wavelength. Thus, Charborty et. al.'s results would be closer to 10^{-6} contrast at wavelengths comparable to Kasdin et. al. and the work presented here.

While early experiments did not include wavefront control, wavefront errors cannot be ignored as they are still a major limit of achievable contrast. I have found controlling WFE to be more challenging than suppressing diffraction. In the baseline experiment presented here, wavefront error was minimized by optical design and construction rather than active control. After initial experiments, components for a high-contrast giant-planet imager can be tested in a well understood system capable of operating in the necessary regime. The accurate wavefront measurements of the phase shifting diffraction interferometer (PSDI) also allows the limitations of contrast to be investigated. Using these tools, we have achieved 6.5×10^{-8} over 8 degrees from 10 to 25 λ/D, demonstrating the usefulness of the Extreme adaptive optics (ExAO) testbed for high-contrast instrument development.

4.2 Experimental method

The ExAO testbed was designed with a minimal number of high-quality optics to ensure that end-to-end WFE would be small (< 1.5 nm rms). In initial, high-contrast measurements active wavefront control was not required, allowing experiments to focus on suppressing diffraction, understanding the high-contrast regime and developing experimental methods for high-contrast imaging (i.e. controlling scattered light). In imaging mode, the testbed consists of a laser source (532 nm) passed through an optical fiber and a high-quality lens. The beam passes through a pupil stop, reflects off a flat mirror, and

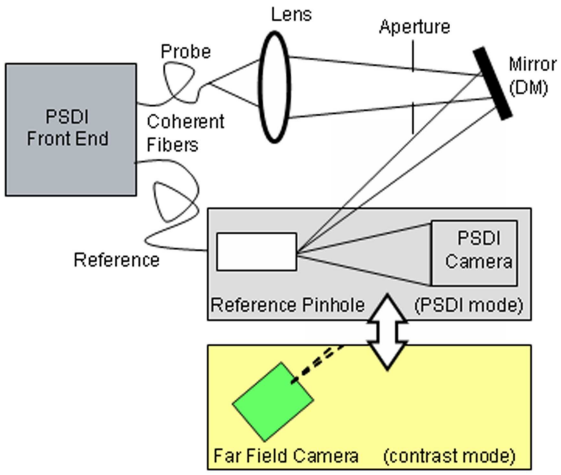

Figure 4.1: Simplified schematic of the ExAO testbed [26]. The testbed has two modes of operation: Imaging and phase shifting diffraction interferometry. The fold mirror in the system can be replaced with a deformable mirror for active wavefront control.

is imaged onto a CCD sampled at ~ 5 times the Nyquist limit (See Fig. 4.1 also shown in Chapter 3). Diffraction is suppressed along one axis with a prolate spheroid shaped pupil [31], shown in Fig. 2.3. The characteristic x-pattern with diffraction suppressed along the horizontal axis of the far-field image is also shown. The shaped pupil is easy to use and produces a region of high contrast sufficient for laboratory testing while not introducing additional phase aberrations. More information about suppressing diffraction is given in Section 2.3.

In PSDI mode, the testbed becomes an extremely accurate optical metrology system [51]. The PSDI was developed at Lawrence Livermore National Laboratory for metrology of complex aspheric optics. Briefly, a probe wavefront is injected from the upper, single-mode fiber shown in Fig. 4.1. This passes through the system and is focused onto a reference pinhole embedded in a super-polished flat mirror. Meanwhile, a coherent reference beam passes through the pinhole and interferes with the outgoing probe wavefront. The interference pattern is recorded at a CCD located at an arbitrary location along the optical axis. Using standard phase-shifting interferometer techniques, this pattern produces a measurement of the phase and amplitude at this location, which can then be numerically propagated to the plane of interest, such as the pupil plane. The resolution of the PSDI is limited by the aperture of the reference pinhole (in the focal plane). The effective resolution in the 10-mm aperture plane is ~ 155 microns [26]. More information about the PSDI is given in Section 3.3.

Contrast is defined as the ratio of the intensity in the region of interest (ROI) to the core intensity and can be measured directly in a far-field image. There are several error sources in high-contrast imaging that must be reduced to achieve good results: insufficient dynamic range, scattered light from the optical system, and CCD saturation effects. The CCD in the ExAO system has a dynamic range of approximately five orders of magnitude (including noise). A contrast measurement of $10^{-6} - 10^{-7}$ can only be made as a composite of two or more images. Typically an unsaturated and a saturated image that are separated by 4 orders of magnitude via neutral density (ND) filters and integration time are used. Several images taken with less ND can be used to better understand the region connecting the core and wings. The ND filters are inserted into the PSDI front-end right before the measurement beam is launched into the fiber. Small

amounts of wedge in the filters will change coupling of light into the fiber, varying the attenuation from the filter. This effect is minimized by keeping the fiber launchers well aligned (they are temperature sensitive) and by putting the ND filters close to the launchers. For my work, the effect was still significant, and a power meter was used to characterize the attenuation caused by the ND for every experiment in real time. The ND filters and laser power were adjusted to return an attenuation of 10^3 for the unsaturated image. I also ran tests to determine the power variability in short exposures (either variability in the laser power or in the shutter speed) and chose our integration times to fall within the region of low variability. The testbed is housed in an opaque enclosure, and scattered light from elements in the optical path must be controlled. We tested our control over scattered light by comparing dark frames where the laser was shuttered to dark frames where the laser was blocked elsewhere in the system. The enclosure and small beam size also reduce air turbulence or bench 'seeing', which was not a problem in these experiments. When the ND filters are removed and the integration time is increased, the CCD is highly saturated. This effect is controlled by co-adding short exposures for longer integrations and using a focal plane mask. The slow $f/\#$ of our system (effectively $f/250$) allows us to move the far-field camera approximately 15 mm behind the focal plane without loss of contrast. A mirrored beam block is introduced at the focal plane to block the core, but not the wings of the point spread function (PSF). The position of the block is optimized by hand to minimize the amount of bleeding from the core, while still measuring the contrast at an inner working distance (IWD) of approximately 8 λ/D. In simulation, shaped pupils can achieve a better IWD, but our system was not designed for this type of optimization, as the final ExAO instrument will use a Lyot coronagraph for diffraction suppression.

Figure 4.2 is an image of the unsaturated core overlayed on the saturated image where the core would be if it were not blocked by the focal plane mask. The x-shape is characteristic of the shaped pupil, which produces a dark region along the horizontal axis of the image. Note that the unsaturated image is plotted on a log scale while the saturated image is on a linear scale. For analysis, each data set of 10 frames is averaged, and the corresponding averaged dark frame is subtracted. Each image is then scaled according to the measured attenuation from the ND and the integration time in order to be comparable with the saturated image. All of the images are normalized to the peak of the scaled unsaturated image.

4.3 Results

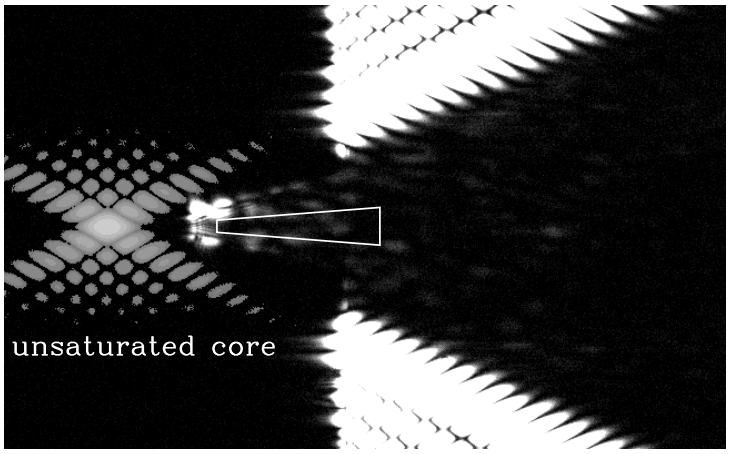

Figure 4.2: An image of the unsaturated core overlayed on the saturated image where the core would be if it were not blocked by the focal plane mask [26]. The boxed area indicates the region of interest from $10 - 25\lambda/D$. These images are superimposed with different scales.

The two modes of testbed operation correspond to two data types. Wavefront data are used to simulate far-field measurements and to verify overall WFE. Far-field measurements are used to directly measure contrast. Achieving better than 10^{-7} contrast

was a key goal, but it was also important to identify limitations to improved contrast. Future tests will expand on the methods used in this experiment. The increased complexity of active wavefront control will introduce errors. The identification of errors in the baseline experiment will provide insight as we build up to the more complicated version. Limitations to contrast will fall into two categories: shaped pupil performance and wavefront errors.

The dark region in the saturated image is clearly visible on the right hand side of Fig. 4.2. In the region from $8 - 15\lambda/D$, the radial average contrast over 8 degrees is 1.3×10^{-7} with an intensity variation of 1.0×10^{-7}. Over the larger region from $10 - 25\lambda/D$, the radial average contrast is 6.5×10^{-8} with an intensity variation of 2.9×10^{-8} (see the region indicated in Fig. 4.2) [26]. A substantial region in the PSF has better than 10^{-7} contrast in visible light, meeting the specifications for a current generation ground-based planet imager. The noise floor due to scattered light and CCD noise is measured to be below 10^{-8} behind the focal plane mask in the saturated image. It should be emphasized that the system is not noise limited (see Fig. 4.4).

4.3.1 Shaped pupil performance

When examining shaped pupil performance, there are two error sources to consider: design and implementation. The design will limit how much and where diffraction is suppressed, while the implementation will limit how close to optimal the physical pupil performs. Experimental far-field data from different shapes made with the same manufacturing technique, and the same shape made with different techniques were compared to examine both of these error sources. Edge quality measurements of shaped pupils and simulations complete the data set.

The most basic aperture shape is a circle, which produces an Airy pattern in

the far-field. Even in this simple case, some small regions of high contrast are produced in the nulls of the pattern. In practice, sampling and WFE make it difficult to achieve the desired contrast even over those smaller regions. Ideally, a larger symmetric region would be produced. Traditional apodizers can achieve this type of suppression, but at the contrast levels we are interested in, the manufacturing of the apodizer is limiting. Shaped pupils, also known as binary masks, are easier to manufacture and a good choice for testbed experiments. The design of shaped pupils is not new; Jacquinot and Dossier [30] give a description of early efforts in this area. With advances in computing and manufacturing, these designs can be further optimized and realized [32]. I chose a simple single opening prolate spheroid pupil for my tests. Fig. 4.3 is a comparison of experimental far-field data taken with a circular aperture and a prolate shaped pupil. In the $10-25\lambda/D$ region, the circle has a contrast of 1.2×10^{-5}, with an intensity variation of 1.4×10^{-5}. The prolate pupil has a performance almost two orders of magnitude better and is more uniform over the same region. Even in the nulls of the radial average plot for the circle, the contrast improvement of the prolate shaped pupil is apparent.

After the shape of the pupil is chosen, contrast can still be limited by implementation. The 10-mm diameter shaped pupil was designed to have contrast of 10^{-10}, but a specification error lead to a deviation of 0.02-mm rms from the desired points defining the opening. In simulation, the resulting loss of contrast from this error is significant ($\sim$ 2 orders of magnitude) but below the loss due to WFE (see Fig. 4.6).

The performance of a shaped pupil is also affected by its edge quality. Pupils manufactured with machining and lithographic etching were tested. Fig. 4.4 is a composite of radial averages from three images for each pupil. The normalized intensity of the unsaturated core of the etched pupil result does not quite align with the ROI

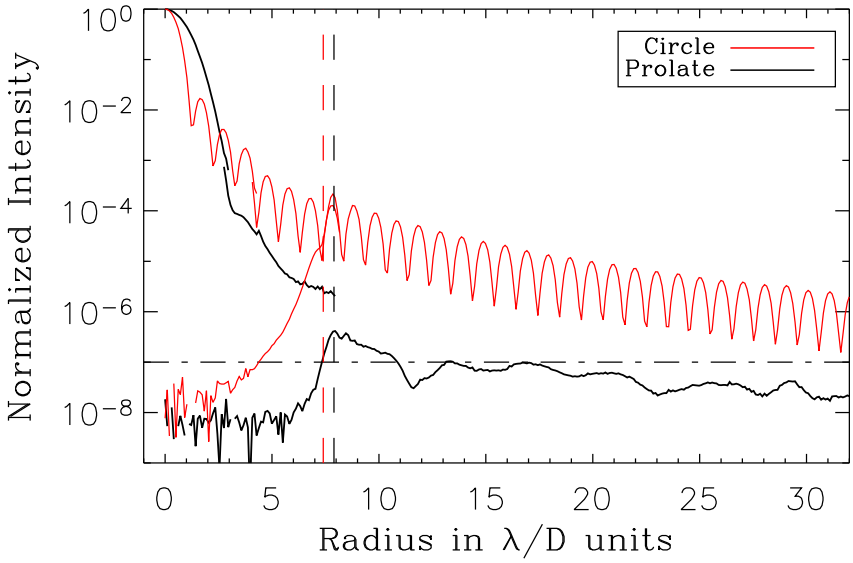

Figure 4.3: Composite, radial-average, normalized-intensity, far-field measurements made with the etched prolate and circular shaped pupils. The vertical lines indicate the edge of the focal plane mask in the two tests. The prolate measurements do not align as well because of saturation in the intermediate image. The prolate pupil performs almost 2 orders of magnitude better than the circular pupil. In contrast measurements with the flat mirror measurement noise is $\sim 10^{-8}$ as seen behind the focal plane mask. The system is not noise limited.

measured in the saturated image due to saturation in the second image of the core composite. Over the ROI, the etched mask has an improvement of approximately 0.5 orders of magnitude over the machined mask. For achieving 10^{-6} contrast, the machined mask is more than adequate at our level of WFE and considerably less expensive to make. Comparing microscope images of the masks, the machined pupil has an rms edge quality roughly 3 times larger than the etched pupil. Wavefront quality is the same for both measurements, indicating the machined pupil is limited by edge quality.

4.3.2 Effects of wavefront error

I also investigated the effect of WFE on high-contrast measurements. Once diffraction is suppressed, contrast can be limited by wavefront errors. Using the PSDI, I

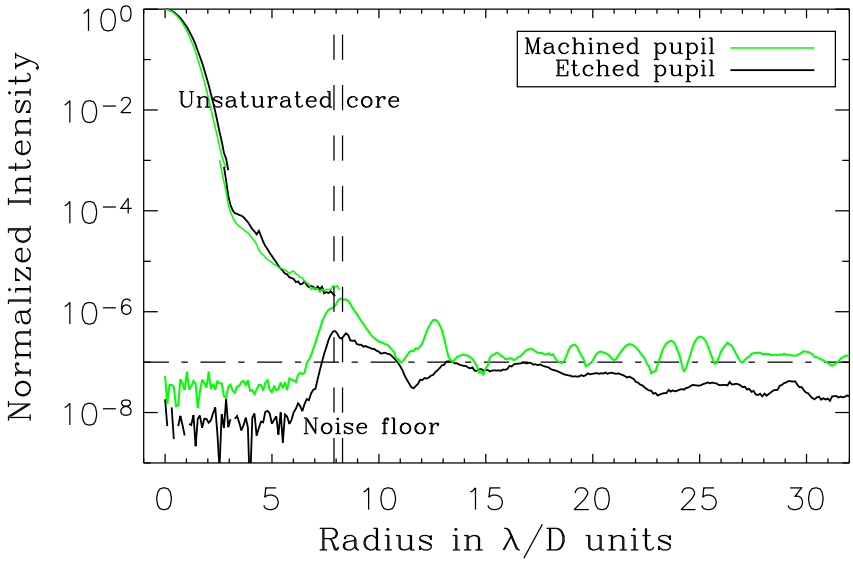

Figure 4.4: Composite, radial-average, normalized-intensity, far-field measurements made with the etched and machined shaped pupils [26]. The vertical lines indicate the edge of the focal plane mask in the two tests.

can accurately measure wavefronts and use the measurements to simulate expected far-field performance. This experiment has a total rms WFE of 1.5 nm. That error breaks down to 0.5-nm astigmatism, 0.5-nm 'ringing' (an artifact from the measurement), 0.3-nm spherical, 0.94-nm other mid-frequency and 0.7-nm high-frequency aberrations [26]. The truncation effect at the PSDI reference pinhole, which causes ringing in the wavefronts, also causes the far-field simulation to break down at approximately 26 λ/D. To test if contrast is limited by WFE, a series of simulations were done. Figures 4.5 and 4.6 are a summary of those results.

To simulate far-field measurements, I used measured WFE and generated a simulated mask from the points used to manufacture the physical mask (with the specification error included). The simulated mask does not include edge roughness, and amplitude errors are assumed to be insignificant. Radial averages over the ROI are plotted in Fig.4.5 for the experiment and a simulation using measured WFE. Good cor-

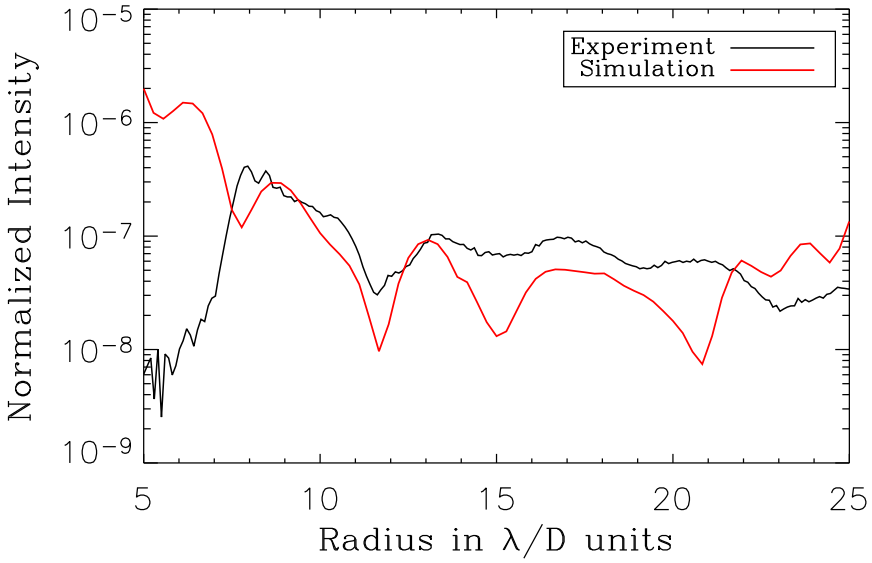

Figure 4.5: Comparison of experimental results with a simulation from measured wavefront error. The simulated mask does not include edge roughness, and amplitude errors are assumed to be insignificant. Good correspondence between experimental and simulated contrast indicates that edge roughness is not a significant factor with the etched mask.

respondence between experimental and simulated contrast indicates that edge roughness is not a significant factor with the etched mask. In Fig. 4.6 simulations using the flawed shaped pupil mask are compared with the perfect mask for varying amounts of WFE. Both simulations using the measured phase (black lines) achieve the same level of contrast indicating that the current level of WFE is the limiting factor to improved contrast. If WFE were reduced to 0.35 nm rms (red lines) the perfect mask would have similar performance to the flawed mask except at large angles indicating that while WFE remains a large error source, mask quality would also limit performance. When comparing performance without phase errors (the two blue lines), the perfect mask would perform several orders of magnitude better than the flawed mask. Simulations indicate that significant mask errors need to be avoided to achieve better than 10^{-8} contrast. To operate in the contrast regime of 10^{-10}, WFE and mask quality will be critical. In the contrast

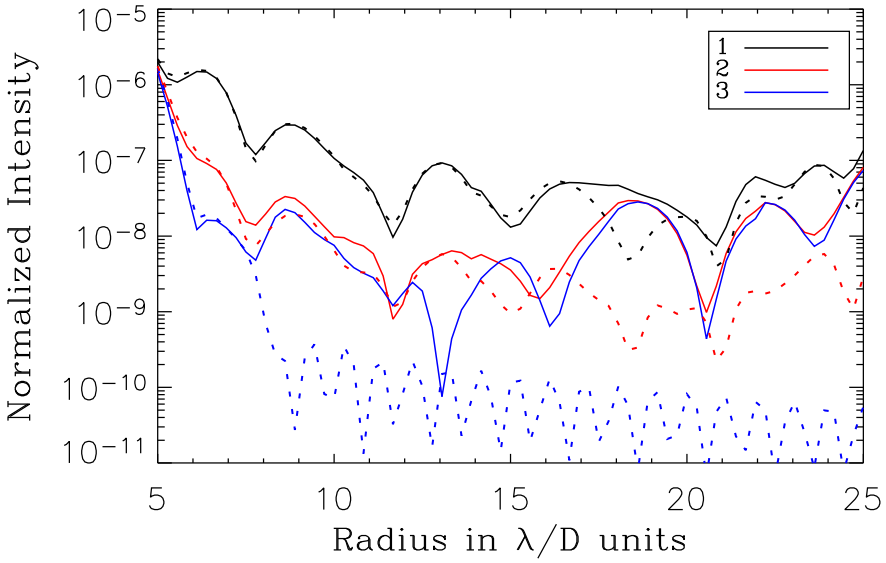

Figure 4.6: Comparison of contrast with flawed pupil mask and the perfect pupil mask with varying amounts of WFE. The solid lines are simulations using a shaped pupil mask with the same specification error as the physical mask and the dotted lines are simulated with the perfect mask. The lines in black (1) are far-field simulations using the experimentally measured phase. The lines in red (2) are simulations with the WFE reduced to 0.35 nm RMS. The lines in blue (3) are simulations with no WFE.

regime needed for our experiments, however, WFE is the more prominent error source.

4.4 Conclusions

I have demonstrated that better than 10^{-7} contrast in visible light can be achieved in a laboratory setting with low-wavefront error and an etched shaped pupil. In the contrast regime of our tests, low WFE is more critical and more difficult to achieve than producing an adequate pupil for diffraction suppression. For the 10^{-6} contrast regime an inexpensive pupil could be substituted, provided that WFE were adequately controlled. Any practical imaging system will have more WFE than the current system, and the obvious next step is to implement active wavefront control. The ExAO testbed can operate in the contrast regime needed to test deformable mirror technology and

other components needed for a future extrasolar planet imager.

Chapter 5

Closed-Loop Performance of a MEMS Deformable Mirror

5.1 Introduction

The detection of over 150 extrasolar planets [1] has placed planetary science at the forefront of astronomy. Most extrasolar planets have been detected using radial velocity techniques, which measure the doppler shift of the parent star that is produced by the gravitational pull of a planet. These techniques probe only about 15% of the orbital parameter space of our solar system [66]. This means that planets of the size and in the position of our own solar system are largely unobserved by current research. Imaging extrasolar planets would open a large complementary region to radial velocity techniques, and a survey of this kind would provide valuable information about the distribution of planets in a 'typical' system. Imaging can also provide additional information about planets. Ground-based systems will require a specialized form of adaptive optics (AO) known as Extreme Adaptive Optics (ExAO) to achieve the high-contrast measurements

needed to image extrasolar planets.

Ground-based extrasolar planet imagers will look for young Jupiter-like planets that are still glowing with the heat of formation. This type of imaging will require contrasts of between 10^{-6} and 10^{-7} [4] making these instruments technically challenging. Stringent requirements for the number of actuators, precision of flattening and frame rate make deformable mirror (DM) technology a particular risk area.

The Gemini planet imager (GPI) is the extrasolar planet imager for the 8-m Gemini Telescope in Chile. It will require approximately 2000 actuators [48], for a clear aperture of 48 actuators across the pupil diameter. Even one non-working actuator cannot be tolerated in the aperture because it will scatter light into the discovery region. Contrast is ultimately limited by residual static wavefront errors [27], so GPI will require wavefront control with an accuracy of better than 1 nm rms within the low- to mid-spatial frequency range [48]. Space-based planet detection architectures have similar requirements. The first step to demonstrating this is to flatten the mirror itself — in the absence of aberrations — to the $<$ 1 nm level. An extrasolar planet imager will need to correct additional aberrations, but tests without abberation will identify performance limits for future more realistic tests as well as demonstrate the internal calibration requirements for the DM in an ExAO system. To adequately correct the changing atmosphere, the system must run at 2500 Hz. Stroke requirements are reduced by the combination of two DMs. A large-stroke DM will be used for large low-order wavefront correction (woofer) and a high-order device will be used for smaller mid- to high-order correction (tweeter). A traditional DM to meet the high actuator count requirement would be prohibitively large and expensive ($1000/channel).

Micro-electrical-mechanical-systems (MEMS) DMs, such as those manufactured

by Boston Micromachines Corporation (BMC) [50], are a promising solution to the DM problem. MEMS are fabricated of polysilicon and utilize an array of independently addressable electrostatic actuators. The top surface of the DM is a continuous gold-coated mirror which can be deformed by the actuators underneath. Performance testing and device characterization are ongoing at the Laboratory for Adaptive Optics (LAO) at the University of California, Santa Cruz. I have focused on the precision flattening requirement using a 1024 actuator device (the largest device currently available), and the results are presented here [60].

MEMS DMs have been used successfully in other AO systems. In a vision science system, Doble et. al. [67] compared the performance of a 144-actuator segmented MEMS device to a more traditional Xinetics DM. They found the MEMS DM to have comparable performance except when the MEMS DM was limited by stroke. A 1024-actuator segmented device was tested in a horizontal path application at frame rates in excess of 800 Hz with Strehl ratios > 0.5 at a wavelength of 1.5 μm by Baker et. al. [62]. Testbed work was also done with the 1024-actuator segmented device using Kolmogorov phase screens to introduce abberations [43]. A major limitation of this earlier segmented MEMS device was the number of inactive actuators.

A similar DM technology is the membrane electrostatic DM. Much development work and testing has gone into these devices [68], including some on-sky tests [69]. These devices typically have fewer actuators and much broader, modal influence functions than their MEMS counterparts. Membrane mirrors are more suited to curvature systems than high-contrast systems, which need to fit well-defined Fourier modes.

A modular, electroceramic DM developed by Xinetics and tested by the Jet Propulsion Laboratory (JPL) is another possibility for a large actuator count DM. There

are versions with 1024 and 4096 actuators. The 1024-actuator version has been tested extensively in the High Contrast Imaging Testbed at JPL [70], where it is kept in a temperature controlled vacuum chamber. JPL has achieved angstrom-level flatness within controllable spatial frequencies. Stability has been demonstrated to 0.01 Å [70]. The 500-nm stroke and mm-pitch make it a challenging device for use in ground-based astronomical systems. Smaller optics are advantageous in high-contrast systems because of improved optical quality when compared with larger optics.

Our ExAO testbed is uniquely suited to testing MEMS deformable mirrors in the high-contrast regime. We have already demonstrated an ability to operate at contrast levels of 10^{-7} to 10^{-8} [26]. The extremely accurate optical metrology of the phase shifting diffraction interferometer (PSDI) [51] allows absolute measurements of the MEMS DM. Using the PSDI as the wavefront sensor, we have flattened to < 1 nm rms over controllable spatial frequencies. The technical challenges in achieving this result can be broken into three categories: measuring the phase, controlling the MEMS, and maintaining the stability of the system. Errors in each of these tasks leads to errors in performance and these are summarized in an error budget. Preliminary work with the MEMS device, including some of the engineering challenges leading up to this result, have been presented in prior works [71, 63, 61]. A complete inventory of these difficulties, together with our mitigation techniques, is included here.

5.2 Description of ExAO testbed

The testbed has two modes of operation: imaging mode and interferometry mode. In imaging mode contrast can be measured directly, while in interferometer mode wavefront phase and amplitude are measured. (Wavefront mode is shown in Figure 5.1).

Contrast is directly related to wavefront error (WFE) and wavefront measurements are used to simulate image data. The comparison provides an internal consistency check for all measurements. The testbed was designed for operation in the high-contrast regime; thus, it has low WFE without active correction, an enclosure to reduce air turbulence and baffling to prevent scattered light. In initial experiments, without active correction, I demonstrated the total WFE of the testbed is 1.5 nm rms, with about 1 nm of that falling within the range of controllable spatial frequencies of our MEMS DMs [26]. In imaging mode, the reference pinhole is replaced with a CCD camera and only the probe beam is used. Further information about contrast measurements can be found in prior works [26, 63] and Chapter 4.

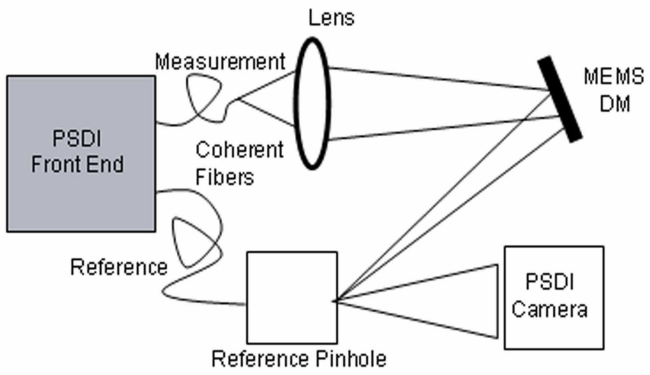

Figure 5.1: Simplified schematic of interferometry mode on the ExAO testbed. A physical aperture can be placed in front of the MEMS, but during closed-loop operation a software aperture is used.

In interferometry mode, the testbed becomes an extremely accurate optical metrology system. The PSDI)was developed at Lawrence Livermore National Laboratory for metrology of aspheric optics for use at ultra-violet wavelengths [51]. A probe (or measurement) wavefront is injected from the upper single-mode fiber in Figure 5.1. This passes through the system and is focused onto a pinhole embedded in a super-polished

flat mirror (the reference pinhole). Meanwhile, a coherent reference beam passes through the pinhole and interferes with the outgoing probe wavefront. The interference pattern is recorded by a CCD located in an arbitrary location along the optical axis. Using standard phase-shifting interferometer techniques, this produces a measurement of the fringe pattern at this location, which can then be converted to a wavefront. This wavefront is numerically propagated in two steps to the plane of interest using the ABCD matrix and a Huygens Integral transformation implemented with fast fourier transforms [51].

Wavefront measurements are used to control the MEMS during closed-loop operations. The spatial resolution at the MEMS plane is limited by truncation effects due to an aperture at the reference pinhole. The effective resolution in the MEMS plane is $\sim$ 141 μm or 41% of an actuator [60]. For closed-loop operation, programs in the interactive data language (IDL) are used to direct data acquisition (wavefront sensing with the PSDI), back propagation calculations and the commanding of the MEMS device through the MEMS driver. Before closed-loop operation, the alignment and voltage response of the system must be calibrated. Alignment is done by activating four known actuators on the MEMS and noting their position in a wavefront measurement. For voltage calibration the response of each actuator is measured and fit with a quadratic. These calibration measurements are used to convert wavefront measurements into actuator by actuator phase, and then to the corresponding voltages. Closed-loop operations can also be run with a spatially filtered Shack-Hartman wavefront sensor [72].

5.3 MEMS Deformable Mirrors

We have tested a total of ten 1024-actuator deformable MEMS mirrors fabricated by BMC [50]. While a future exoplanet imager will require more actuators, the

1024 device is the largest commercially available MEMS device. Characterization and performance testing of these devices have provided feedback to the design and specification for a larger device. We have characterized voltage response, actuator uniformity and device stability as these characteristics will affect closed-loop performance.

MEMS DM technology for ExAO applications is still under development, but over these ten devices, we have seen a dramatic improvement in unpowered flatness and yield, which will be crucial for the 4000-actuator device. The 1024-actuator mirrors have 4 inactive actuators by design (they are wired to ground). The actuators are spaced 340 μm apart with a continuous face sheet as the top surface. Due to residual manufacturing stress, the top surfaces of these devices have curvature. Early devices had $>$ 200 nm rms unpowered WFE, but more recent devices have had as little as 50 nm rms unpowered WFE.

In general, defective actuators occur during the manufacturing process rather than failing during operation. However, a combination of high humidity and high voltage can produce oxidation in individual actuators, which will eventually limit the performance of those actuators [59]. 'Snap-down' can also damage actuators. This occurs when an actuator has too much displacement and the electrical attraction compressing the actuator overcomes the mechanical force that allows the actuator to rebound. Two early devices were damaged by humidity at the LAO, but no damage due to snap-down has occurred.

The MEMS is controlled with 13-bit D/A conversion and amplification using a system developed by Red Nun Electronics Company. The smallest voltage step allowed with these electronics is 0.025 volts for the current configuration. This corresponds to a phase step of 0.18 nm near the center of the displacement range where response is

linear. The driver boards for many-channel systems like this are under development. It is critical and tedious to ensure that the mapping through the driver electronics is accurate. Minor damage to the boards can be difficult to detect and will negatively affect closed-loop performance.

One limitation of MEMS DM technology is the device's limited stroke, especially compared with macro-DM technology. In practice, we find that MEMS stroke depends on the position of neighboring actuators as expected for their relatively broad influence functions, which have approximately 26% crosstalk. In a typical AO system, the DM is operated at a bias to correct both positive and negative wavefront errors. The entire device is set at an intermediate voltage and actuators are moved by varying their voltage about the bias. We typically operate at a bias of 110 volts, that voltage being midway in our operational displacement. A maximum voltage limit of 160 volts is set to prevent snap-down both in software and on the voltage power supply. An imbalance between the electrostatic force of activating an actuator and the mechanical restoring force causes stroke at a bias to be reduced. In typical operations, these devices achieve about 1 μm of stroke with our operational parameters.

MEMS actuators have a non-linear response to voltage that varies on a individual device as well as between devices. We calibrate the voltage response of every actuator on a device. In this test, one actuator in each 4 by 4 array of actuators on the device is tested at varying voltages cyclically until all of the actuators are tested. There are 16 frames for each voltage level, with 64 actuators tested in each frame. In early tests the average voltage response of four actuators was used to calibrate the entire device. Performance was improved, particularly for irregular actuators, by calibrating individual responses.

Operating in closed loop mitigates the effect of small variations in voltage response between actuators. On the most recent device, the variation in maximum displacement at 160 volts is less than 5% (excluding the outer two rows and columns of actuators), which is well within our ability to flatten. Irregular actuators, however, are unable to achieve the desired position, regardless of number of iterations, producing an in-band fitting error that limits closed-loop performance. We have identified three categories of such actuators: no-response (or dead), low-response and coupled. Typically we refer to the yield of a MEMS device as percentage of working actuators. This number is particularly important in high-contrast applications as no-response actuators scatter light into the dark hole region. Actuator uniformity refers to the variability of all 'working' actuators including low-response and coupled actuators.

The oldest device has 96.9% normal actuators (33 irregular) while the most recent device has 99.5% normal actuators (5 irregular). Only 94.1% of actuators were normal (60 irregular) in tests of the segmented device published by Baker et. al. in 2004 [43, 62]. This dramatic improvement in actuator yield and uniformity has allowed improved performance and made MEMS DMs a feasible technology for high-contrast applications.

I have categorized irregular actuators as low-response or coupled. Low-response actuators can be actuators that only move with their neighbors or actuators with reduced voltage response. The February 2005 device in Fig. 3.8 has a low-response actuator that only moves with its neighbors, right in the center. After flattening, this actuator is offset from its neighbors by about 20 nm. In previous tests with this device [63], more irregular actuators were apparent due to errors in the driver electronics, but this electronics problem has since been corrected. Coupled actuators affect voltage calibration. For example,

in our best performing device (October 2005), there are two coupled actuators. When a coupled actuator's voltage response is tested individually, there is no displacement after the bias voltage because the other actuator in the pair is set to the bias during the test. If coupled actuators are tested simultaneously, the voltage response is normal. A coupled actuator will move to the lesser of the voltage applied to the pair.

Current closed-loop tests use the PSDI as the wavefront sensor, which limits frame rate due to the speed of data acquisition. As a result, excellent stability for both the system and the MEMS is required. The PSDI stability was measured to be 0.08 nm rms phase by replacing the MEMS with a flat mirror. The average long term stability of the MEMS was measured as 0.16 nm rms phase. On the shorter time scale the system is more stable with an average rms deviation of 0.13 nm rms phase for the MEMS and 0.07 nm rms phase for the flat mirror [60]. More information on system stability is located in Section 3.4.3.

5.4 Closed-loop performance

In these closed-loop tests, no additional aberrations were introduced into the system. The primary source of error is the MEMS DM itself. Although a ground-based extrasolar planet imager will have to correct the atmosphere, the more basic test here identifies the performance limitations of future more realistic tests. A planet imager will have a stringent internal calibration requirement of <1 nm (in mid-spatial frequencies). These experiments demonstrate that we can meet this requirement. The metric I use for closed-loop performance is WFE within the range of spatial frequencies which the DM can correct. Higher spatial frequencies will scatter to larger angles [27]. Using a numerical lowpass filter to avoid aliasing will create a dark hole region over controllable

spatial frequencies in the far-field image (or the power spectrum of the wavefront) [47, 29] (see Fig. 6.2). There are some higher order effects that cause higher order aberrations to fold into the dark hole, but these are small in a case with no additional aberration, making in-band WFE a good metric for a high-contrast system.

The ExAO testbed was designed to minimize measurement and stability errors so that closed-loop operation would be primarily a test of MEMS performance. In

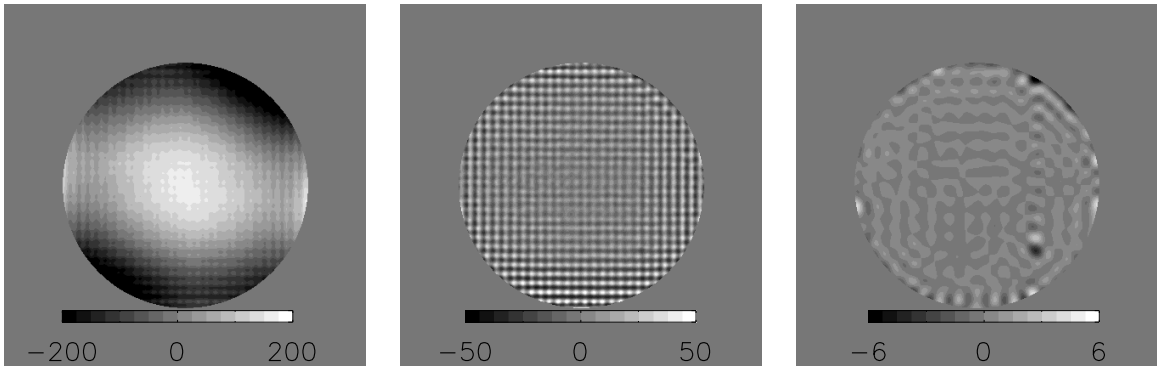

Figure 5.2: Wavefronts taken before and after a closed-loop test with a 9.2 mm aperture [60]. The initial wavefront has an rms wavefront error of 148 nm, while the flattened wavefront has 12.8 nm total rms wavefront error, which is mostly errors on the scale on an individual actuator. Inside the controlled range of spatial frequencies, the rms wavefront error is 0.54 nm. This is seen more clearly in the lowpass filtered image (far right).

previous closed-loop tests a 10-mm circular aperture was placed slightly in front of the MEMS device during flattening. In the most recent tests the physical aperture was replaced with a software aperture of the same size (9.2 mm in the MEMS plane) to reduce diffraction from the edge of the physical mask. A ring two actuators wide around the outside of the aperture is slaved to the final ring of actuators inside the aperture using a nearest neighbor average. The reason for this is that a discontinuity between controlled and uncontrolled actuators can produce a ringing 'edge' effect during closed-loop operation. Typically the closed loop is run for between 16-25 iterations with most of the correction taking place within the first five iterations. The test shown in Fig. 5.2

was run for 25 iterations with the best flattening occurring at iteration 20. Tip/tilt is not actively controlled. After a device is partially flattened, tip/tilt is removed optically. After that, flattening is done with tip/tilt removed numerically. Before running closed loop, the wavefront had 148.1 nm total rms WFE, and after flattening, the wavefront had 12.8 nm total rms WFE and only 0.54 nm rms WFE inside the controlled range of spatial frequencies. This level of performance of the system is quite repeatable. Out-of-band error is dominated by print through; however, this particular device has similar amounts of print through and almost twice as much out-of-band WFE as the February 2004 device. Possibly, the additional error is caused by the window. The wavefront improvement is noticeable in Fig. 5.2. The large structure of the errors in the initial wavefront have been corrected in the final wavefront (middle image), revealing smaller structures on the scale of an individual actuator. These small-structure errors fall outside of the region of controllable errors. By filtering out the high-spatial-frequency errors, the limitations to closed-loop performance can be better investigated (far right image). The light and dark actuators slightly to the right and below center are the coupled actuators previously discussed. They are about 3 nm above and below their neighbors. The effective aperture has a 9.2-mm diameter with approximately 27 actuators across yielding a highest controllable spatial frequency of about 13.5 cycles per aperture and a corresponding control radius in the point spread function of 13.5 λ/D. The cutoff frequency is apparent in the power spectrum (See Fig. 5.3) at the edge of the dark hole region. The 27 actuators correspond to an active aperture covering 84% of the MEMS device. I limit the aperture size to allow for at least 2 rows of slaved actuators around the active aperture to prevent an edge discontinuity, which introduces error, and to avoid the outermost row/column of the device, which is not fully covered by the face sheet and

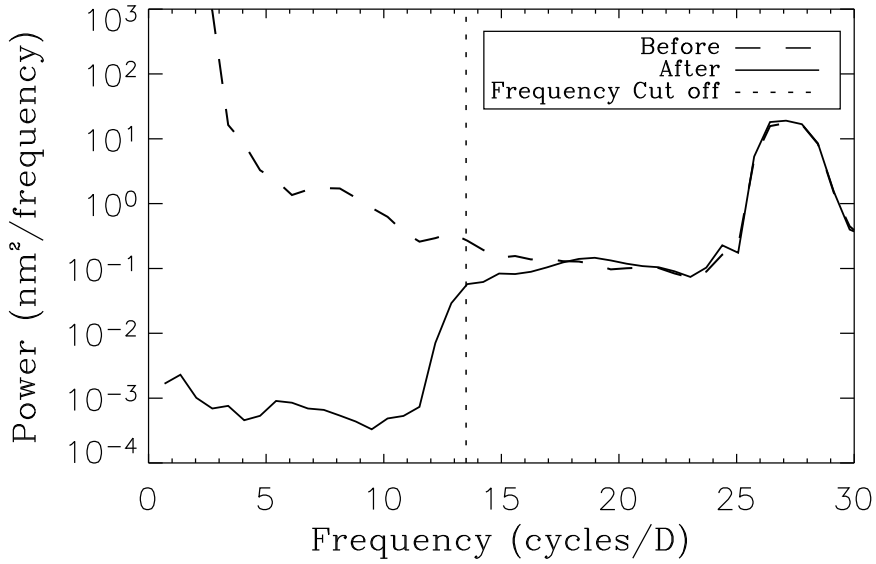

Figure 5.3: Power spectrum generated from wavefronts taken before and after flattening.The 27 actuators across the aperture yield a highest controllable spatial frequency of 13.5 cycles per aperture. The bump at 27 cycles per aperture corresponds to physical structures on the MEMS at the scale of the individual actuator spacing. As indicated in Section 5.5 wavefront measurement error is about 0.2 nm rms. If this error were evenly distributed over measured spatial frequencies error in the power spectrum would be $\sim 5 \times 10^{-6}$ and small compared to other stable error sources.

typically has less stroke. Aliasing is prevented with a numerical spatial filtering of the PSDI measurement. A bump in the power spectrum at 27 cycles per aperture indicates the error introduced by print-through of physical structures on the MEMS device. The primary effect in the far-field image of this error will be to produce repeating images of the point spread function (PSF) starting at $27\lambda/D$. In high-contrast imaging, where the region of interest (ROI) is inside the region of controllable spatial frequencies, MEMS print through is not a significant error source (see Fig. 6.2). The power spectrum was generated with a Blackman window to reduce ringing, and has a slightly reduced total WFE under the curve as a result.

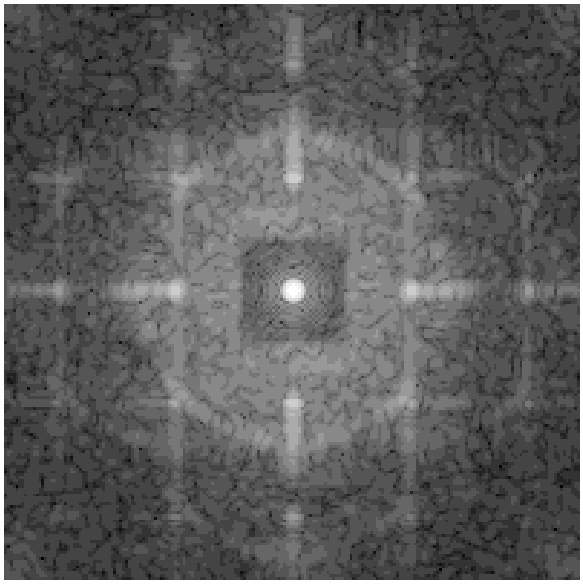

Figure 5.4: Far-field image simulated from the wavefront measurement shown in Fig.5.2. Diffraction has been suppressed with a symmetric Blackman apodization for illustrating the effect of high spatial frequency errors like print-through on the image.

5.5 Limitations to improved performance

Errors in correcting the wavefront can stem from imperfect wavefront measurements, instabilities in the system and the inability of the DM to fit the desired shape. I summarize these errors in an error budget (see Table 5.1). I have disregarded errors outside of the controllable spatial frequencies of the MEMS device. Fortunately, those errors will primarily scatter light outside of the ROI in corresponding far-field measurements.

I refer to the largest error source as an edge effect. It is measured by comparing the rms WFE over the full aperture and over a 75% aperture. In previous results, this error source was > 1 nm due to diffraction from the physical aperture and the distance between the aperture and the MEMS device. The physical aperture has been replaced with a software aperture, and the edge effect has been reduced to 0.42 nm. Even with this reduction, edge effects remain the largest error source. While diffraction and scattered light from the physical aperture have been removed, other sources remain and introduce

error into the PSDI measurements. It is particularly difficult to perfectly baffle light from the uncontrolled edges and wires of the MEMS device. A device window contributes to imperfect baffling. A more advanced optical layout with a well-defined pupil or another type of WFS could reduce this error.

The effect of irregular actuators on closed-loop performance is clear from the lowpass filtered image (far right of Fig. 5.2). Devices with more irregular actuators did not flatten as well as this device. The effect of the coupled actuators on flattening was estimated by comparing the rms WFE over 75% of the aperture to the error over the same aperture with the area around the irregular actuators removed. This does not account for any errors caused by the irregular actuators outside of their immediate vicinity. This technique for estimating error does not work well for no-response actuators or many irregular actuators within the aperture.

The remaining errors: voltage, stability and measurement are all system dependent. The voltage step size is determined by the number of bits in the electronics split over the voltage range of the electronics, currently 0 to 200 volts. This voltage step size is converted to phase using a typical voltage response in the vicinity of the bias voltage. The response over the small region required to correct most of the device is quite linear, but if more stroke on the device were to be required, this error could become larger. Voltage step size could be reduced with higher-resolution drivers, or with a change in the voltage range. The stability of the device was discussed previously. Measurement error is inherent to the PSDI system and is calculated by comparing two measurements taken consecutively. Alignment errors of the input fiber of the PSDI measurement leg increase measurement error.

The calculated WFE agrees well with the measured WFE indicating that these

Error Source	nm rms
Edge Effects	0.42
Irregular Actuators	0.22
Voltage Step Size	0.18
Stability	0.12
Measurement Error	0.20
Total	0.56

Table 5.1: Error budget for best flattening result. The experimental residual WFE is 0.54 nm rms within controllable spatial frequencies, which corresponds well to the error budget.

are the limiting errors for improved performance.

5.6 Conclusion

Our testing has demonstrated that MEMS DMs can be controlled at the level of precision needed for ExAO systems. I have flattened a MEMS DM to 0.54 nm rms over controllable spatial frequencies and identified the individual contributors to WFE in an error budget. The largest contribution is from edge effects caused by scattered light, interpreted as wavefront error by the PSDI. I have characterized the yield and actuator uniformity, which contribute to better calibration and provide feedback for device improvements. The most recent device has 99.5% normal actuators, which is a dramatic improvement over the early segmented device with 94.1% normal actuators [43]. In particular, the most recent device has no dead actuators within an aperture 27 actuators across, which greatly improves the performance. Overall, the level of closed-loop performance, without additional improvements, meets the precision and accuracy requirements for a high-contrast, giant-planet imager and demonstrates the feasibility of MEMS technology for such an instrument.

Chapter 6

Demonstrating 2×10^{-7} Contrast with a MEMS Deformable Mirror

6.1 Introduction

Imaging extrasolar planets is a technically challenging, but crucial step, in the study of planet formation and planetary science. Imaging young, Jupiter-like planets still glowing with the heat of formation will require contrast of between 10^{-6} and 10^{-7}. High-contrast imaging requires suppressing diffraction and controlling wavefront errors [27]. In practice, amplitude errors and scattered light make high-contrast imaging even more challenging.

Laboratory tests investigating the experimental limits to contrast are ongoing at several institutions. These experiments generally fall into three categories: contrast measurements without active wavefront control, tests of wavefront control accuracy, and contrast measurements with active wavefront control. Tests without active wavefront control are primarily investigating techniques for diffraction suppression. Deformable

mirrors (DMs) for a high-contrast system will be high order, and thus, wavefront control experiments generally focus on testing novel DM technology. While the specifications for active control are set in units of wavefront error (WFE), the metric that ultimately matters is contrast, making experimental measurements critical.

Tests without active control generally focus on suppressing diffraction. However, even the small amount of WFE in a carefully designed optical system will limit performance. At the Laboratory for Adaptive Optics (LAO), I have demonstrated that better than 10^{-7} contrast is achievable in a laboratory setting with low WFE (1.5 nm rms), but that WFE is the primary limitation to improved contrast [26] (see Chapter 4). Kasdin et. al. [64] have focused on pupil design and manufacturing limitations. They have identified numerous shaped pupil designs and demonstrated between 10^{-6} and 10^{-7} contrast at radii greater than 6 λ/D. Other experimental results have been obtained by Charborty et. al. [65] where they used a multi-opening gaussian pupil and achieved contrast of 4×10^{-7} at 4.5 λ/D. Contrast in a diffraction-suppressed regime scales with wavelength squared [27]. Therefore, Charborty et. al.'s results would be closer to 10^{-6} contrast at wavelengths comparable to Kasdin et. al.

High-contrast instrumentation requires precision wavefront control with many degrees of freedom, necessitating new DM technology. At the LAO, we have been testing the performance of 1024-actuator micro-electrical-mechanical-systems (MEMS) DMs made by Boston Micromachines Corporation (BMC) [50]. I have demonstrated flattening of $<$ 1 nm rms within controllable spatial frequencies [60] (see Chapter 5). The High Order Testbed (HOT) operated by the European Southern Observatory will also be testing the BMC DM but is only in its preliminary stages [73]. A modular electroceramic DM developed by Xinetics and tested by the Jet Propulsion Laboratory (JPL)

is another possibility for a large-actuator-count DM. There are versions with 1024 and 4096 actuators. The 1024-actuator version has been tested extensively in the High Contrast Imaging Testbed (HCIT) at JPL [70], where it is kept in a temperature controlled vacuum chamber. JPL has achieved angstrom level flatness within controllable spatial frequencies.

Precision phase control is critical for high-contrast imaging with a DM, but experimental measurements reveal that it is not sufficient. Extensive contrast measurements, including correction of amplitude errors, have been made at HCIT. The optical design of HCIT is more complicated than the Extreme adaptive optics (ExAO) testbed and includes a full Lyot coronagraph. The additional optics make end-to-end WFE on the order of 10 nm rms [74] for HCIT, while the ExAO testbed has approximately 1.5 nm rms WFE [26]. HCIT finds contrast to be limited by amplitude errors to 10^{-6} with phase only correction [74]. To combat amplitude errors, HCIT uses a speckle nulling algorithm to correct phase and amplitude errors affecting a half dark hole region [75]. They have demonstrated 2×10^{-9} contrast with speckle nulling and a Lyot coronagraph [75]. Speckle nulling requires many iterations, which make it quite slow and limit its usefulness for stable, space-based applications [76]. Speckle nulling is much too slow for ground based correction. More recent tests at HCIT, in collaboration with Princeton, have achieved contrast of 10^{-8} with a shaped pupil coronagraph [76]. These tests were limited by 'quilting'— errors in the wavefront on the order of an individual actuator. In a well-sampled wavefront measurement, these manifest as a grid pattern. In far-field measurements, the grid manifests as a repeating pattern at spatial frequencies corresponding to the actuator spacing. The additional PSF features can scatter light into the dark region of the primary point spread function (PSF). The effect of actuator ripple is

also seen in MEMS DMs but is not a limiting factor in the 10^{-7} contrast regime.

In this chapter, I present far-field measurements with a flattened MEMS device. This experiment builds on earlier work that focused on diffraction suppression [26] and wavefront control [60]. To facilitate an investigation of contrast limitations inherent to the MEMS device (such as amplitude errors), no phase errors were added to the system. The goal of this work was to demonstrate contrast of 10^{-7} with a MEMS device, similar to early work with a flat mirror [26]. I demonstrate that MEMS far-field performance is limited by amplitude errors and scattered light. The effect of irregular actuators on MEMS flattening has been discussed [60]. In Section 6.3.3, I demonstrate the effect of irregular actuators on contrast measurements.

6.2 Experimental method

The ExAO testbed is uniquely suited to high-contrast experiments. Contrast can be measured directly in imaging mode. The testbed can also operate in interferometry or phase shifting diffraction interferometer (PSDI) mode. The interferometry mode is used for optical metrology and closed-loop operations. A 1024-actuator MEMS DM [50] was installed and closed-loop performance was characterized with the PSDI as the wavefront sensor (WFS) [60]. The precision wavefront correction of < 1 nm over controllable spatial frequencies should yield excellent contrast.

A description of interferometry mode and closed-loop operations can be found in Chapters 3 and 5. Closed-loop wavefront data presented in prior works [60, 61] were obtained with a windowed device. The data presented here were obtained without a window because the window was found to introduce ghost images, which reduced contrast by a small but not negligible amount of 1×10^{-7}. The MEMS device used can be

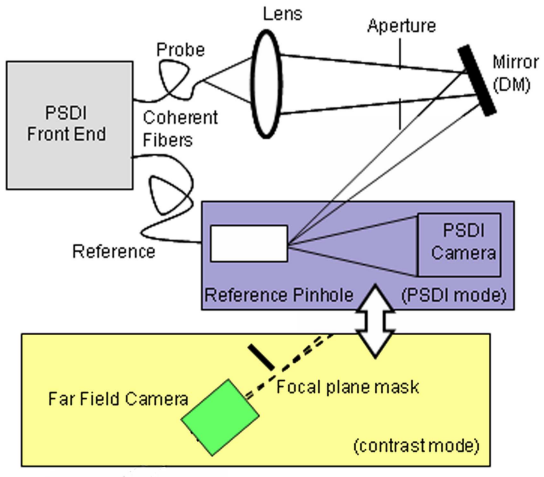

Figure 6.1: Simplified schematic of the ExAO testbed. The testbed has two modes of operation: imaging and phase shifting diffraction interferometry. The fold mirror in the system can be replaced with a deformable mirror for active wavefront control. The far-field camera is set 15 mm behind the focal plane, so a focal plane mask can be used to block light from the core of the point spread function and prevent CCD saturation.

consistently flattened to ~ 0.6 nm rms phase within controllable spatial frequencies.

A description of imaging mode can be found in Chapters 3 and 4. Far-field imaging with a MEMS device is more difficult than with a flat mirror because additional light is scattered in the focal plane. Extra care must be taken in aligning the focal plane mask (see Fig. 6.1). An experiment to quantify scattered light for the flat mirror case is presented in Section 6.3.2, and far-field simulations from measured wavefronts with the MEMS device place an upper limit on scattered light in far-field images with the MEMS.

6.3 Results and limitations

In this experiment, the MEMS was flattened to 0.54 nm rms within controllable spatial frequencies over a 10 mm aperture in the pupil plane (9.2 mm projected into the MEMS plane). This in-band WFE is slightly better than the in-band WFE of the flat mirror [26] and I expected slightly improved contrast over the narrow dark hole region. I reported 6.5×10^{-8} azimuthally averaged over 8 degrees from 10-25 λ/D with the flat

mirror (see Chapter 4). This larger region, however, is not available with the MEMS mirror. The region of interest (ROI) for the MEMS device is limited by the number of actuators across the aperture and increased scattered light at the focal plane mask. Over the more comparable region of 7-13.5 λ/D over 4 degrees, the flat mirror has a contrast of 1.5×10^{-7}. The MEMS DM has a contrast of 7.6×10^{-7} with a spatial intensity variation (i.e. the standard deviation in the ROI) of 7.6×10^{-7} from 6-13.5 λ/D over 4 degrees. This is worse than the flat mirror. The edges of the dark hole with the MEMS are contaminated by scattered light (inner edge) and high-order errors (outer edge), but even over the much smaller region of 8-11 λ/D, the MEMS contrast is 2.0×10^{-7} with a spatial intensity variation of 7.5×10^{-8}. The comparison is more obvious in radially

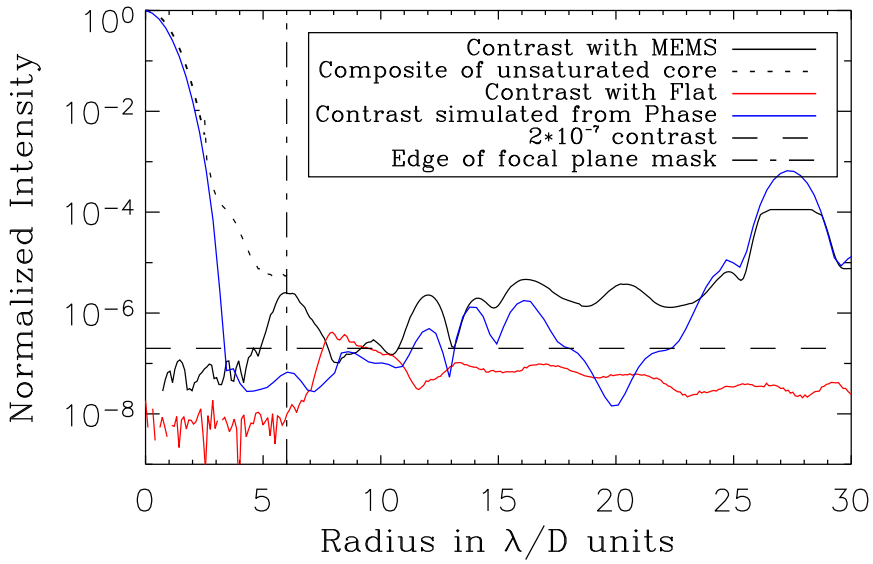

Figure 6.2: Radial average of far-field images taken with the flat mirror and with the MEMS. The dotted line is a composite of the core of the MEMS images. A simulated radial average far field was also generated from the measured phase. The error in contrast measurements can be estimated by intensity behind the focal plane mask, $\sim 5 \times 10^{-8}$. Measurement error is higher in the case of the MEMS because shorter integration times are added to generate an image with the exposure time needed for dynamic range.

averaged lineouts from the flat mirror far field and the MEMS DM far field (shown in

Fig. 6.2). Contrast is comparable between the flat and the MEMS over the dark hole region, but simulations predict the MEMS data should be better. Contrast, in the case of the flat mirror, is limited by phase errors [26], but a far-field simulation using the phase measured from the flattened MEMS DM indicates that phase is not the limiting factor for MEMS contrast (See Fig. 6.2 blue line). The average contrast from 8-11 λ/D over 4 degrees of the simulation with measured phase is 1.2×10^{-7}, as I would expect given the improved wavefront quality.

The HCIT at JPL has already identified amplitude errors as a limiting factor to contrast in their system [77], making amplitude errors a logical error source in our system as well. The PSDI measures both phase and amplitude; both can be used for more accurate simulations of far-field performance. In Fig. 6.3, a combination of phase and

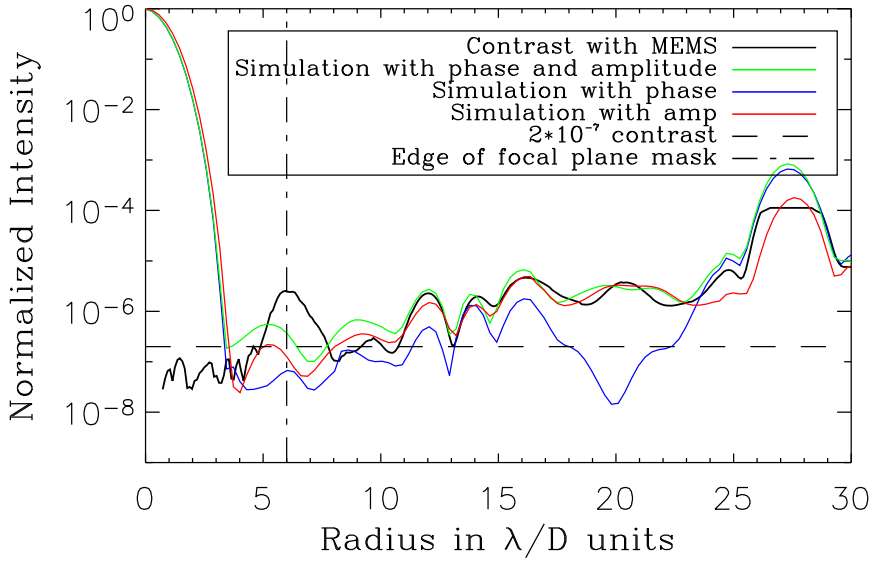

Figure 6.3: Radial average of experimental and simulated far-field images with the MEMS mirror. The black line is experimental MEMS data; the green line is a simulation using measured amplitude and phase; the blue line is a simulation with only phase, and the red line is a simulation with only amplitude. Contrast is limited with the MEMS device by amplitude errors. The amplitude errors are overestimated by the PSDI measurements. The most likely source of error in measuring amplitude is the reference pinhole, which is a non-common path item between the wavefront measurement and the far-field measurements.

amplitude have been used to simulate far-field performance. The blue line is a simulation using only phase as in Fig. 6.2. The red line is a simulation using the measured amplitude errors, but assuming no phase errors. The green line is a simulation using both measured phase and measured amplitude. Not unexpectedly, the best match to the experimental result (black line) is the simulation with both phase and amplitude. Amplitude errors are a limiting factor in contrast for the MEMS case. The simulations also indicate that amplitude errors are overestimated by the PSDI. The most likely source of this error is the reference pinhole of the PSDI. The pinhole is non-common path between wavefront measurements and far-field measurements. The 3 μm pinhole does not reflect light, and the substrate in which the pinhole is mounted will contribute to errors through surface roughness. The combination of phase and amplitude measurements can still be used to predict far-field performance but are not a substitute for experimental results. The simulations also indicate that light from the core is scattering off the focal plane mask reducing contrast in the experiment from 6-8 λ/D, and that region should not be included in average values of contrast, making the average contrast from 8-11 λ/D of 2.0×10^{-7} a more accurate representation of performance.

6.3.1 Amplitude errors

Amplitude errors can be measured directly in PSDI wavefront data and while errors may be slightly overestimated because of the reference pinhole, they remain a good metric for real errors. Amplitude errors can be caused by non-uniform pupil illumination, non-uniform reflectivity of the MEMS and out-of-plane phase errors. Spatial frequency information allows types of amplitude errors to be identified. An azimuthally averaged power spectrum comparing the amplitude with the MEMS DM and the flat mirror reveal systematic amplitude errors that are low frequency, while the MEMS primarily introduces

errors at the spatial frequency of individual actuators (See Fig. 6.4).

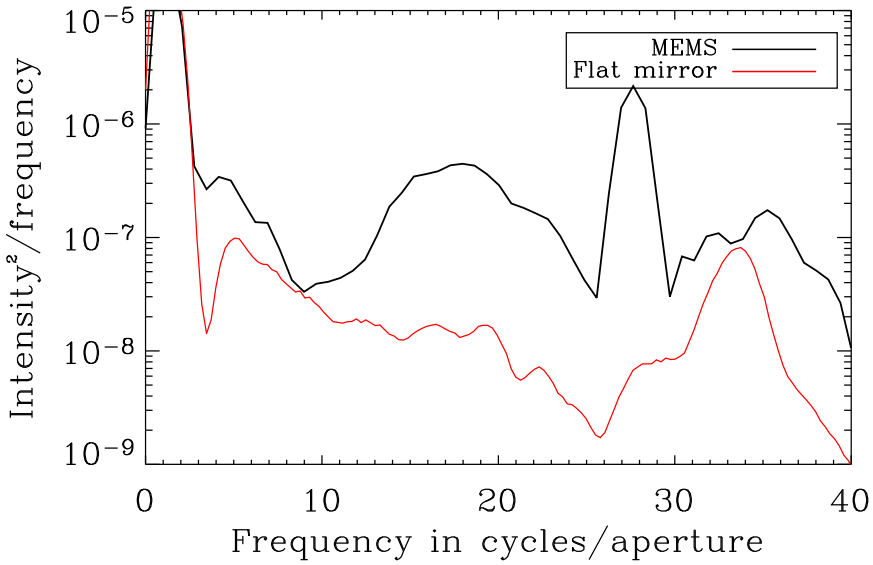

Figure 6.4: Radial average power spectrum of amplitude measurements with the flattened MEMS DM and the flat mirror. The amplitude measurement is normalized to one before the power spectrum is calculated. Most systematic amplitude errors are low order and likely caused by pupil illumination. The MEMS also introduces some amplitude error across all spatial frequencies. These errors are likely caused by variations in reflectivity. Amplitude errors are also introduced at the actuator spacing (corresponding to 27 cycles/aperture) by physical MEMS structures.

System amplitude errors are dominated by non-uniform pupil illumination (errors with a spatial frequency of < 5 cycles per aperture). For flat mirror measurements taken during the MEMS tests presented here and in the MEMS data, this error is about 2%. This level of error is consistent with measurements of illumination amplitude errors by JPL at HCIT [77]. Earlier flat measurements [26] had amplitude illumination errors of only 0.8% indicating that careful alignment of the input fiber and the pupil can reduce this error source in future MEMS measurements.

Amplitude measurements with the MEMS have an additional error of 2.6% at the spatial frequency of the actuator spacing, bringing the total error to 4%. It is likely that some real amplitude error is introduced by the MEMS ripple ('quilting'), but phase

errors also introduced at this spatial frequency can contribute to amplitude errors in the pupil because the pupil and the MEMS are not conjugate. PSDI measurements in the MEMS and pupil planes indicate that over the short distance between them there is little amplitude and phase mixing, but this could become a more serious concern if additional aberrations are introduced. Placing the MEMS at a pupil conjugate, or using a device with less ripple, could reduce this error source.

Amplitude errors in the MEMS data from 8-11 cycles per aperture (the ROI) are 0.2%.

6.3.2 Scattered light

A practical challenge in high-contrast imaging is scattered light. In the ExAO system, there is only one focal plane. The imaging camera is placed 15 mm behind the focal plane, and a mask allows the region where diffraction is suppressed by the prolate pupil to pass, while the core of the image, which can saturate the CCD, is blocked. A typical experimental image with the focal plane mask and the ROI labeled is shown in Fig. 6.5. The wedge shaped mask is made from shim stock covered with reflective mylar on the side facing the incoming beam. The inside corner of the wedge is covered with either a mirror or a straight piece of mylar. The mask is aligned to send light from the PSF core out of the system. Light still scatters off of the focal plane mask into the image. This effect is minimized by choosing a ROI which avoids the edges of the mask, thereby limiting the inner working distance (IWD). The effect of scattered light can be quantified by examining the difference between two far-field images with the focal plane mask slightly shifted in the second image. This test was done with the flat mirror. As expected, most of the scattered light is in the corner of the focal plane mask where the core is the brightest. I estimate the effect of scattered light to be about 15%. Moving

out to the 8 λ/D range where the ROI usually starts, the effect is reduced to 1%, which is significantly less than the measurement noise as defined by standard deviation over the region in an un-differenced image. Along the edges of the focal plane mask the effect is between 1 and 4%. The most important region to consider is along an 8 degree radial average from 8-15 λ/D, which is our typical ROI in these experiments. The variation in this region is 1% indicating that while scattered light in the focal plane is a significant problem in certain regions, it is not a problem over the typical ROI. Changes in the layout of the ExAO testbed will allow for improved focal plane masking, which could make these experiments easier and potentially improve the IWD. Contrast in the ROI will probably not improve with this change.

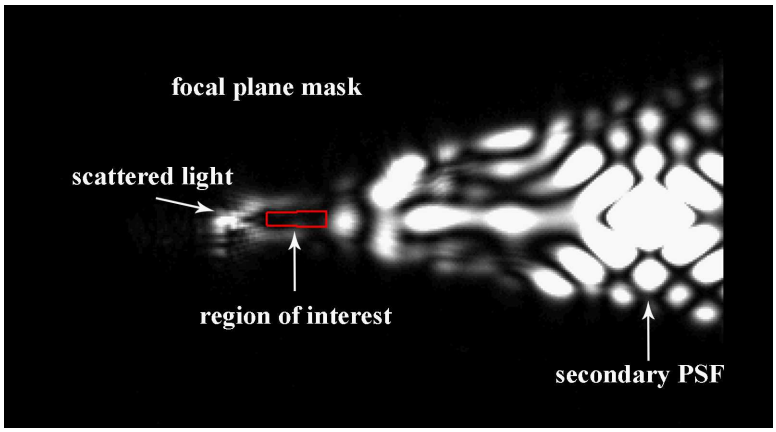

Figure 6.5: Experimental far-field image with focal plane mask. Light from the central core is mostly blocked by the focal plane mask but some light is scattered off the edges.'Quilting' errors on the surface of the MEMS produce a repeating pattern at spatial frequencies which correspond to the actuator spacing. The red box indicates the 8-11 λ/D ROI.

The less uniform surface of the MEMS scatters more light than the flat mirror, however most of it can still be baffled. In general, focal plane masking is the same as in the flat mirror case. However, increased light on the edges of the focal plane mask increases the intensity of scattered light and reduces the ROI from 8 degrees (typically used with the flat mirror) to 4 degrees. Additional light from the core is also scattered

in the MEMS case and contaminates contrast from 6-8 λ/D (See Fig. 6.2 and Fig. 6.5). In the flat mirror case, this region is limited by WFE. Comparison between MEMS data and flat mirror data (without the ripple) suggests that in the 10^{-7} contrast regime, scattered light from actuator ripple (or 'quilting') is not a limiting factor. A different shaped pupil with a wider dark region in the PSF or a more traditional coronagraph will make contrast measurements with the MEMS easier.

6.3.3 Irregular actuators

Irregular actuators limit performance because they do not have a typical voltage response (see section 3.4). I have identified three types of irregular actuators: no-response, low-response and coupled. Low-response actuators are often controlled only by moving neighboring actuators. We identify this type of irregular actuator as 'floating'. Irregular actuators introduce WFE during closed-loop operation [60], which in turn, limits contrast. No-response actuators are a particular problem because they scatter light over all spatial frequencies, including the frequencies in the dark hole region. To investigate the effect of irregular actuators on contrast, flattened wavefronts were modified to imitate extra irregular actuators. A floating actuator is simulated by setting an actuator to 20 nm below its ideal flattened position, while a simulated no-response actuator is set to 0 volts leaving the rest of the device in its original position. New wavefront measurements are taken and far-field images are simulated from the measured phase and amplitude. When diffraction is suppressed with a prolate shaped pupil, the position of the irregular actuator can vary the effect on contrast, but with a symmetric apodization this is not a problem. A floating actuator removed from its flattened position by 20 nm causes a reduction in contrast over the ROI of 5×10^{-7}. A no-response (or dead) actuator is much more serious, reducing contrast by over two orders of magnitude. Simulated

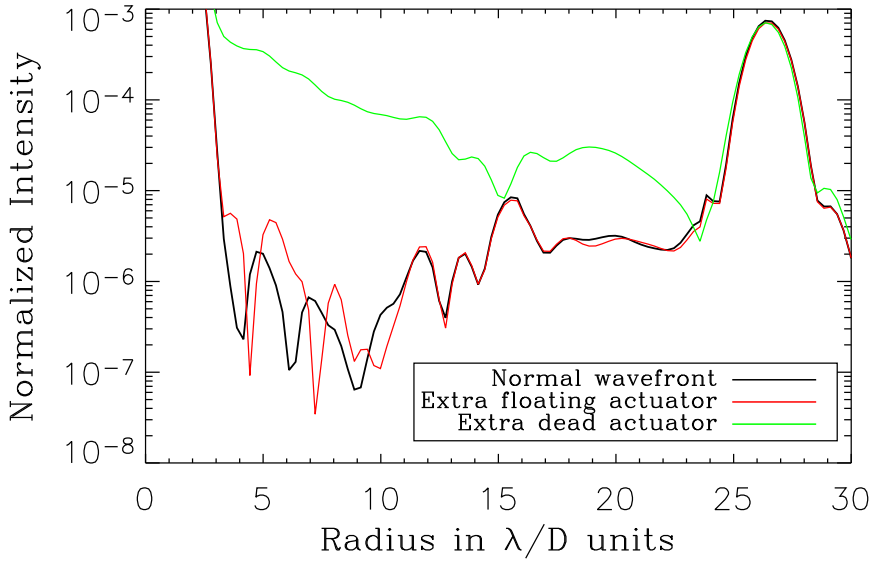

Figure 6.6: Radial average of simulated far-field images showing loss of contrast with additional irregular actuators. A typical flattened wavefront is modified to have either an extra floating actuator 20 nm below its flattened position or one normal actuator is set to 0 volts to simulate a no-response actuator. Then a far-field image is simulated from the wavefront.

far-field measurements are azimuthally averaged over 4 degrees for the case of a normal flattened wavefront, one additional floating actuator and one no-response actuator, and the results are shown in Fig. 6.6. The floating actuator produces error primarily in the region of controllable spatial frequencies, while the no-response actuator scatters light over a much broader range. The dramatic effect of the no-response actuator is obvious in the simulated far-field image of Fig. 6.7. Here, the top image was simulated with a normal wavefront, and the bottom image was simulated with an added no-response actuator. The no-response actuator clearly obscures the dark hole region with scattered light.

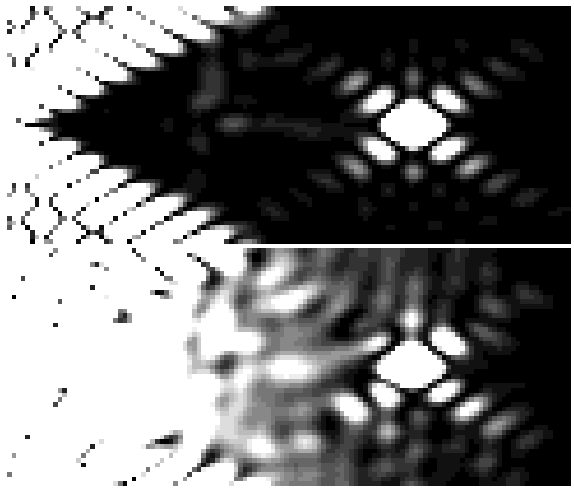

Figure 6.7: Top image is a far-field image simulated from a wavefront measurement with the prolate pupil in place. (The x-pattern is characteristic of a single opening prolate pupil.) Below, the far-field image was simulated with the same wavefront modified to have a dead actuator within the aperture. Scattered light from a single dead actuator dramatically reduces contrast. Both images are plotted on the same linear scale.

6.4 Conclusion

I have demonstrated 2.0×10^{-7} contrast over a small, well-defined region in the far-field generated with a flattened MEMS (phase only correction) using a prolate shaped pupil for diffraction suppression. I have previously demonstrated contrast limitations with a flat mirror [26] and precision flattening of a MEMS DM [60]. Flat mirror experiments focused on suppressing diffraction, while earlier MEMS experiments focused on reducing WFE. In this experiment my expertise in these two areas was critical to high-contrast performance but not sufficient. Comparison to previous contrast measurements with a flat mirror indicates MEMS performance is similar to flat mirror performance despite slightly improved WFE. Improved contrast requires a reduction of amplitude

errors through more careful optical design or active control. In addition, the ROI in MEMS measurements is limited by scattered light.

These results were taken with the MEMS flattened but without the introduction of model atmospheric phase aberrations. The simpler layout of this experiment allowed us to investigate the error sources inherent to the MEMS that limit contrast. Next steps include better focal plane masking, amplitude correction and the introduction of Kolmogorov phase screens. Additional wavefront errors will likely introduce unrealistic amplitude errors making MEMS far-field performance more difficult to quantify. These preliminary far-field experiments indicate that amplitude errors from phase screens must be well characterized to understand performance limitations.

Chapter 7

Correcting atmosphere-like aberrations

7.1 Introduction

Building an extrasolar planet imager is technically challenging, as it requires contrasts that are nearly two orders of magnitude better than current instrumentation. Experimental, proof-of-concept work is critical to the success of the instrument design and implementation. I have demonstrated that the Extreme Adaptive Optics (ExAO) testbed can operate in the necessary high-contrast regime for proof-of-concept tests and demonstrated the feasibility of the novel micro-electrical-mechanical-systems (MEMS) deformable mirror (DM) technology. These tests were performed with a simple optical layout that allowed fundamental exploration of contrast limits, but did not resemble a realistic instrument layout. The most obvious discrepancy in the initial tests is the lack of additional optical aberrations.

Micro-electrical-mechanical-systems DMs have been used in more realistic adap-

tive optic (AO) systems to correct atmospheric distortion as well as aberrations introduced by the human eye. In these cases, the MEMS DMs performed comparably to more traditional DM technology [78, 67], but not as well as the precision flattening that was demonstrated on the ExAO testbed. Several AO systems for vision science research are using 140-actuator MEMS DMs, but these systems are generally limited to 0.1 μm rms over all spatial frequencies [79, 67]. In a different application a 1024-actuator segmented MEMS device was tested in a horizontal path application, and it achieved Strehl ratios of > 0.5 at a wavelength of 1.5 μm. On the ExAO testbed, I have demonstrated wavefront correction of < 1 nm rms within controllable spatial frequencies (< 10 nm rms total wavefront error). This test was done without additional aberrations, which were included in the experiments mentioned above. Any practical AO system will have to correct more wavefront error than exists on the ExAO testbed, which makes it critical to understand how the error budget for flattening applies to the more realistic case.

Will known error sources increase when additional aberrations are introduced, or will new error sources limit residual wavefront error (WFE)? In this chapter, I present preliminary experiments with a Kolmogorov phase screen which introduces atmospheric aberrations to the ExAO system. I investigate the limits to wavefront control with this additional aberration and present simulated far-field results.

7.2 Experimental method

The layout of the ExAO testbed has been described thoroughly in previous chapters (see Chapters 3, 4 and 5). The layout of both modes of the testbed is shown in Fig. 7.1. For the tests described here, a Kolmogorov phase screen is placed approximately 200 mm in front of the MEMS device (see Fig. 7.2).

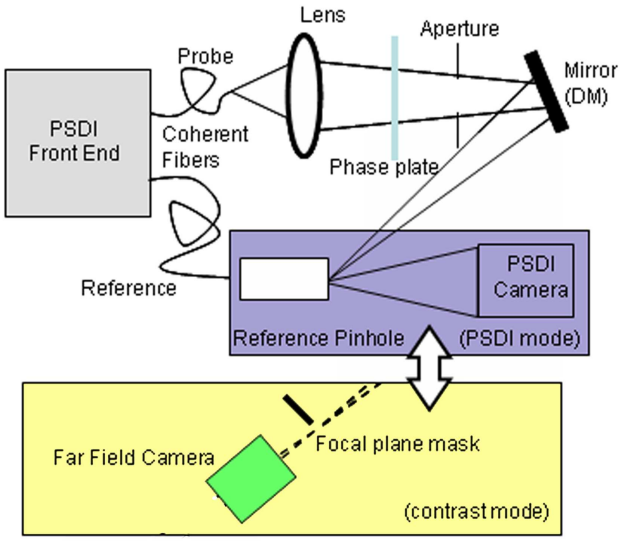

Figure 7.1: Simplified schematic of the ExAO testbed. The testbed has two modes of operation: imaging and phase shifting diffraction interferometry. The fold mirror in the system can be replaced with a DM for active wavefront control. A Kolmogorov-like phase plate is introduced before the aperture to provide additional aberrations for correction.

Closed-loop operations were described in Chapter 5. Operation with additional aberration functions in much the same way. The phase shifting diffraction interferometer (PSDI) is used as the wavefront sensor (WFS). The voltage response of each actuator (or the average of 4 actuators) is calculated without the phase plate. Alignment between the PSDI and the MEMS is calibrated with the plate in place, after a partial correction of WFE by the MEMS. Misalignment of the phase plate will introduce errors to the calibration, but re-calibrating after partial correction can eliminate these errors.

The system can also be operated in far-field imaging mode to directly measure contrast (see Chapters 3 and 4). Fig. 7.2 is an unfolded layout of imaging mode showing the position of the phase plate, the pupil and the MEMS. The beam is slowly converging thus minimizing the effects introduced because of the plate. The pupil and MEMS are not conjugate. Phase and amplitude mixing could be introduced by the separation, and that error still needs to be investigated.

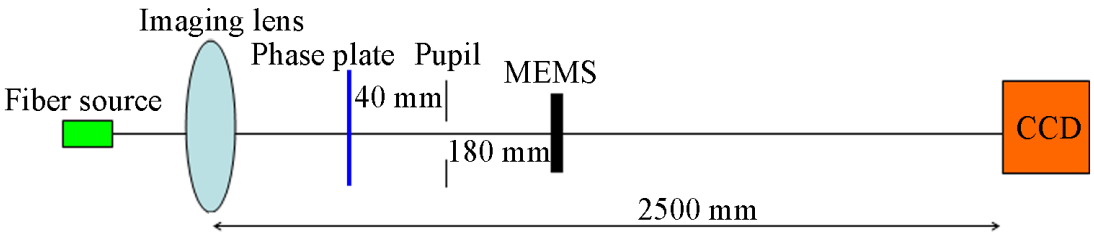

Figure 7.2: An unfolded layout of imaging mode showing the separation between the phase plate, the pupil and the MEMS.

Several types of phase plates have been specified and manufactured for the ExAO testbed. The plate used in this experiment is composed of two tooled Lexan plates sandwiching a near index matching resin. This plate is designed to produce WFE with Kolmogorov statistics with a wide range of spatial frequency content. The design was tested to ensure that the MEMS had the stroke to correct the WFE within controllable spatial frequencies. The measured phase and amplitude of the plate is shown in Fig. 7.3. The plate introduces approximately 87 nm rms total WFE. Unfortunately, it also introduces nearly 18% amplitude variation, which makes far-field imaging quite difficult (see Section 7.4).

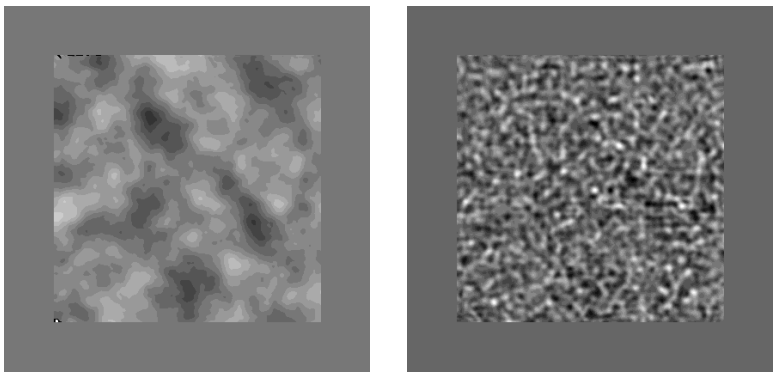

Figure 7.3: Measured phase (left) and amplitude (right) of the phase plate with MEMS errors subtracted. The plate introduces about 87 nm rms wavefront error and approximately 18% amplitude errors.

7.3 Closed-loop performance

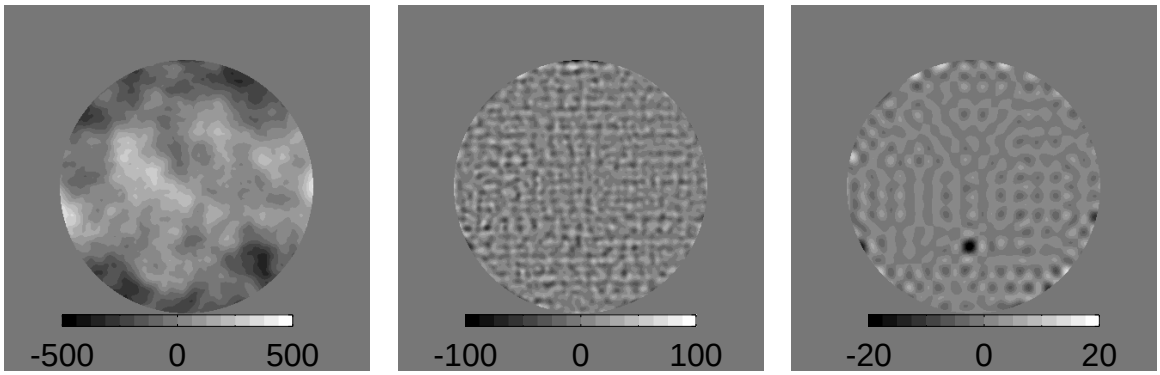

Figure 7.4: Left: Wavefront with Kolmogorov phase screen before closed loop is run with 119.6 nm rms WFE. Middle: Wavefront after closed loop is run; higher order errors from plate and MEMS dominate (13.3 nm rms). Right: Low pass filtered wavefront after closed loop. Wavefront appears to have similar error to closed loop without the phase plate, however magnitude of error is higher. The WFE over controllable spatial frequencies is 2.0 nm rms compared to the 0.5 nm rms of the MEMS alone.

The wavefronts from closed-loop operation with the phase plate are shown in Fig. 7.4. The large-structure errors in the uncorrected image (Left image Fig. 7.4) are dominated by the Kolmogorov phase plate. After correction, MEMS errors on the scale of an individual actuator are visible, but high order errors (errors with spatial frequencies outside of controllable spatial frequencies) are primarily introduced by the phase plate. When the corrected image is lowpass filtered to show only controllable spatial frequencies, the wavefront appears quite similar to corrected MEMS wavefronts without the phase plate and suggests that irregular actuators are a source of WFE.

Closed-loop performance is quantified by rms WFE. The in-band rms WFEs are calculated by first lowpass filtering the wavefront (right image of Fig. 7.4), and then calculating the standard deviation over the aperture. The WFEs for closed-loop performance with and without the phase plate are presented in Table 7.1. Despite a similar appearance, the corrected in-band WFE with the phase plate is four times that

Wavefront	total nm rms	in-band nm rms
MEMS uncorrected	94.7	93.0
MEMS corrected	5.4	0.5
Phase plate and MEMS uncorrected	119.6	116.3
Phase plate and MEMS corrected	13.3	2.0

Table 7.1: Summary of corrected and uncorrected WFE for closed-loop performance with and without the phase plate.

Error Source	nm rms
Edge Effects	1.0
Irregular Actuators	1.1
Voltage Step Size	0.18
Stability	0.13
Measurement Error	0.20
Out-of-band leakage	1.2
Total	1.9

Table 7.2: Error budget for flattening with phase plate. The experimental residual WFE is 2.0 nm rms within controllable spatial frequencies.

of the error without the plate.

As in the data for the MEMS alone, the individual contributors to WFE with the phase plate can be summarized in an error budget, and most of the sources remain the same. Edge errors and errors introduced by irregular actuators are significantly increased by the phase plate. With the MEMS alone, irregular actuators account for 0.22 nm rms WFE, whereas in the phase plate case, this error is over 1 nm and the second largest error source. It should be noted that the irregular actuator visible in the right-hand wavefront of Fig. 7.4 is not the same as the irregular actuator that dominates the wavefront of the MEMS flattened alone. It is possible to align the phase plate to reduce the effect of irregular actuators, although that does not produce a realistic measurement of AO system performance.

Stability and measurement error remain the same as in the MEMS alone case. The error due to the voltage step size also remains the same. This error is calculated by converting the smallest voltage step size of 0.025 volts to phase, using the average

voltage calibration near the bias voltage of 110 volts. The histogram of Fig. 7.5 indicates that, as in the MEMS-alone case, when correcting the phase plate, most of the actuators remain near the bias voltage. A voltage step size error of 0.18 nm rms is still accurate.

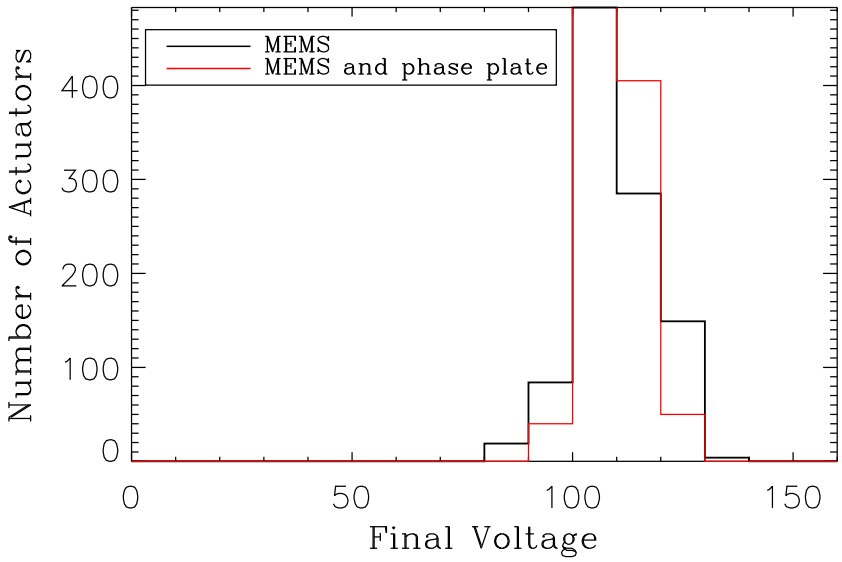

Figure 7.5: A histogram of final voltages when correcting the MEMS alone, and for correcting the phase plate. In either case, the majority of actuators remain close to the bias voltage of 110 volts.

The error sources for closed-loop operation without the phase plate only account for about 1.5 nm rms of the error with the phase plate indicating that a new error source must be considered when additional aberrations are introduced. Examination of the power spectrum of the final wavefront (see Fig. 7.6) reveals that a major source of error occurs at spatial frequencies just inside the region of controllable spatial frequencies. This error suggests that out-of-band errors are 'leaking' into controllable spatial frequencies, possibly by an incorrect estimation of in band-errors. During closed-loop operation, MEMS commands are calculated after numerically lowpass filtering PSDI wavefront data with a hard-edged square aperture to prevent aliasing. The same technique is used to calculate in-band rms WFE after tests. WFE can also be estimated by a summation

of the power spectrum over specific spatial frequencies. Calculations of this type are largely consistent with the rms errors calculated with the lowpass filter, but suggest that errors could be introduced by filtering, particularly in cases of large uncorrectable WFEs. Further investigation is needed to characterize and reduce out of band leakage errors, which would also eliminate uncertainties about rms error calculations. Disregarding the out of band leakage (effectively reducing the size of the dark hole region) the corrected wavefront has about 1 nm rms WFE.

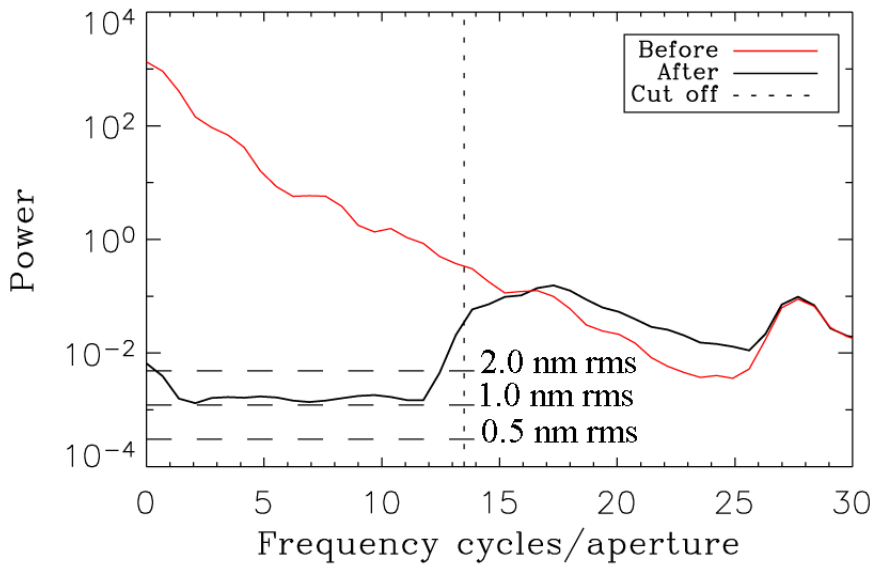

Figure 7.6: Power spectrum of before and after wavefronts with the phase plate. Before correction wavefront error is distributed across all spatial frequencies, but after correction a dark hole of approximately 1 nm rms has been achieved. The edge of the dark hole between 11 and 13.5 cycles/aperture is contaminated by higher order errors outside of controllable spatial frequencies.

7.4 Simulated far-field performance

Direct far-field measurements after wavefront correction of the phase plate proved difficult. The dark hole region is obscured by speckles unaccounted for in simulations from phase measurements. As in contrast measurements with the MEMS alone,

contrast measurements with the phase plate are limited by amplitude errors. While these errors are not large with the MEMS, the phase plates introduce amplitude errors on the order of 20%, thus significantly decreasing contrast. Because of the difficulty in directly measuring contrast, I have used simulations to investigate contrast limits with the phase plate. Previous comparisons of experimental far-field measurements to simulation indicate that simulations from both measured phase and measured amplitude are accurate indicators of experimental far-field performance (see Chapter 6). Figure 7.7 illustrates the effect of phase errors and amplitude errors, and the necessity of suppressing diffraction in high-contrast measurements. These images were simulated with a prolate shaped pupil. The image on the left is from measured phase before correction. The characteristic x-pattern of the prolate pupil is barely visible, and there is very little concentration of light in the core of the point spread function (PSF). The middle image is a simulation after correction with the phase measurement only. The red box indicates the edge of controllable spatial frequencies, the dark hole region. In the simulation with phase only, wavefront correction is clear throughout the red box, but high contrast is achieved only over the triangular regions where diffraction is suppressed by the prolate shaped pupil. The right image is a simulation using measured amplitude and phase. Diffraction is still suppressed, but the corrected dark hole region is much less obvious. This is the simulation which most accurately represents what experimental far-field data would look like. The scale of all three images is the same. Figure 7.8 provides a more quantitative illustration of far-field performance. The three simulations from Fig. 7.7 are azimuthally averaged over 4 degrees, and plotted versus radius. In the blue line, the far-field image before wavefront correction shows no dark hole region and a contrast of approximately 10^{-3}. After wavefront correction, a simulation from measured phase ex-

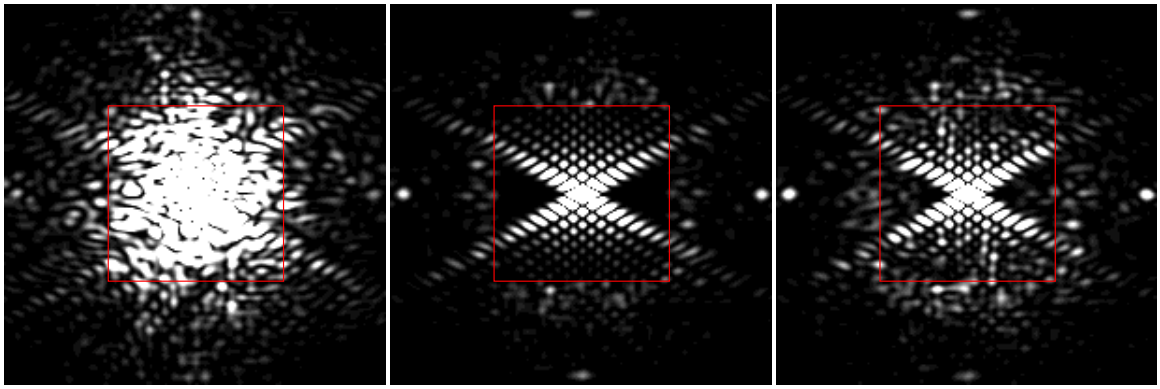

Figure 7.7: Simulated far-field images using a prolate shaped pupil for diffraction suppression. Left: Simulation from uncorrected wavefront phase. Middle: Simulation from corrected wavefront phase. Right: Simulation from corrected wavefront amplitude and phase. The red box indicates the 'dark hole' region over controllable spatial frequencies.

hibits a defined dark hole region. The outer edge of the dark hole is contaminated by out of band leakage as discussed in Section 7.3, but contrast of 10^{-6} is still achieved. When amplitude errors are included, the dark hole is more obscured and contrast is reduced to at least 10^{-5}. While performance is slightly better at small angles in the simulation, this cannot be measured using the current experimental set up due to scattered light near the core.

7.5 Conclusions

The inclusion of additional wavefront aberrations is critical to understanding realistic AO system performance. Introducing Kolmogorov phase screens increases the residual WFE introduced by irregular MEMS actuators, but the largest error source is a new measurement error in the PSDI which is produced by large out of band errors. WFE is reduced from 119 nm rms to 2 nm rms over controllable spatial frequencies. The residual error is reduced to 1 nm if out-of-band leakage is disregarded— effectively reducing the size of the dark hole region. Unfortunately, the phase plates also introduce significant amplitude errors, which simulations indicate will limit contrast measurements

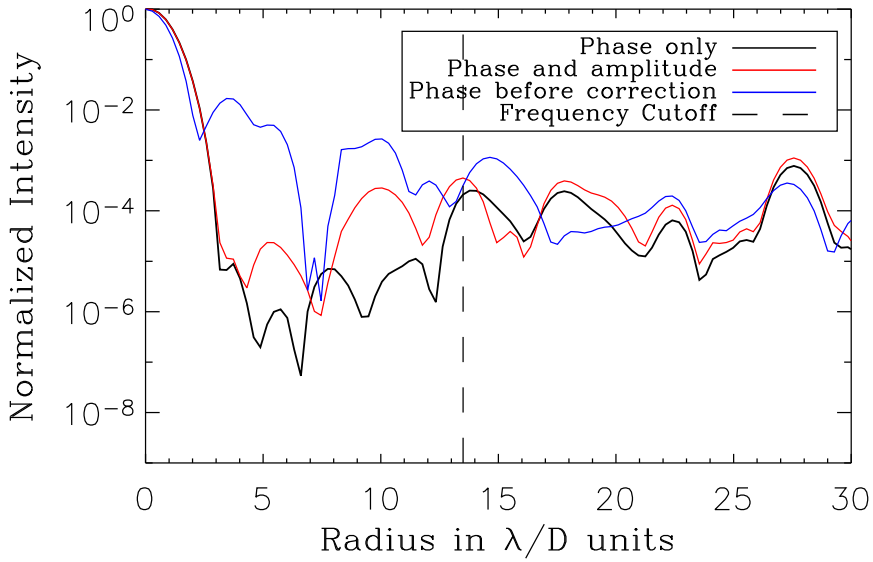

Figure 7.8: Radial average of far-field images simulated with measured phase before and after wavefront correction and measured phase and amplitude after correction.

to no better than 10^{-5}. The amplitude errors of the phase plates are unphysical and do not indicate a real system limitation. However, amplitude errors must be reduced to allow realistic future tests of instrument components.

Bibliography

1. G. W. Marcy. California & carnegie planet search. http://exoplanets.org, 2006.

2. A. Sozzetti. Astrometric methods and instrumentation to identify and characterize extrasolar planets: A review. *Publications Of The Astronomical Society Of The Pacific*, 117:1021–1048, 2005.

3. Beichman C.A. A road map for the exploration of neighboring planetary systems (ExNPS). Technical report, Jet Propulsion Laboratory, 1996. Written by the ExNPS Team, ed. C.A. Beichman.

4. A. Burrows, M. Marley, W. B. Hubbard, J. I. Lunine, T. Guillot, D. Saumon, R. Freedman, D. Sudarsky, and C. Sharp. A nongray theory of extrasolar giant planets and brown dwarfs. *Astrophysical Journal*, 491:856–875, 1997.

5. G. Marcy and R. P. Butler. Detection of extrasolar giant planets. *Annual Reviews of Astronomy and Astrophysics*, 36:57–98, 1998.

6. Michael Zeilik and Stephen A. Gregory. *Introductory Astronomy and Astrophysics*. Saunders College Publishing, Fort Worth, fourth edition, 1998.

7. G. Basri, W.J. Borucki, and D. Koch. The kepler mission: A wide-field transit search for terrestrial planets. *New Astronomy Reviews*, 49:478–485, 2005.

8. N. J. Rattenbury. Planetary microlensing: From prediction to discovery. *Modern Physics Letters*, 21:919–933, 2006.

9. K. L. Luhman and Ray Jayawardhana. An adaptive optics search for companions to stars with planets. *Astrophysical Journal*, 566:1132–1146.

10. Beth A. Biller, Laird Close, Rainer Lenzen, Wolfgang Brandner, Donald W. McCarthy, Eric Nielsen, and Markus Hartung. Suppressing speckle noise for simultaneous differential extrasolar planet imaging (SDI) at the VLT and MMT. Domenico Bonaccini Calia, Brent L. Ellerbroek, and Roberto Ragazzoni, editors, *Advancements in Adaptive Optics*, Proc. SPIE **5490**, p. 389–397, 2004.

11. C. Marois, R. Doyon, D. Nadeau, R. Racine, M. Riopel, P. Vallee, and D. Lafreniere. TRIDENT: an infrared differential imaging camera optimized for the detection of methanated substellar companions. *Publications Of The Astronomical Society Of The Pacific*, 117:745–756, 2005.

12. Bruce A. Macintosh, E.E. Becklin, Denise Kaisler, Quinn Konopacky, and B. Zuckerman. Deep Keck adaptive optics searches for extrasolar planets in the dust of ϵ Eridani and Vega. *Astrophysical Journal*, 594:538–544, 2003.

13. E. Masciadri, R. Mundt, Th. Henning, C. Alvarez, and D. Barrado y Navascues. A search for hot massive extrasolar planets around nearby young stars with the adaptive optics syste NACO. *Astrophysical Journal*, 625:1004–18, 2005.

14. John E. Krist. High contrast imaging with the hubble space telescope: Performance and lessons learned. John C. Mather, editor, *Optical, Infrared and Millimeter Space Telescopes*, Proc. SPIE **5487**, p. 1284–1295, 2004.

15. J. R. P. Angel. Ground-based imaging of extrasolar planets using adaptive optics. *Nature*, 368:203–207, 1994.

16. Bruce A. Macintosh, Brian Bauman, Julia Wilhelmsen Evans, James R. Graham, Christopher Lockwood, Lisa Poyneer, Daren Dillon, Don T. Gavel, Joseph J. Green, James P. Lloyd, Russell B. Makidon, Scot Olivier, Dave Palmer, Marshall D. Perrin, Scott Severson, Andrew I. Sheinis, Anand Sivaramakrishnan, Gary Sommargren, Remi Soummer, Mitchell Troy, J. Kent Wallace, and Edward Wishnow. eXtreme Adaptive Optics Planet Imager: overview and status. Domenico Bonaccini Calia, Brent L. Ellerbroek, and Roberto Ragazzoni, editors, *Advancements in Adaptive Optics*, Proc. SPIE **5490**, p. 359–369, 2004.

17. Bruce A. Macintosh, Scot S. Olivier, Brian J. Bauman, James M. Brase, Emily Carr, Carmen J. Carrano, Donald T. Gavel, Claire E. Max, and Jennifer Patience. Practical high-order adaptive optics systems for extrasolar planet searches. Robert K. Tyson, Domenico Bonaccini, and Michael C. Roggemann, editors, *Adaptive Optics Systems and Technology II*, Proc. SPIE **4494**, p. 60–68, 2002.

18. James E. Larkin, Andreas Quirrenbach, Alfred Krabbe, Ted Aliado, Matthew Barczys, George Brims, John Canfield, Thomas M. Gasaway, David LaFreniere, Nick Magnone, Gunnar Skulason, Michael Spencer, David Sprayberry, and Jason Weiss. Osiris: infrared integral field spectrograph for the keck adaptive optics system. Masanori Iye and Alan F. M. Moorwood, editors, *Instrument Design and Performance for Optical/Infrared Ground-based Telescopes*, Proc. SPIE **4841**, p. 1600–1610, 2003.

19. H. M. Schmid. SPHERE VLT planet finder. http://www.astro.phys.ethz.ch/research/planets/sphere, 2006.

20. R. Gratton, H.M. Schmid, W. Brandner, S. Hippler, R. Neuhäuser, A. Quirrenbach, S. Desidera, M. Turratto, and D.M. Stam. The science case of the CHEOPS planet finder for VLT. Alan F.M. Moorwood and Masanori lye, editors, *Ground-based Instrumentation for Astronomy*, Proc. SPIE **5492**, p. 1010–1021, 2004.

21. D. Mouillet, T. Fusco, AM Lagrange, and JL Beuzit. 'Planet Finder' On The VLT: Context, Goals and Critical Specifications for Adaptive Optics. *EAS Publications Series*, 8:193–199, 2003.

22. T. Fusco, C. Petit, G. Rousset, J.-F. Sauvage, K. Dohlen, D. Mouillet, J. Charton, P. Baudoz, M. Kasper, E. Fedrigo, P. Rabou, P. Feautrier, M. Downing, P. Gigan,

J.-M. Conan, J.-L. Beuzit, N. Hubin, F. Wildi, and P. Puget. Design of the extreme ao system for SPHERE, the planet finder instrument of the VLT. Brent L. Ellerbroek and Domenico Bonaccini Calia, editors, *Advances in Adaptive Optics II*, Proc. SPIE **6272**, p. 62720K, 2006.

23. A. Karlsson, L. d'Arcio, R. den Hartog, and M. Gridlunc. Darwin a mission overview. John C. Mather, Howard A. MacEwen, and Mattheus W. M. de Graauw, editors, *Space Telescopes and Instrumentation I: Optical, Infrared and Millimeter*, Proc. SPIE **6262**, p. 62651O, 2006.

24. C. Henry. Terrestrial planet finder interferometer 2005. Daniel R. Coulter, editor, *Techniques and Instrumentation for Detection of Exoplanets II*, Proc. SPIE **5905**, p. 1–7, 2005.

25. Randall Jackson. Terrestrial planet finder. http://planetquest.jpl.nasa.gov/TPF, 2006.

26. Julia W. Evans, Gary Sommargren, Bruce A. Macintosh, Scott Severson, and Daren Dillon. Effect of wavefront error on 10^{-7} contrast measurements. *Optics Letters*, 31 No.5:565–567, 2006.

27. Anand Sivaramakrishnan, James P. Lloyd, P. E. Hodge, and Bruce A. Macintosh. Speckle decorrelation and dynamic range in speckle noise-limited imaging. *Astrophysical Journal*, 581:L59–62, 2002.

28. Marshall D. Perrin, Anand Sivaramakrishnan, Russell B. Makidon, Ben R. Oppenheimer, and James R. Graham. The structure of high strehl ratio point-spread functions. *Astrophysical Journal*, 596:702–712, 2003.

29. L. A. Poyneer, B. Bauman, B. A. Macintosh, D. Dillon, and S. Severson. Spatially filtered wave-front sensor for high-order adaptive optics. *Opt. Lett.*, 31:293–295, 2006.

30. P. Jacquinot and B. Roizen-Dossier. *Progress in Optics*, volume 3, chapter Apodisation, p. 31–184. North-Holland Publishing Company-Amsterdam, 1964.

31. N. J. Kasdin, R. J. Vanderbei, D. N. Spergel, and M. G. Littman. Extrasolar planet finding via optimal apodized-pupil and shaped-pupil coronagraphs. *Astrophysical Journal*, 582(2):1147–61.

32. N. Jeremy Kasdin, R. J. Vanderbei, M. G. Littman, and D. N. Spergel. Optimal one-dimensional apodizations and shaped pupils for planet finding coronagraphy. *Applied Optics*, 44:1117–28.

33. D. Slepian and H. O. Pollak. Prolate spheroidal wave functions, fourier analysis and uncertainty—i. *The Bell System Technical Journal*, Jan.:43–62, 1961.

34. M. Bernard Lyot. A study of the solar corona and prominences without eclipses. *George Darwin Lecture, Assoc.R.A.S.*

35. Anand Sivaramakrishnan, Christopher D. Koresko, Russel B. Makidon, Thomas Berkefeld, and Marc J. Kuchner. Ground-based coronagraphy with high-order adaptive optics. *Astrophysical Journal*, 552:397–408, 2001.

36. Bruce Macintosh, James Graham, David Palmer, Rene Doyon, Don Gavel, James Larkin, Ben Oppenheimer, Leslie Saddlemyer, J. Kent Wallace, Brian Bauman, Julia Evans, Darren Erikson, Katie Morzinksi, Donald Phillion, Lisa Poyneer, Anand Sivaramakrishnan, Remi Soummer, Simon Thibault, and Jean-Pierre Veran. The Gemini Planet Imager. Brent L. Ellerbroek and Domenico Bonaccini Calia, editors, *Advances in Adaptive Optics II*, Proc. SPIE **6272**, p. 62720L, 2006.

37. M.J. Kuchner and W.A. Traub. A Coronagraph with a Band-limited Mask for Finding Terrestrial Planets. *The Astrophysical Journal*, 570(2):900–908, 2002.

38. A. Sivaramakrishnan, R. Soummer, A.V. Sivaramakrishnan, J.P. Lloyd, B.R. Oppenheimer, and R.B. Makidon. Low-Order Aberrations in Band-limited Lyot Coronagraphs. *The Astrophysical Journal*, 634(2):1416–1422, 2005.

39. John W. Hardy. *Adaptive Optics for Astronomical Telescopes*. Oxford Series in Optical and Imaging Science. Oxford University Press, New York, 1998.

40. Robert K. Tyson, editor. *Adaptive Optics Engineering Handbook*. Optical Engineering. Marcel Dekker, Inc., New York, 2000.

41. Claire Max. Adaptive optics and its applications. Lecture notes from course at UCSC, Fall 2003.

42. Roberto Ragazzoni. Pupil plane wavefront sensing with an oscillating prism. *Journal of Modern Optics*, 43 No. 2:289–293, 1996.

43. Kevin L. Baker, Eddy A. Stappaerts, Don Gavel, Scott C. Wilks, Jack Tucker, Dennis A. Silva, Jeff Olsen, Scot S. Olivier, Peter E. Young, Mike W. Kartz, Laurence M. Flath, Peter Krulevitch, Jackie Crawford, and Oscar Azucena. Breadboard testing of a phase-conjugate engine with an interferometric wave-front sensor and a microelectricalmechanical systems-based spatial light modulator. *Applied Optics*, 43 No.30:5585–5593, 2004.

44. Gleb Vdovin. *Adaptive Optics Engineering Handbook*, chapter Micromachined Membrane Deformable Mirrors, p. 231–248. Marcel Dekker, Inc., 2000.

45. Gordon D. Love. *Adaptive Optics Engineering Handbook*, chapter Liquid Crystal Adaptive Optics, p. 231–248. Marcel Dekker, Inc., 2000.

46. L.A. Poyneer and J.P. Véran. Optimal modal Fourier-transform wavefront control. *Journal of the Optical Society of America A*, 22(8):1515–1526, 2005.

47. F. Malbet, J.W. Yu, and M. Shao. High dynamic range imaging using a deformable mirror for space coronography. *Publications Of The Astronomical Society Of The Pacific*, 107:386–398, 1995.

48. Bruce Macintosh, James Graham, Ben Oppenheimer, Lisa Poyneer, Anand Sivaramakrishnan, and Jean-Pierre Veran. MEMS-based extreme adaptive optics for planet detection. Scot S. Olivier, Srinivas A. Tadigadapa, and Albert K. Henning, editors, *MEMS/MOEMS Components and thier Applications III*, Proc. SPIE **6113**, p. 48–57, 2006.

49. Donald Gavel. Laboratory for adaptive optics. http://lao.ucolick.org, 2006.

50. Thomas Bifano, Paul Bierden, and Julie Perreault. Micromachined deformable mirrors for dynamic wavefront control. John D. Gonglewski, Mark T. Gruineisen, and Michael K. Giles, editors, *Advanced Wavefront Control: Methods, Devices and Applications II*, Proc. SPIE **5553**, p. 1–16, 2004.

51. Gary E. Sommargren, D. W. Phillion, Michael A. Johnson, Nhan Q. Nguyen, Anton Barty, Franklyn J. Snell, Daren R. Dillon, and Lloyd S. Bradsher. 100-picometer interferometry for EUVL. Roxann L. Engelstad, editor, *Emerging Lithographic Technologies VI*, Proc. SPIE **4688**, p. 316–328, 2002.

52. Don Phillion and Gary Sommargren. Point source diffraction interferometry with lensless imaging. presented at CfAO workshop on ExAO Calibration, October 2003.

53. Gary E. Sommargren. Phase shifting diffraction interferometry for measuring extreme ultraviolet optics. OSA Trends in Optics and Photonics.

54. Gary Sommargren. Simulations of image resolution and edge ringing using a lensless phase shifting diffraction interferometer. Presented at ExAO weekly meeting, January 2004.

55. Gary Sommargren. Image resolution using a lensless phase shifting diffraction interferometer. Presented at ExAO weekly meeting, December 2003.

56. Scot Olivier. Advanced adaptive optics technology development. Robert K. Tyson, editor, *Adaptive Optics Systems and Technology II*, Proc. SPIE **4494**, p. 1–10, 2002.

57. William D. Cowan and Victor M. Bright. *Adaptive Optics Engineering Handbook*, chapter Surface Micromachined Deformable Mirrors, p. 249–272. Marcel Dekker, Inc., 2000.

58. Joel Kubby. Mems devices. presented at CfAO Summer School, Aug 2005.

59. Herbert R. Shea, Arman Gasparyan, Carolyn D. White, Robert B. Comizzoli, David Abushch-Magder, and Susanne Arney. Anodic oxidation and reliability of MEMS poly-silicon electrodes at high relative humidity and high voltages. Russel A. Lawton, editor, *MEMS Reliability for Critical Applications*, Proc. SPIE **4180**, p. 117–122, 2000.

60. Julia W. Evans, Bruce A. Macintosh, Lisa Poyneer, Katie Morzinski, Scott Severson, Daren Dillon, Donald Gavel, and Layra Reza. Demonstrating sub-nm closed loop MEMS flattening. *Optics Express*, 14:5558–5570, 2006.

61. Julia. W. Evans, Katie Morzinski, Scott Severson, Lisa Poyneer, Bruce Macintosh, Daren Dillon, Layra Reza, Don Gavel, David Palmer, Scot Olivier, and Paul Birden. Extreme adaptive optics testbed: Performance and charachterization of a 1024-MEMS deformable mirror. Scot Olivier, editor, *MEMS/MOEMS Components and their applications III*, Proc. SPIE **6113**, p. 131–136, 2006.

62. K. L. Baker, E. A. Stappaerts, D. Gavel, S. C. Wilks, J. Tucker, D. A. Silva, J. Olsen, S. S. Olivier, P. E. Young, M. W. Kartz, L. M. Flath, P. Krulevitch, J. Crawford, and Oscar Azucena. High-speed horizontal-path atmospheric turbulence correction with a large-actuator-number mircoelectricalmechanical system spatial light modulator in an interferometric phase-conjugation engine. *Optics Letters*, 29 No.15:1781–1783, 2004.

63. Julia. W. Evans, Katie Morzinski, Layra Reza, Scott Severson, Lisa Poyneer, Bruce Macintosh, Daren Dillon, Gary Sommargren, David Palmer, Don Gavel, and Scot Olivier. Extreme adaptive optics testbed: High contrast measurements with a MEMS deformable mirror. D. R. Coulter, editor, *Techniques and Instrumentation for Detection of Exoplanets II*, Proc. SPIE **5905**, p. 303–310, 2005.

64. N. Jeremy Kasdin, Ruslan Belikov, James Beall, Robert J. Vanderbei, Michael G. Littman, Michael Carr, and Amir Give'on. Shaped pupil coronagraphs for planet finding: Optimization, manufacturing, and experimental results. p. 128–136, 2005.

65. Abhijit Chakraborty, Laird A. Thompson, and Michael Rogosky. 10^{-7} contrast ratio at $4.5\lambda/d$: New results obtained in laboratory experiments using nano-fabricated coronagraph and multi-gaussian shaped pupil masks. *Optics Express*, 13 No. 7:2394–2402, 2005.

66. C. H. Lineweaver and D. Grether. What fraction of sun-like stars have planets? *Astrophysical Journal*, 598:1350–1360.

67. Nathan Doble, Geunyoung Yoon, Li Chen, Paul Bierden, Scot Oliver, and David R. Williams. Use of a microelectricalmechanical mirror for adaptive optics in the human eye. *Optics Letters*, 27 No. 17:1537–1539, 2002.

68. G Vdovin, P M Sarro, and S Middelhoek. Technology and applications of micromachined adaptive mirrors. *J. Micromech. Microeng.*, 9:R8–R20.

69. D. Dayton, J. Gonglewski, S. Restaino, J. Martin, J. Phillips, M. Hartman, S. Browne, P. Kervin, J. Snodgrass, N. Heimann, M. Shilko, R. Pohle, B. Carrion, C. Smith, and D. Thiel. Demonstration of new technology MEMS and liquid crystal adaptive optics on bright astronomical objects and satellites. *Optics Express*, 10 No.25:1508–1519, 2002.

70. John Trauger, Dwight Moody, Brian Gordon, Yekta Gürsel, Mark Ealey, and Roger Bagwell. Performance of a precision high-density deformable mirror for extremely high contrast imaging astronomy from sapce. J. Chris Blades and Oswald H. W. Siegmund, editors, *Future EUV/UV and Visible Space Astrophysics Missions and Instrumentation*, Proc. SPIE **4854**, p. 1–8, 2003.

71. Julia Wilhelmsen Evans, Gary Sommargren, Lisa Poyneer, Bruce Macintosh, S. Severson, Daren Dillon, Andrew Shenis, David Palmer, Jeremy Kasdin, and Scot Olivier. Extreme Adaptive Optics Testbed: Results and future work. Domenico Bonaccini Calia, Brent L. Ellerbroek, and Roberto Ragazzoni, editors, *Advancements in Adaptive Optics*, Proc. SPIE **5490**, p. 954–959, 2004.

72. Lisa A. Poyneer and Bruce Macintosh. Experimental demonstration of phase correction with a 32 x 32 microelectricalmechanical systems mirror and a spatially filtered wavefront sensor. *J. Opt. Soc. Am. A*, 21:810–819, 2004.

73. E. Vernet-Viard, M. E. Kasper, C. Verinaud, E. Fedrigo, N. N. Hubin, S. Esposito, E. Pinna, A. T. Puglisi, A. Tozzi, A. G. Basden, S. J. Goodsell, G. D. Love, and R. M. Myers. Extreme adaptive optics system optimization with the high-order test bench. Brent L. Ellerbroek and Domenico Bonaccini, editors, *Advances in Adaptive Optics II*, Proc. SPIE **6272**, p. 62722K, 2006.

74. Andrew Lowman, John Trauger, Brian Gordon, Joseph Green, Dwight Moody, Albert Niessner, and Fang Shui. High contrast imaging testebed for the terrestrial planet finder coronagraph. John C. Mather, editor, *Optical, Infrared and Millimeter Space Telescopes*, Proc. SPIE **5487**, p. 1246–1254, 2003.

75. John Trauger, Chris Burrows, Brian Gordon, Joseph Green, Andrew Lowman, Dwight Moody, Albert Niessner, Fang Shui, and Daniel Wilson. Coronograph contrast demonstrations with the high contrast imaging testbed. John C. Mather, editor, *Optical, Infrared and Millimeter Space Telescopes*, Proc. SPIE **5487**, p. 1330–1336, 2003.

76. Ruslan Belikov, Amir Give'on, John T. Trauger, Michael Carr, N. J. Kasdin, Robert J. Vanderbein, Fang Shi, Kunjithapatham Balasubramanian, and Andreas Kuhnert. Toward 10^{10} contrast for terrestrial exoplanet detection: demonstration of wavefront correction in a shaped-pupil coronagraph. John C. Mather, Howard A. MacEwen, and Mattheus W. M. de Graauw, editors, *Space Telescopes and Instrumentation I: Optical, Infrared, and Millimeter*, Proc. SPIE **6265**, p. 62621A, 2006.

77. Fang Shui, Andrew E. Lowman, Dwight C. Moody, Albert F. Niessner, and John T. Trauger. Wavefront amplitude variation of TPF's High Contrast Imaging Testbed: Modeling and experiment. Daniel R. Coulter, editor, *Techniques and Instrumentation for Detection of Exoplanets II*, Proc. SPIE **5905**, p. 483–493, 2005.

78. Sergio R. Restaino, Jonathan Andrews, Ty Martinez, Don Payne, Dave Wick, and Christopher Wilcox. MEMs-based adaptive optics systems: the naval research laboratory program. Scot S. Olivier, Srinivas A. Tadigadapa, and Albert K. Henning, editors, *MEMS/MOEMS Components and Their Applications III*, Proc. SPIE **61130**, p. 61130E, 2006.

79. Yuhua Zhang and Austin Roorda. MEMS deformable mirror for ophthalmic imaging. Scot S. Olivier, Srinivas A. Tadigadapa, and Albert K. Henning, editors, *MEMS/MOEMS Components and Their Applications III*, Proc. SPIE **6113**, p. 61130A, 2006.